

Nanoscale Strontium Titanate Sheets and Crystals

By

Jack Andrew Tilka

A dissertation submitted in partial fulfillment of

The requirements of the degree of

Doctor of Philosophy

(Materials Engineering)

at the

UNIVERSITY OF WISCONSIN-MADISON

2018

Date of final oral examination: 1/12/18

The dissertation is approved by the following member of the Final Oral Committee:

Paul G. Evans, Professor, Materials Science and Engineering
Susan E. Babcock, Professor, Materials Science and Engineering
Daniel C. Fredrickson, Associate Professor, Chemistry
Dane Morgan, Professor, Materials Science and Engineering
Xudong Wang, Professor, Materials Science and Engineering

Abstract

The physical properties of materials are dominated by their structure and composition. Insight into the structure of complex oxide materials has the potential to improve our understanding and eventually control of their physical properties. This PhD thesis reports the development of characterization and fabrication techniques relevant to improving the scientific understanding of complex oxide materials. The work presented here has two components. I report a way to use ideas that were originally developed in semiconductor processing to control the elastic strain state and crystallization process of the model complex oxide SrTiO₃. An additional component is an important series of advances in the analysis of diffraction patterns acquired with focused x-ray nanobeams.

The fabrication and characterization of nanoscale SrTiO₃ has been experimentally shown to allow the introduction of elastic strain into SrTiO₃. The creation of thin SrTiO₃ crystals from (001)-oriented SrTiO₃ bulk single crystals using focused ion beam milling techniques yields sheets with submicron thickness and arbitrary orientation within the (001) plane. Synchrotron x-ray nanodiffraction experiments show that the SrTiO₃ sheets have rocking curves with angular widths less than 0.02°. These widths are less than a factor of two larger than bulk SrTiO₃, which shows that the sheets are suitable substrates for epitaxial thin film growth. A precisely selected elastic strain can be introduced into the SrTiO₃ sheets using a silicon nitride stressor layer. Synchrotron x-ray nanodiffraction studies show that the strain introduced in the SrTiO₃ sheets is on the order of 10⁻⁴, matching the predictions of an elastic model. This approach to elastic strain sharing in

complex oxides allows the strain to be selected within a wide and continuous range of values, an effect not achievable in heteroepitaxy on rigid substrates.

An additional fabrication technique is also evaluated here based on the crystallization of SrTiO₃ from initially amorphous thin films. This process is known as solid-phase epitaxy in two-dimensional samples but is just beginning to be explored in more complex geometries. I report experiments in both homoepitaxy and heteroepitaxy including measurements of crystal growth rates and the crystallographic orientations of crystals formed in this way. The lateral growth rates are consistent with previously measured vertical growth. This result indicated that previous work on vertical solid-phase epitaxy could be extended into lateral solid-phase epitaxy, which has the power to be applied to complicated non-planar geometries.

The highly coherent and tightly focused x-ray beams produced by hard x-ray light sources enable the nanoscale structural characterization of materials but are accompanied by significant challenges in the interpretation of diffraction and scattering patterns. I report here a series of methods that expand the range of physical problems that can be accurately captured by coherent x-ray optical simulations. My approach has been to expand simulations methods to include arbitrary x-ray incident angles and arbitrary epitaxial heterostructures. I first applied these methods to extract the misorientation of lattice planes and the strain of individual layers of Si/SiGe heterostructures relevant to applications in quantum electronics. Further applications reported in this thesis are in probing defects created in the processing of SrTiO₃ and in measuring the change in lattice parameter introduced into strained SrTiO₃ sheets. The systematic interpretation of nanobeam diffraction patterns aids in the fabrication of SrTiO₃ nanostructures.

Acknowledgements

I would not have come this far without the help, support, and encouragement of my collaborators, group, mentors, friends, and family.

I would like to thank my advisor, Paul Evans, and my committee for advising and mentioning me through my induction to science.

I would like to thank my collaborators, especially at the Advanced Photon Source and Argonne National Laboratory, Deborah M. Paskiewicz, Dillon D. Fong, Zhonghou Cai and Martin Holt. Their commitment to excellence and innovation has been a tremendous help to my graduate school career.

The past and present members of the Evans's research group deserve much thanks. Kyle McElhinny, Josef Spalenka, Pice Chen, Margaret Cosgriff, Sarah Thompson, Qingteng Zhang, Gokul Gopalakrishnan, and Hamed Yusef, were a tremendous help in guiding me through at least my first few years in graduate school. Joonkyu Park, Yajin Chen, Youngjun Ahn, Arunee Lakkham, Sam Marks, and Anatasios Pateras were instrumental in my daily success in and around the laboratory, and sometimes crucial for time spent during beamtime.

My friends and colleagues in the Materials Science and Engineering Department and Chemistry Department have provided valuable discussion and insight into research.

I would like to thank my family for always being as supportive as they could both all the way from Florida, and from around the Midwest.

Finally, Thanks to Arielle Mensch.

Table of Contents

Abstract	i
Acknowledgements	iii
Table of Contents	iv
List of Figures and Equations	vi
1 Introduction and Motivation	1
1.1 Challenges in Controlling the Nanoscale Structure of Complex Oxide Materials	1
1.2 Nanoscale Structural Characterization	4
1.3 Nanoscale Complex Oxide Crystals: Fabrication and Phenomena	13
1.4 Solid-Phase Epitaxy	17
1.5 References	21
2 Nanoscale Characterization of Si/SiGe Heterostructures: X-ray Nanobeam Experiment and Diffraction Simulation	26
2.1 Introduction	26
2.2 Experimental Methods	31
2.3 Coherent Diffraction Simulation and Analysis Methods	32
2.4 Influence of Interfacial Structure on Diffraction	45
2.5 Conclusion	48
2.6 References	50
3 Fabrication and Characterization of Strontium Titanate Sheets	54
3.1 Introduction	54
3.2 Focused Ion Beam Milling of SrTiO₃	57
3.3 X-ray Characterization with Convergent Nanobeam	59
3.4 Discussion of Mosaic Distribution and Lattice Expansion	62
3.5 Conclusion	69
3.6 References	70
4 Stressor-Layer-Induced Elastic Strain Engineering in SrTiO₃ Complex Oxide Sheets	73
4.1 Introduction	73
4.2 Fabrication and Characterization of Strain SrTiO₃ Sheets	76
4.3 Analysis and Discussion of Nanodiffraction Patterns	83
4.4 Conclusion	87
4.5 References	89
5 Lateral Solid-Phase Epitaxy in Complex Oxide Sheets	92
5.1 Introduction	92
5.2 Lateral Solid-Phase Epitaxy of SrTiO₃ from SrRuO₃ Seed Crystals	97

5.3	Lateral Solid-Phase Epitaxy of SrTiO₃ from SrTiO₃ Seed Crystals	104
5.4	Conclusion	109
5.5	References	110
Appendix A		112
A.1	Create Focused X-ray Beam	112
A.2	Create Lattice Sum and Rocking Curve using Focused Beam	114

List of Figures and Equations

- Figure 1.1 Two-dimensional schematic of an Ewald sphere. The grey point represents the reciprocal lattice (HOL) plane where the θ and 2θ are set to the (002) reflection. ___ 6
- Figure 1.2 Two-dimensional schematic of the (HOL) plane of reciprocal space with an Ewald sphere produced by a focused x-ray beam. The convergence of the focused beam has a width of $\delta\theta$ and the greyed area of the Ewald's sphere represents the uncertainty associated with the convergence of the x-ray beam. _____ 8
- Figure 1.3 Schematic of a Fresnel zone plate taken from Thompson *et al.* (2001). _____ 10
- Figure 1.4 Schematic of the role of the x-ray focusing optics used to create the focused x-ray beam used throughout this thesis. (a) Perfectly collimated and monochromatic incoming parallel x-ray beam. (b) Fresnel zone plate and first order focus. (c) Order sorting aperture used to block higher order foci and some of the unfocused beam from propagating to the focal point. (d) Central stop used to block the remaining unfocused x-ray beam. _____ 11
- Figure 1.5 (a) Experimental, and (b) simulated x-ray diffraction pattern produced with zone plate based focusing optics. The height of the vertical region of intensity is the angular width of the convergent x-ray beam, $\delta\theta$. The width of the region of intensity is inversely proportional to the number of crystallographic planes illuminated by the x-ray beam. The dark region in the center is the projection of the shadow of the center stop on to diffraction pattern. _____ 12
- Figure 1.6. Number line of (bottom) commonly available substrates for complex oxides growth, and (top) complex oxide thin films. Adapted from Schlom *et al.* (2014). 13
- Figure 1.7 Schematic of a trilayer structure. The in-plane lattice parameters of the substrate and thin film are equal after thin film growth. _____ 14
- Figure 1.8 A strain sharing model that shows the final strain in a theoretical thin film with the elastic constants of STO as a function of thin film thickness. Starting lattice mismatches from -3% to 3% are shown. _____ 15
- Figure 1.9 Schematic of the interaction of the FIB with material taken from Volket *et al.* (2007). _____ 16
- Figure 1.10 Schematic of the growth of an epitaxial STO crystal from a seed crystal. _ 19
- Figure 2.1 (a) Schematic cross section of the Si/SiGe heterostructure grown on a graded SiGe layer on an (001)-oriented Si single crystal substrate. (b) Focused x-ray nanodiffraction geometry using Fresnel zone plate x-ray focusing optics and a two-dimensional CCD detector. Arrows indicate the direction of the sample rotation used to vary the x-ray incident angle. (c) Focused x-ray nanobeam diffraction pattern acquired at an angle close to the Bragg condition of the (004) reflection of the strained-Si QW. Intensity fringes visible as vertical stripes on the diffraction pattern

originate from the thickness of the 91 nm-thick top SiGe layer. (d) Radial slice of the three-dimensional simulated wave front propagating from the zone plate to the focus. Cylindrical coordinates Z and R correspond to the distance along the direction between the zone plate and the sample and the distance from the optical axis, respectively. _____ 29

Equation 2.1 _____ 34

Equation 2.2 _____ 35

Equation 2.3. _____ 35

Figure 2.2 The lattice sum method with multiple layers. Here the material represented in dark gray is N_1 layers thick with a lattice parameter of a_1 , and the material represented in light gray is N_2 layers thick with a lattice parameter of a_2 . _____ 35

Equation 2.4 _____ 36

Equation 2.5 _____ 36

Figure 2.3 (a) Schematic of the model sample used to create the simulated diffraction pattern. (b) Simulated θ - 2θ diffraction pattern created using the lattice sum of the model. The reflections centered at 26.95° and 27.45° arise from the SiGe and strained-Si QW layers, respectively. (c) Simulated diffraction patterns for x-ray incident angles of $\theta=26.95^\circ$ and $\theta=27.43^\circ$. Detector images in part (c) are each normalized to the maximum intensity in each image. (d) Simulated θ - 2θ scan produced by integrating the diffracted intensity in the wave-field simulation over the area of a single pixel of the two dimensional detector. _____ 37

Figure 2.4 Screen shot of the webpage made available to those interested in x-ray nanodiffraction at <http://xray.engr.wisc.edu/nanobeamsimulation/html/index.php>. 39

Figure 2.5 (a) Simulated θ - 2θ scan produced by a wave field simulation of the focused beam that has been integrated to include all of the intensity provided by the focusing optics. (b) Measured θ - 2θ scan produced by integrating the intensity over an area greater than the whole image of the zone plate on the detector. The angular resolution is set by the width of the zone plate, which broadens the narrow SiGe peak and eliminated the narrow thickness fringes. _____ 40

Figure 2.6 (a) Simulated θ - 2θ scan using the lattice sum method. Blue lines on the top axis correspond to the values of the incident angle where experimental and simulated diffraction patterns are shown below. (b) Simulated (top row) and experimental (bottom row) diffraction patterns acquired near the SiGe (004) reflection. (c) Simulated (top row) and experimental (bottom row) diffraction patterns acquired at the strained-Si QW (004) reflection. _____ 42

Figure 2.7 (a) Map of the integrated intensity of individual diffraction patterns at a fixed incident angle. (b) Focused x-ray nanobeam diffraction patterns measured at points indicated by the dotted and solid red boxes in (a). (c) Simulated diffraction patterns for two different effective incident angles with respect to the strained-Si QW. ____ 44

- Figure 2.8 Lattice sum of the Si/SiGe heterostructure as a function of reciprocal lattice vector and layer separation. The highest intensity region at 4.59 \AA^{-1} is the Bragg peak of the SiGe layer. _____ 45
- Figure 2.9 Two line profiles of the lattice sum calculated in Figure 2.8. The blue simulation is the result of the interference between the two layers when half a layer of empty space is added. _____ 46
- Figure 3.1 Schematic of the FIB procedure and x-ray geometry of the STO sheets. (a) Deposition of a protective C cap. (b) Coarse milling and trench creation at 14 nA. (c) Intermediate milling at 4 nA. (d) Fine milling at 300 pA. (e) X-ray scattering geometry. _____ 57
- Figure 3.2 SEM image of (a) large (110) face and (b) top edge of a 500-nm-thick STO sheet produced by FIB milling. The dimensions of the face are $9.5 \mu\text{m} \times 10.2 \mu\text{m}$. The darker region on the top is the protective C cap. _____ 58
- Figure 3.3 (a) SEM image of the milled sheet recessed into bulk STO. (b) Plot of transmitted x-ray intensity versus position. The bright region shows the trench milled into the substrate; the sheet cannot be resolved because the 500 nm thickness does not strongly absorb. _____ 60
- Figure 3.4 (a) Schematic of the synchrotron x-ray nanodiffraction experiment. (b) Experimental diffraction pattern of the (002) Bragg reflection of a (110) annealed STO sheet. (c) A simulated (002) diffraction pattern using the same focusing optics as in the experiment and an ideal 500 nm thick STO sample. (d) Five incoherently summed mosaic blocks of STO with orientations differing in θ over a range of 0.013° . The off center blocks each have one eighth the intensity of the block in the center of the image. _____ 61
- Figure 3.5 (a) Diffraction patterns of the (002) Bragg reflection from bulk unprocessed STO acquired with different sample orientations ranging from $\theta = 18.292^\circ$ to $\theta = 18.352^\circ$. The region of high x-ray intensity moves from left to right as θ increases. The shadow of the center stop is apparent at $\theta = 18.322^\circ$. (b) Integrated intensity as a function of angle for the diffraction patterns shown in (a). The intensity of the rocking curve is approximately constant over an angular range equal to the zone plate divergence because part of the divergent beam meets the Bragg condition for all angles in this range. (c) Narrow rocking curves produced by integrating within the region of interest indicated by the white box in (a). _____ 63
- Figure 3.6 (a) Histograms of rocking curve widths of bulk STO before and after annealing. (b) Histograms of rocking curve widths of STO sheets. The most frequent width in both cases is 0.016° . _____ 64
- Figure 3.7 (a) STO plans that have been elastically or plastically bent to cause a curvature in the STO sheet. (b) STO planes with low angle grain boundaries (c) schematic of the height of STO sheet illuminated by the nanofocused x-ray beam. _____ 66
- Figure 3.8 Histograms of the lattice expansion in the STO sheets acquired in the same locations as Figure 3.6(b). _____ 68

- Figure 4.1(a) Schematic of the STO sheet with SiN stressor layers. Scanning electron microscopy images of a 510-nm-thick STO sheet (b) without (c-d) with a 270-nm-thick SiN layer deposited on the face. The large face of the sheet has area $10 \times 10 \mu\text{m}^2$. _____ 77
- Figure 4.2 Schematic of the x-ray scattering geometry showing the definitions of the angles θ and 2θ . _____ 79
- Figure 4.3 (a) Three experimental diffraction patterns taken different incident angles each with three different rectangular regions of interest with colors corresponding to the vectors and peaks in (b) and (c) respectively. (b) Schematic x-ray scattering showing different incident wavevectors within a single incident angle. (c) Three rocking curve peaks corresponding to the rectangles in (a). _____ 80
- Figure 4.4 (a) Diffraction patterns of the (200) STO bulk Bragg reflection. (b) Simulated dynamical diffraction patterns of the (200) bulk Bragg reflection. (c) Diffraction patterns of the (200) STO sheet. (d) Simulated kinematic diffraction patterns of the (200) STO sheet. _____ 82
- Figure 4.5 (a) Simulated diffraction pattern at the nominal Bragg condition. (b) Tilt and (c) strain resulting in the sample angular shift in the diffraction pattern. (d) The integrated intensity of the tilt and strain shown as a function of pixel in the horizontal direction highlighting the difficulty in distinguishing the effects of tilt and strain. _____ 84
- Figure 4.6 Simulated STO rocking curves for (a) unstrained STO with zero tilt, (b) unstrained STO with a 0.1° tilt, and (c) -0.2% strained STO with zero tilt. The dotted lines and crosses are a guide to the eye. (d) Schematic of tilt and strain in the STO sheets with lattice spacing d . _____ 85
- Figure 4.7 Histogram of strain measured from the (200) rocking curves in the STO sheets without a SiN layer (blue cross hatched) and with a SiN layer (red cross hatched). The change in lattice parameter of the bare STO sheet arises from the FIB processing. The increase in lattice parameter after SiN deposition agrees with the mechanical prediction for an elastically strained sheet. (b) Predicted strain in STO sheets as a function of thickness of the STO sheet for different stress-thickness product. The black line is the experimental stress, and the black asterisk represents the experimentally measured stress and strain. _____ 88
- Figure 5.1 (a) Schematic of SPE of STO on STO: (i) amorphous STO as deposited on an (001) crystalline STO substrate, (ii and iii) crystallization of STO as the crystalline/amorphous interface moves toward the surface, (iv) fully crystallized STO. (b) Schematic of SPE of STO on $\text{SiO}_2/(001)$ Si: (i) amorphous STO as deposited on the $\text{SiO}_2/(001)$ Si substrate, (ii) period of annealing during which no nucleation and growth of the crystalline STO forms, (iii) nucleation and growth of crystalline STO into amorphous STO, (iv) fully crystallized polycrystalline STO on $\text{SiO}_2/(001)$ Si. Taken from Chen *et al.* (2017). _____ 94
- Figure 5.2 Minimum distance, L_C , that can be crystallized before nucleation is expected to take place away from seed crystal. Adapted from Chen *et al.* (2017). _____ 95

- Figure 5.3 (a) Optical image of the SRO seed after it has been transferred to a Si substrate. (b) SEM image of the same SRO sheet. The wrinkles present in the SRO are a defect from the imperfect transfer process. _____ 97
- Figure 5.4 Schematic of the lateral SPE of STO on single crystal SRO seeds (a) 50 nm thick SRO seeds, shown in green, with 50 nm square holes spaced throughout the structure that has been transferred to a Si (001) substrate. (b) 50 nm thick layer of amorphous STO is sputtered over the whole surface. (c) The heterostructure is annealed at 450 °C for various times. The dark red represents the (002) heteroepitaxially STO on SRO, the dark orange represents the directionally grown lateral SPE STO, and the light orange is the amorphous STO thin film. _____ 99
- Figure 5.5 (c) X-ray nanodiffraction intensity of the (002) STO peak plotted on the same scale as the Ru fluorescence intensity. The intensity drops in (c) show that the (002) STO ends at the boundary of the SRO seed crystals. (a) Secondary electron SEM image of STO crystallized on SRO. (b) EBDS of the same area shown in (a) with the inverse pole figure color scale corresponding to the directions shown below the image. _____ 101
- Figure 5.6 Schematic of STO seeds and STO on STO SPE. (a) Amorphous STO deposited through a shadow mask. (b) Mask is removed and leaves behind insulated amorphous STO near the boundary of the shadow mask. (c) The sample is annealed for 3 h at 650 °C. (d) A second amorphous STO layer is deposited over the whole surface. (e). Material is annealed for various times at 450 °C. The dark orange represents the directed crystal growth from the STO crystalline STO seeds. _____ 105
- Figure 5.7 Secondary electron SEM images of the STO crystallized from the STO seed. (a) First 60 nm thick amorphous layer. (b) After first anneal at 650 °C for 3 h. (c) Second 60 nm thick amorphous layer. (d) Final structure after annealing at 450 °C for 6 h _____ 106
- Figure 5.8 (a) Secondary electron SEM image of an STO film that was annealed for 270 min. The gray disks represent crystalline STO that has grown into the dark amorphous region, and the bright objects located in the center of the gray disks are the nucleation sites for the STO growth. (b) Similar SEM image taken of an STO film that was annealed for 870 min. (c) Scatter plot of the average crystalline radius measured from representative disks within STO films with different annealing times. The data are fit with a line to determine a growth rate of 0.44 nm/min. _____ 107

1 Introduction and Motivation

1.1 Challenges in Controlling the Nanoscale Structure of Complex Oxide Materials

Nanoscale complex oxides have the potential to be exploited in applications that take advantage of their numerous interesting properties including ionic transport, ferroelectricity, ferromagnetism, large semiconducting band-gap, two dimensional electron gases, and quantum wells [1–5]. Complex oxides are a class of oxides that have more than one metal cation and crystal structures that can include many structural degrees of freedom. The structure and composition of many classes of complex oxides, including those based on the perovskite family, can be tuned to adjust the properties of the compounds precisely. Complex oxide thin films have applications as dielectrics, sensors, and capacitors [6–8]. The wide range of compositions leads to a broad and fascinating parameter space in which the chemistry and crystallography can be tuned to engineer a huge range of properties.

Despite the versatility and precision of the existing range of techniques that are available to complex oxides, there remain several opportunities to improve the ability to control their properties. This is particularly true through the use of nanoscale concepts in synthesis and characterization. The range of nanoscale techniques that can be applied to control the properties of complex oxides can be expanded by drawing from the large body of work on group-IV semiconductors such as Si and SiGe. These semiconducting materials already have a wide range of uses including field effect transistors, in which nanoscale control of the lattice constant of these systems has lead to increases in device

performance [9–13]. Applying concepts for the nanoscale introduction of strain to complex oxides could significantly impact the field. Expanding the range of synthesis methods at the nanoscale by drawing from semiconductor synthesis has a similarly large potential impact. This thesis also explores the role of nanoscale structure in controlling solid-phase epitaxy (SPE), the epitaxial crystallization of an initially amorphous volume of material. SPE has been widely applied in group IV semiconductors. It underpins the recrystallization of crystalline semiconductors after creating highly doped layers [14]. Bringing SPE to nanoscale complex oxides presents formidable challenges in synthesis and characterization, but it has the potential to allow new compositions and geometries for these materials.

This thesis addresses two main points in the synthesis and characterization of complex oxides. First, I have demonstrated a new method that allows nanoscale complex oxides to have unique structural properties by elastically deforming them to a specific lattice parameter. Second, I have shown that an important class of materials with the perovskite crystal structure can be grown in nanoscale geometries using SPE. A common issue linking these problems is that precise structural characterization is a difficult challenge. I have addressed this problem by developing x-ray diffraction analysis techniques that allow better understanding of the complex diffraction patterns associated with the use of nano focused x-ray beams.

the key impacts and results of this thesis will be covered in chapter 2-5 that each focus on a particular accomplishment, or set of related accomplishments in fabrication, characterization, or both. A brief overview of those impacts and chapters are provided below. The expansion of the simulation and analysis of x-ray nanobeam diffraction is

discussed in chapter 2. The creation of thin complex oxide sheets, as well as the creation of characterization procedures for evaluating rocking curve widths using nanobeams is discussed in chapter 3. Introducing elastic strain into complex oxide sheets and the development of characterization techniques to measure that strain using a nanobeam is discussed in chapter 4. Microns long growth and the growth rates for lateral SPE is discussed in chapter 5.

Chapter 2 is an overview of the analysis strategies employed in the characterization of these complex diffraction patterns to further the understanding of structural properties at the nanoscale of crystalline materials. The key accomplishment of the work reported in Chapter 2 is the creation of simulations that quantitatively reproduce x-ray nanodiffraction patterns. The simulations accommodate an arbitrary selection of the x-ray zone plate focusing optics and x-ray energy and allow the angle of incidence and thin film heterostructure to be precisely defined. Chapter 2 reports the comparison of these results with experiments on thin film heterostructures composed of Si and SiGe alloys. The simulations are further used through the remaining chapters to aid in the interpretation of x-ray diffraction studies in other materials, illustrating the general importance of the simulation. In addition to reporting the simulations in journal publications, I have disseminated the methods by creating an online simulator that can be used by anyone interested in precise interpretation of the diffraction from x-ray nanobeams [15–17].

Chapter 3 focuses on the development of nano fabrication techniques aimed at exploring strain sharing in complex oxide systems. The focused ion beam (FIB) was used to create thin sheets of SrTiO₃ (STO) that could potentially be used as a compliant

substrate for further complex oxide growth. X-ray nanodiffraction was used to verify that the damage introduced due to the FIB fabrication was sufficiently small that the sheet still fell within the range of quality typically used for heteroepitaxial growth, as evidenced through x-ray rocking curve analysis.

Chapter 4 demonstrates a proof of concept that thin STO sheets fabricated by FIB can be used for elastic strain sharing by showing that they are elastically compliant through the deposition of silicon nitride thin films. The key insight provided in chapter 4 is that the elastic strain produced by the silicon nitride thin film is in excellent agreement with the prediction of mechanical models, so the approach could be broadened to precise engineering design of complex oxide systems.

Chapter 5 addresses the lateral SPE of STO from SRO and STO seeds. The pivotal finding is that the SRO seed templates the crystalline STO to have directed crystal growth through an amorphous STO thin film. This potentially provides a powerful processing technique for non-planer geometries of complex oxides systems.

The remainder of this introductory chapter outlines the primary material and reoccurring ideas presented throughout the thesis. I start with the key topics of x-ray diffraction, including reciprocal space. Conventional x-ray diffraction experiments are first examined in order to draw a clear comparison with the more complicated optical arrangement of nanobeam diffraction studies.

1.2 Nanoscale Structural Characterization

Crystalline solids are composed of a periodic array of atoms. Geometrically, it is easiest to describe the crystal structure by decomposing the periodic structure into a Bravais lattice and a list or “basis” of atoms near each lattice site. The basis describes the

atomic number and location of the constituent atoms of the structure within a convenient repeating unit. When this repeating unit is the smallest repeatable structural unit, it is termed the primitive unit cell. In other cases a larger conventional unit cell may be used in order to simplify the description of the properties of the materials. The Bravais lattice is comprised of the points in space through which the basis must be translated to reproduce the bulk solid and can be represented by the vectors connecting the position of a single lattice point to its nearest neighbors. In the case of cubic systems, which are the focus of this work, the vectors are orthogonal and the distances are termed the lattice parameters. Lattice parameters in crystalline materials are typically on the order of 3-5 Å [18,19].

X-rays provide a powerful tool to probe the structure of crystals because the wavelength, λ , of x-rays is on the order of 1 Å, which means that they can diffract from periodic groups of atoms. The angles and intensities with which x-rays are diffracted can be used to determine lattice parameters, orientation, and in principal recreate the whole structure. A central idea used to understand the diffraction of x-rays is called reciprocal space. Reciprocal space is the Fourier transform of the location of the atoms in the real space of the crystal. Like real space, reciprocal space is made up of a series of periodically repeating points called a reciprocal lattice. Each point in the reciprocal lattice corresponds to the orientation and periodicity of a set of interatomic planes that make up the crystal. The vector between the origin of reciprocal space and a reciprocal space lattice point is called G . The incoming x-ray beam can also be represented as a vector in reciprocal space, k_i , depicted in Figure 1.1 such that $k = 2\pi/\lambda$. The vector k_i always ends at the origin of reciprocal space, and shares the same tail as the scattered x-ray beam.

A useful visualization of these concepts is called the Ewald sphere. This is shown in Figure 1.1. The energy of the incoming and outgoing x-ray beams is equal when the elastic interactions are considered. Therefore, the magnitude of the incoming and outgoing x-ray reciprocal space wavevectors must be equal. All of the possible locations for the head of the outgoing wavevector must lie on the Ewald sphere, which has a radius equal to the magnitude of the x-ray wavevector and one point on the origin. The vector that described the scattering of the x-rays in the crystals is $Q = k_d - k_i$, where k_d is the diffracted beam. Reciprocal lattice points only exist in periodic locations in reciprocal space, and strong diffraction of x-rays will take place when $Q = G$. Once the magnitude and angle of k_i set, any location on the Ewald sphere that intersects a reciprocal lattice

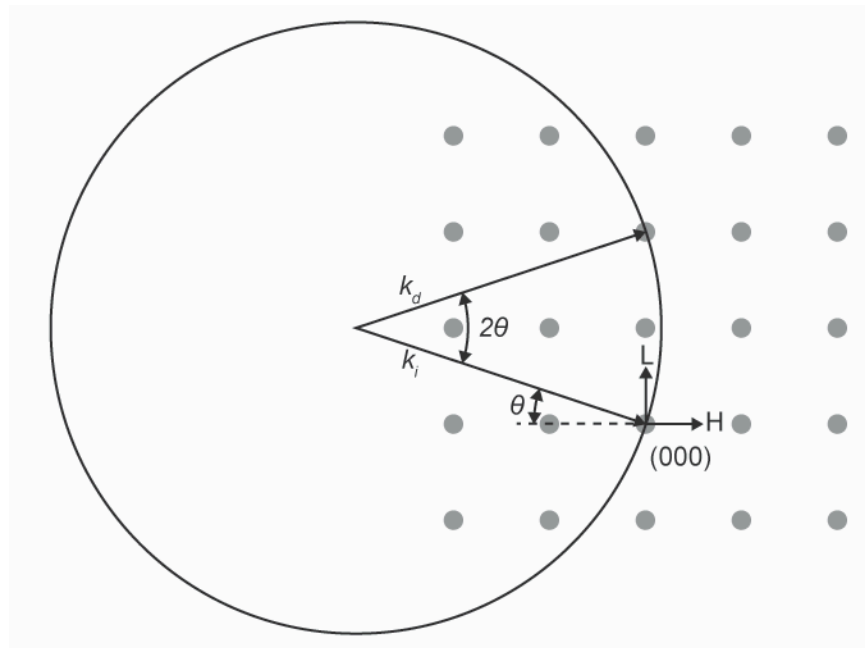


Figure 1.1 Two-dimensional schematic of an Ewald sphere. The grey point represents the reciprocal lattice (HOL) plane where the θ and 2θ are set to the (002) reflection.

point will result in a diffracted x-ray beam with high intensity. These diffracted points can be measured, and the real space structure of the crystal determined.

In the past, x-ray characterization of solids has had a transformative impact on the understanding of crystalline materials. The parallel-beam approach is based on an analysis in which the incident x-ray beam can be approximated as a plane wave. The interpretation of heterostructure and superlattice diffraction intensity distributions is well-known, and there is straightforward and effective mapping between the angular distribution of diffracted intensity and the structure of the sample [20,21].

The interpretation described in Figure 1.1 is complicated by the introduction of x-ray focusing optics. Conventional x-ray sources used in laboratory scale x-ray diffraction, such as a rotating Cu anode, are often used to probe the volume averages of materials over a scale of hundreds of microns to tens of centimeters. The structural properties of materials may vary over a size ranges that are much smaller than lab sources can probe. For example, grains of different orientation or phase could be on the order of nanometers, or strain induced from the deposition of electrodes could vary over microns [22]. When these smaller structural scales are of interests, then x-ray focusing optics can be used to create smaller x-ray spot sizes through which a sample can be rastered in order to create fine multidimensional scans of the material. Focusing x-rays is more challenging than focusing visible light. This is because the index of refraction of x-rays is much closer to unity than optical light, with indices of refraction near 10^{-6} leading to weak interactions with mater.

Tightly focused x-ray beams found at hard x-ray synchrotron sources promise to allow the characterization of the distribution of strain, composition, and lattice orientation at length scales of tens of nanometers. Such scales are relevant to fundamental physical processes in the formation and interaction of structural defects during epitaxy, the

patterning of surface features via self-assembly, and the creation of semiconductor devices [23–26]. The small spot sizes produced by diffraction based focusing optics also produce large angular divergence of the focused beam. For example, a spot size of 10 nm has a divergence of 12 mrad at a wavelength of 1 Å [18]. The divergence from the focusing optics is the origin of the uncertainty associated with Figure 1.2 and equal to magnitude of $\delta\theta$.

The diffraction experiments with STO sheets were carried out at station 2ID-D of the Advanced Photon Source (APS) at Argonne National Laboratory. The Si/SiGe

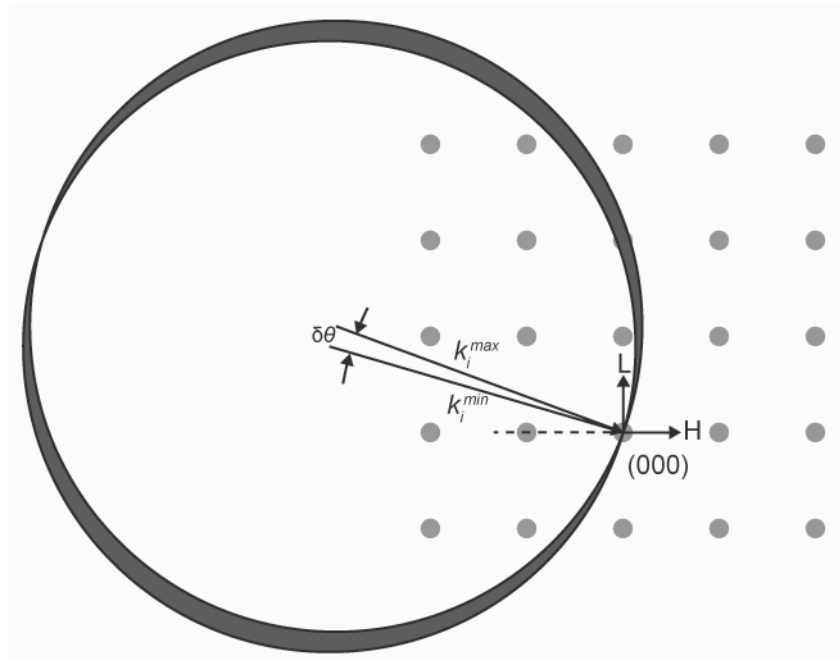


Figure 1.2 Two-dimensional schematic of the (H0L) plane of reciprocal space with an Ewald sphere produced by a focused x-ray beam. The convergence of the focused beam has a width of $\delta\theta$ and the greyed area of the Ewald's sphere represents the uncertainty associated with the convergence of the x-ray beam.

heterostructures were studied at the Sector 26 ID-C at the APS. The electrons at the APS are accelerated to near the speed of light in bunches. The APS has different bunch modes for different applications, but for experiments carried out at speeds slow compared to the

speed at which an electron bunch can travel around the ring, the individual bunches do not play a major role in the x-ray intensity and the beam can be treated as continuous.

Station 2ID-D uses a magnetic insertion device to generate photons from the storage ring. The insertion device has magnets with alternating north and south poles above and below the electron beam. When the relativistic electrons pass through the alternating magnetic fields they take a path of alternating radii of curvature. The accelerating electrons radiate photons. These photons sum coherently along the direction of the electron beam and are polarized perpendicular to the insertion device [27]. The distance between the magnets in the insertion device can be altered to tune the x-ray energy. The emitted x-rays are not only at the primary energy but also energies from higher harmonics. To prevent the higher harmonic radiation from interfering with the data, an x-ray mirror is placed at the angle of the total external reflection for the first harmonic but not the higher harmonics. The mirror is water cooled from the back to dissipate the energy that is heating the mirror. The beam energy is selected by a double-bounce Si (111) monochromator with an energy bandwidth of 1.3×10^{-4} . The beam is focused with a zone plate that is 160 μm in diameter with an outermost zone width of 100 nm. The focal spot had a full width of half-maximum (FWHM) of roughly 100 nm. These parameters are important in modeling the diffraction of the focused beams.

The optical configuration of sector 26 of the APS is similar, but with important differences in the zone plate optics and the size of the final focal spot. The zone plate at sector 26 used in these experiments is 160 μm in diameter with a nominal outermost zone width of 30 nm. The measured focal spot size is 50 nm FWHM at the sample. The nanofocused beam is rastered across the sample by finely controlling the position of the

zone plate within the larger unfocused parallel beam. The mechanical precision needed to achieve the fine control the necessary piezoelectric stages is achieved with the feedback of optical sensors. The combination of the powerful structural probe and fine spatial resolution of the beamline creates a system that can be imaged as an x-ray microscope rather than a more conventional diffractometer.

The technology that currently creates the smallest spot size is a Fresnel zone plate. The zone plate is made with rings of alternated indices of refraction and decreasing size as shown in Figure 1.3 [28]. The materials used to create the zone plate are Au and

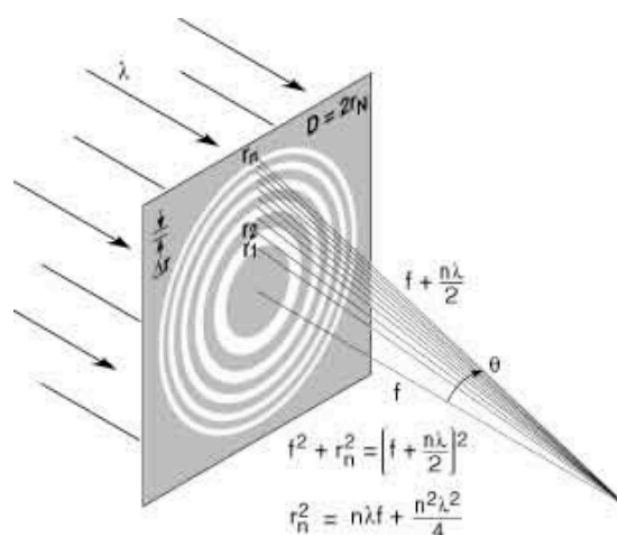


Figure 1.3 Schematic of a Fresnel zone plate taken from Thompson *et al.* (2001).

vacuum with radii, $r_1, r_2 \dots r_n$, where r_n is the radius of the n^{th} zone, and Δr is the width of the outer most zone. The other notable zone plate parameters are diameter of the zone plate, D_{ZP} , and number of zones, N . The zone plate parameters and the x-ray energy used for a given experiment determine the focal length, f , and spot size. The fraction of the intensity that the zone plate focuses is called the focusing efficiency, which is less than 10% of the starting x-ray intensity. Additionally, a zone plate requires large coherence

lengths, which are only on the order of nm in laboratory sources. Due to these factors, nanofocused x-ray beams require the high brilliance, long coherence length, and high degree of collimation allowed by synchrotron x-ray sources.

Other focusing optics related to selecting the first order focus are required in order to create a focused x-ray beam using a zone plate. A schematic of the optics required and the effect they have on the final profile of the focused beam is shown in Figure 1.4

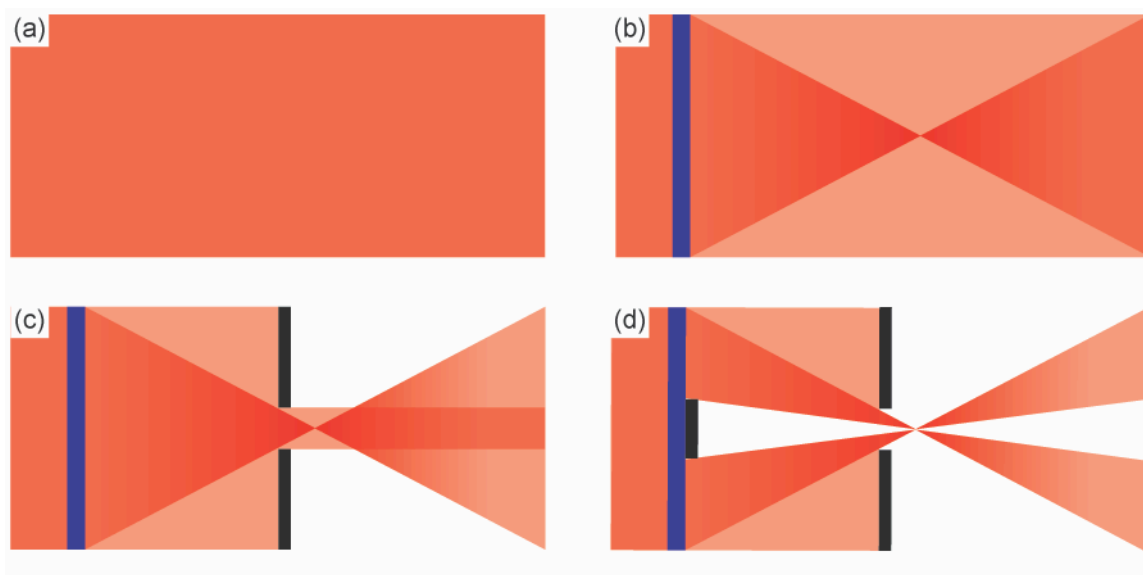


Figure 1.4 Schematic of the role of the x-ray focusing optics used to create the focused x-ray beam used throughout this thesis. (a) Perfectly collimated and monochromatic incoming parallel x-ray beam. (b) Fresnel zone plate and first order focus. (c) Order sorting aperture used to block higher order foci and some of the unfocused beam from propagating to the focal point. (d) Central stop used to block the remaining unfocused x-ray beam.

starting from the unfocused beam. Here I assume that the beam is perfectly collimated, parallel, and monochromatic, Figure 1.4(a). The parallel beam encounters the zone plate, which imprints a phase on the parallel beam that is propagated to the various foci of the zone plate. The majority of the beam is transmitted through the zone plate unaffected, and the transmitted beam and first order focus is shown in Figure 1.4(b). The intensity from the higher order foci, and transmitted beam far from the center of the zone plate are blocked from the sample with the order-sorting aperture as shown in Figure 1.4(c). The

transmitted beam, or zeroth order focus, is blocked from passing through the center of the order sorting aperture by the center stop as shown in Figure 1.4(d). Ideally the focusing optics will allow only the first order focus from the zone plate to transmit to the sample. These optics result in a tightly focused nanobeam with a distinctive diffraction pattern.

The zone plate and center stop lead to an annulus of intensity in reciprocal space. In the case the an out-of-plane Bragg reflection that will be evaluated throughout this

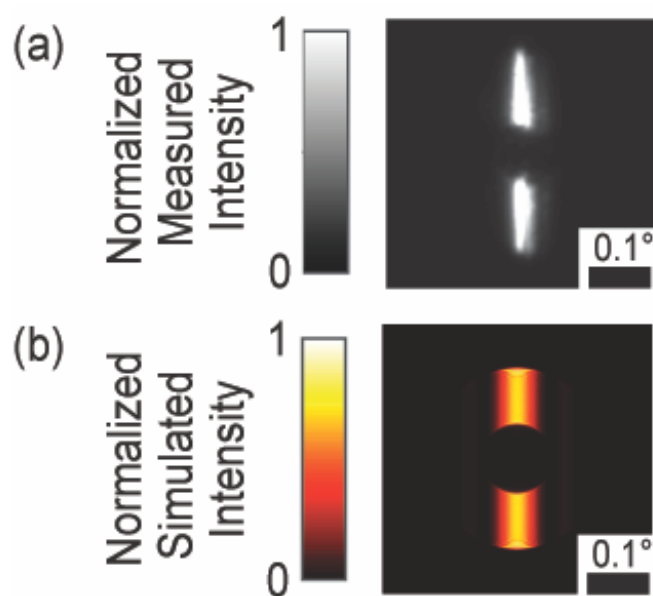


Figure 1.5 (a) Experimental, and (b) simulated x-ray diffraction pattern produced with zone plate based focusing optics. The height of the vertical region of intensity is the angular width of the convergent x-ray beam, $\delta\theta$. The width of the region of intensity is inversely proportional to the number of crystallographic plans illuminated by the x-ray beam. The dark region in the center is the projection of the shadow of the center stop on to diffraction pattern.

thesis, the final diffraction pattern is a single stripe of intensity with a length equal to the angular divergence of the x-ray beam, a shadow with a radius equal to the angular width of the center stop, and a width related to material from which the x-ray beam is scattering as shown in Figure 1.5.

1.3 Nanoscale Complex Oxide Crystals: Fabrication and Phenomena

Strain can alter the physical properties of complex oxides, including the Curie temperature, polarization, and permittivity of ferroelectric oxides [1,2]. The effects of strain on the functional electronic properties of oxide thin films have been explored extensively. Some examples of the relevance of these effects in condensed matter physics

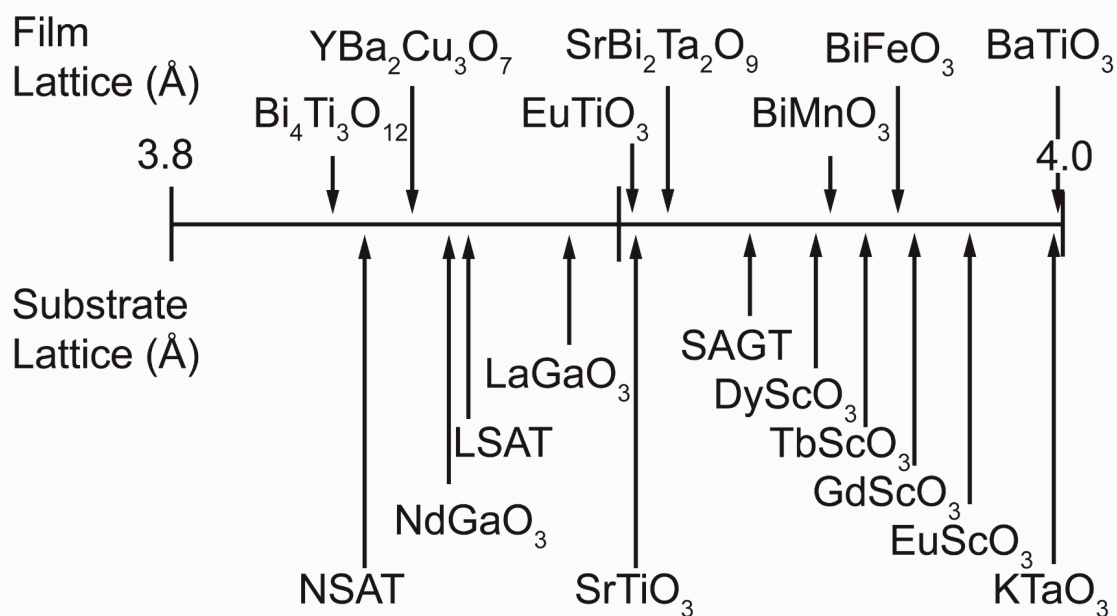


Figure 1.6. Number line of (bottom) commonly available substrates for complex oxides growth, and (top) complex oxide thin films. Adapted from Schlom *et al.* (2014).

include the observation of a large strain-mediated magnetoelectric coupling coefficient for $\text{La}_{0.7}\text{Sr}_{0.3}\text{MnO}_3$ thin films grown on $\text{Pb}(\text{Mg}_{1/3}\text{Nb}_{2/3})_{0.72}\text{Ti}_{0.28}\text{O}_3$ [29]. Similarly, the metal-to-insulator transition temperature in superconducting $\text{La}_{1.85}\text{Sr}_{0.15}\text{CuO}_4$ [30], and phase boundaries in BiFeO_3 are modified by strain [31,32]. Growing thin films epitaxially on different substrates also creates opportunities to access properties not normally present in oxide systems. For example, SrTiO_3 (STO) can become ferroelectric at room temperature under biaxial tensile strain [33,34].

A key approach to creating strain in complex oxide thin films has been to synthesize thin films by epitaxial growth on substrates with a different lattice parameter. In a general sense, the growth process is termed heteroepitaxy because the substrate and thin film have different compositions. The in-plane lattice mismatch between the thin film and substrate then controls the magnitude of strain in complex oxide thin films by constraining the in-plane lattice constant of the thin film to that of the substrate. This heteroepitaxial growth approach faces important limitations because the values of the strain are set by available substrate lattice parameters for which single crystals with

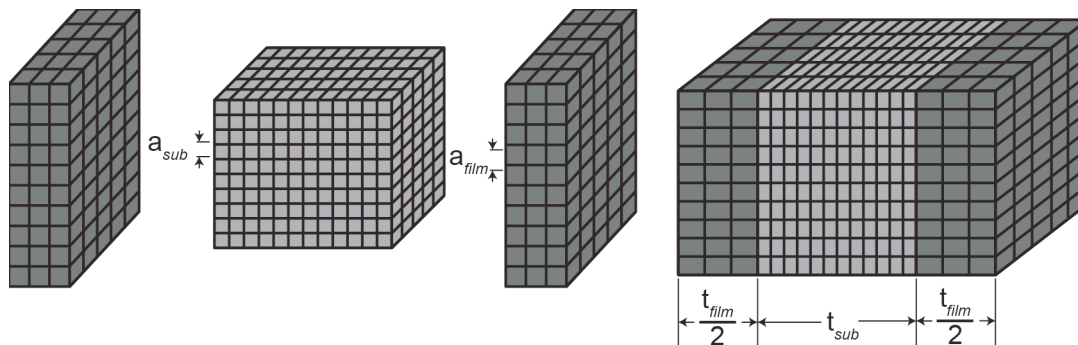


Figure 1.7 Schematic of a trilayer structure. The in-plane lattice parameters of the substrate and thin film are equal after thin film growth.

sufficiently low defect density can be created [37]. A chart of the commonly used substrates including $(\text{NdAlO}_3)_{0.39}\text{-(SrAl}_{1/2}\text{Ta}_{1/2}\text{O}_3)_{0.61}$ (NSAT), $(\text{LaAlO}_3)_{0.29}\text{-(SrAl}_{1/2}\text{Ta}_{1/2}\text{O}_3)_{0.71}$ (LSAT), $\text{Sr}_{1.04}\text{Al}_{0.32}\text{Ga}_{0.35}\text{Ta}_{0.5}\text{O}_3$ (SAGT), and thin films is shown in Figure 1.6. Because the choice of substrate lattice parameters is fixed by available substrate composition, the strains in epitaxial thin films are limited to discrete values. Changing the strain of a thin film often requires growing on different substrates. Some films have no substrate with a lattice mismatch small enough to prevent the nucleation of misfit dislocations.

In semiconductors such as Si/SiGe or GaAs, the ranges of achievable strain can be dramatically expanded by growing thin films on thin elastically compliant substrates [35,36]. When the elastic strain is shared by the substrate and thin film, the strain is a more easily varied parameter. Mechanically compliant substrates must be thin enough to relax during growth, and have crystallographic quality similar to bulk substrate materials.

I have explored a lithographic technique to produce oxide substrate sheets by FIB milling thin enough to allow strain relaxation in films of only 100 nm thick. The sheets are attached to the bulk at one end and have two large surfaces exposed for growth. Growth on both surfaces simultaneously would result in a trilayer structure as shown in Figure 1.7. The strain sharing between the thin film and substrate can be modeled by assuming that all of the distortion is elastic [36]. Figure 1.8 shows the strain that the thinnest substrate I have created to date, with a thickness of 225 nm, would impart on a thin film with the lattice parameters elastic constants of STO and various initial lattice mismatches as a function of thin film thickness. The model is created by considering a

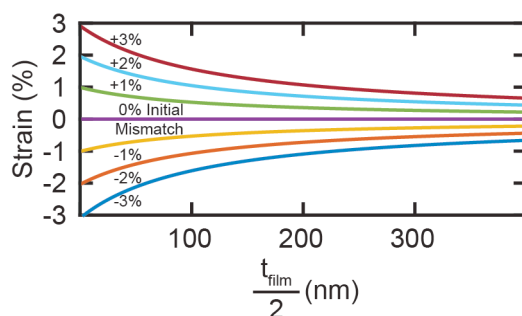


Figure 1.8 A strain sharing model that shows the final strain in a theoretical thin film with the elastic constants of STO as a function of thin film thickness. Starting lattice mismatches from -3% to 3% are shown.

trilayer structure with thin films of equal thickness on each side of an STO sheet. The final force per unit length applied on the thin films and substrates at the thin

film/substrate interface and the in-plane lattice parameters must be equal at equilibrium. The strain in the thin film is therefore dependent on differences in the in-plane lattice parameter, thickness, and biaxial modulus. In the limit of zero film thickness no strain sharing occurs and the thin film is strained by exactly the equilibrium lattice mismatch. As the thin film thickness increases the strain monotonically moves toward zero strain as the substrate and thin film both elastically relax to accommodate their lattice mismatch. The elastic constants of various complex oxides are similar to that of STO. As a result,

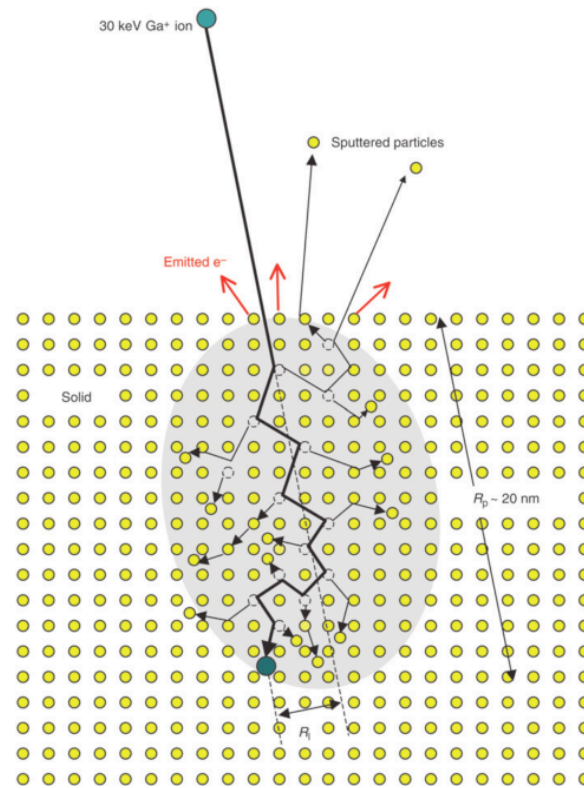


Figure 1.9 Schematic of the interaction of the FIB with material taken from Volkert et al. (2007).

other materials systems will follow the same trend with a similar order of magnitude as in shown in Figure 1.8. A BaTiO₃ (BTO) thin film, for example, has a lattice mismatch of -2% with STO, and with this model is expected to have a strain of 1.4% at a BTO layer thickness of 200 nm thick.

Ion-induced damage is a major concern in the use of ion-beam milling to create oxide nanostructures like the ones created in chapter 3 and 4. The interaction from the FIB is considered through the collision cascade model, shown in Figure 1.9, where the bombarding ions participate in a series of independent binary collisions [38]. An atom is moved off its lattice site when the energy transferred to it is greater than the displacement energy. The displaced atom can have enough energy to displace additional atoms in subsequent collisions. The range over which the Ga^+ ions come to rest in the material is referred to as the straggle and transverse straggle in the directions parallel and perpendicular to the incoming ion beam, respectively. When the distribution of Ga^+ ions follows a Gaussian distribution the straggle can be represented using a single value representing the root-mean-square width of the ion distribution [39]. Atoms displaced from lattice sites located near a surface have a chance to be completely removed from the bulk material into the vacuum in a process called sputter removal, which is the mechanism through which a FIB mills material. Damage from FIB arises from several fundamental effects. Ion scattering displaces atoms from lattice sites, creating vacancies and interstitials, which can coalesce to form loops and an increase in dislocation density [40,41]. An increase in vacancy concentration can expand the lattice parameter in STO [42]. The transverse straggle from the ion milling creates an amorphous region along the sidewall of the region being milled. This sidewall effect varies slightly between materials but typically creates an amorphous region between 20-50 nm [40,43].

1.4 Solid-Phase Epitaxy

Crystalline oxide thin films are often synthesized through vapor-phase deposition techniques, such as molecular beam epitaxy (MBE) or pulsed laser deposition

(PLD). [44] These synthesis techniques require elevated temperatures to facilitate long-range surface diffusion to form a crystalline phase directly at the substrate-vapor interface and are constrained to planar geometries due to line-of-sight constraints. Some of these limitations can be overcome using a process by which the oxide is deposited at low temperature as an amorphous thin film. Amorphous layers once deposited can be crystallized through the process of solid-phase epitaxy (SPE), which has the potential to create crystalline thin films. [45,46]

The SPE process consists of deposition of an amorphous thin film that is subsequently annealed to transform into a crystalline phase. In the event there are multiple seed crystals, the crystals continue to grow until the thin film is cooled or the crystals meet each other or a different interface. The SPE process allows the creation of crystalline thin films grown at temperatures far lower than those required for vapor-phase epitaxy. This technique also provides a potential route for the formation of crystals with intricate three-dimensional nanoscale geometries. The range of geometries and materials that capitalizes on SPE can be broadened with greater understanding of the fundamental mechanisms governing the crystallization of complex oxide thin films. In chapter 5 I use x-ray nanodiffraction and electron backscatter diffraction (EBSD) to measure the strain and orientation in the crystalline STO. These measurements provide understanding of the role of strain induced by the amorphous-crystalline interface in the growth crystalline STO.

The nucleation and growth of crystalline STO depends strongly on the interface between the substrate and the amorphous thin film. [47] Amorphous STO deposited on the native oxide layer of Si, termed $\text{SiO}_2/(001)$ Si, requires an incubation time for nuclei

to form before the crystalline STO can grow. This knowledge can be used to predict the maximum distance crystalline STO will grow before interacting with crystals nucleated stochastically from elsewhere in the amorphous sample. Alternatively the amorphous thin film grown on a single crystal STO substrate does not require the formation of nuclei because the STO substrate acts like a template for SPE. I have studied the amorphous-crystalline interface in samples in which SPE proceeds laterally from isolated seed crystals on the surface.

Improved understanding of the mechanisms, energetics, and kinetics of SPE has the potential to influence the design of crystalline thin films of complex oxides. SrRuO_3 (SRO) is used as seed crystals to direct the SPE of STO. Amorphous STO will be deposited by sputter deposition on top of the substrate and seed crystals and then annealed at $450\text{ }^\circ\text{C}$ for various times, as depicted in Figure 1.10.

The shapes of the crystalline regions and directional dependent growth velocities will be mapped using the intensity of the crystalline STO Bragg reflections. The known unstrained interface velocity will be compared with the measured lateral interface

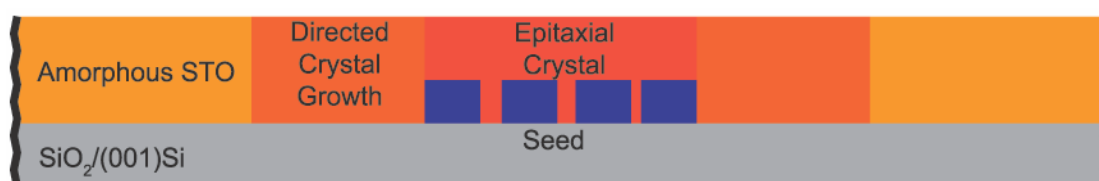


Figure 1.10 Schematic of the growth of an epitaxial STO crystal from a seed crystal.

velocities as a function of strain. Chapter 5 furthers the understanding of the energetics and kinetics of SPE and aid in the creation of crystalline films with complex three-dimensional geometries. The knowledge gained through these experiments will also provide insight into the interaction between thermodynamically stable crystalline phases

and unstable amorphous phases, particularly at the nanoscale, where it has been shown that bulk thermodynamically unstable materials can nucleate and grow. [48]

1.5 References

- [1] D. J. Kim, J. P. Maria, A. I. Kingon, and S. K. Streiffer, *J. Appl. Phys.* **93**, 5568 (2003).
- [2] K. J. Choi, M. Biegalski, Y. L. Li, A. Sharan, J. Schubert, R. Uecker, P. Reiche, Y. B. Chen, X. Q. Pan, V. Gopalan, L.-Q. Chen, D. G. Schlom, and C. B. Eom, *Science* **306**, 1005 (2004).
- [3] C. Donnerer, Z. Feng, J. G. Vale, S. N. Andreev, I. V. Solovyev, E. C. Hunter, M. Hanfland, R. S. Perry, H. M. Rønnow, M. I. McMahon, V. V. Mazurenko, and D. F. McMorrow, *Phys. Rev. B* **93**, 174118 (2016).
- [4] P. G. Radaelli, G. Iannone, M. Marezio, H. Y. Hwang, S. W. Cheong, J. D. Jorgensen, and D. N. Argyriou, *Phys. Rev. B* **56**, 8265 (1997).
- [5] B. Yildiz, *MRS Bull.* **39**, 147 (2014).
- [6] M. Osada, G. Takanashi, B. W. Li, K. Akatsuka, Y. Ebina, K. Ono, H. Funakubo, K. Takada, and T. Sasaki, *Adv. Funct. Mater.* **21**, 3482 (2011).
- [7] K. Kerman and S. Ramanathan, *J. Mater. Res.* **29**, 320 (2013).
- [8] S. Yoon, A. E. Maegli, L. Karvonen, S. K. Matam, A. Shkabko, S. Riegg, T. Grobmann, S. G. Ebbinghaus, S. Pokrant, and A. Weidenkaff, *J. Solid State Chem.* **206**, 226 (2013).
- [9] S. E. Thompson, M. Armstrong, C. Auth, M. Alavi, M. Buehler, R. Chau, S. Cea, T. Ghani, G. Glass, T. Hoffman, C. H. Jan, C. Kenyon, J. Klaus, K. Kuhn, Z. Ma, B. McIntyre, K. Mistry, A. Murthy, B. Obradovic, R. Nagisetty, P. Nguyen, S. Sivakumar, R. Shaheed, L. Shifren, B. Tufts, S. Tyagi, M. Bohr, and Y. El-Mansy, *IEEE Trans. Electron Devices* **51**, 1790 (2004).

- [10] A. M. Jones, J. L. Jewell, J. C. Mabon, E. E. Reuter, S. G. Bishop, S. D. Roh, and J. J. Coleman, *Appl. Phys. Lett.* **74**, 1000 (1999).
- [11] M. El Kurdi, M. Prost, A. Ghrib, S. Sauvage, X. Checoury, G. Beaudoin, I. Sagnes, G. Picardi, R. Ossikovski, and P. Boucaud, *ACS Photonics* **3**, 443 (2016).
- [12] P. H. Lim, S. Park, Y. Ishikawa, and K. Wada, *Opt. Express* **17**, 16358 (2009).
- [13] D. M. Paskiewicz, D. E. Savage, M. V Holt, P. G. Evans, and M. G. Lagally, *Sci. Rep.* **4**, 4218 (2014).
- [14] M. J. Aziz, in *Crucial Issues Semicond. Mater. Process. Technologies* (NATO Adv. Sci. Inst. Ser., 1992), pp. 465–476.
- [15] J. A. Tilka, J. Park, K. C. Sampson, Z. Cai, and P. G. Evans, *APL Mater.* **4**, 126108 (2016).
- [16] J. A. Tilka, J. Park, Y. Ahn, A. Pateras, K. C. Sampson, D. E. Savage, J. R. Prance, C. B. Simmons, S. N. Coppersmith, M. A. Eriksson, M. G. Lagally, M. V. Holt, and P. G. Evans, *J. Appl. Phys.* **120**, 15304 (2016).
- [17] J. A. Tilka and E. Mueller, (2016)
<http://xray.engr.wisc.edu/nanobeamsimulation/html/index.php>.
- [18] H. Yan, O. Kalenci, I. C. Noyan, and J. Maser, *J. Appl. Phys.* **104**, (2008).
- [19] A. Ying, B. Osting, I. C. Noyan, C. E. Murray, M. Holt, and J. Maser, *J. Appl. Cryst.* **43**, 587 (2010).
- [20] E. E. Fullerton and I. K. Schuller, *Phys. Rev. B* **45**, 9292 (1992).
- [21] U. Pietsch, V. Holy, and T. Baumbach, *High-Resolution X-Ray Scattering: From Thin Films to Lateral Nanostructures*. (Springer, Berlin, 2004).
- [22] J. Park, Y. Ahn, J. A. Tilka, K. C. Sampson, D. E. Savage, J. R. Prance, C. B.

- Simmons, M. G. Lagally, S. N. Coppersmith, M. A. Eriksson, M. V. Holt, and P. G. Evans, *APL Mater.* **4**, 66102 (2016).
- [23] M. A. Lutz, R. M. Feenstra, F. K. Legoues, P. M. Mooney, and J. O. Chu, *Appl. Phys. Lett.* **724**, 724 (1995).
- [24] P. G. Evans, P. P. Rugheimer, M. G. Lagally, C. H. Lee, A. Lal, Y. Xiao, B. Lai, and Z. Cai, *J. Appl. Phys.* **97**, 103501 (2005).
- [25] C. S. Ritz, H. J. Kim-Lee, D. M. Detert, M. M. Kelly, F. S. Flack, D. E. Savage, Z. Cai, P. G. Evans, K. T. Turner, and M. G. Lagally, *New J. Phys.* **12**, 103011 (2010).
- [26] P. M. Mooney and J. O. Chu, *Annu. Rev. Mater. Sci.* 335 (2000).
- [27] J. Als-Nielsen and D. McMorrow, *Elements of Modern X-Ray Physics*, Second Edition (John Wiley & Sons, Ltd, 2011).
- [28] A. C. Thompson, D. T. Attwood, E. M. Gullikson, M. R. Howells, J. B. Kortright, A. L. Robinson, J. H. Underwood, K.-J. Kim, J. Kirz, I. Lindau, P. Pianetta, H. Winick, G. P. Williams, and J. H. Scofield, *X-Ray Data Booklet*, Second Edition (2001).
- [29] C. Thiele, K. Dörr, O. Bilani, J. Rödel, and L. Schultz, *Phys. Rev. B* **75**, 54408 (2007).
- [30] T. L. Meyer, L. Jiang, S. Park, T. Egami, and H. N. Lee, *APL Mater.* **3**, 126102 (2015).
- [31] M. P. Cosgriff, P. Chen, S. S. Lee, H. J. Lee, L. Kuna, K. C. Pitike, L. Louis, W. D. Parker, H. Tajiri, S. M. Nakhmanson, J. Y. Jo, Z. Chen, L. Chen, and P. G. Evans, *Adv. Electron. Mater.* **2**, 1500204 (2016).

- [32] R. J. Zeches, M. D. Rossell, J. X. Zhang, A. J. Hatt, Q. He, C.-H. Yang, A. Kumar, C. H. Wang, A. Melville, C. Adamo, G. Sheng, Y.-H. Chu, J. F. Ihlefeld, R. Erni, C. Ederer, V. Gopalan, L. Q. Chen, D. G. Schlom, N. A. Spaldin, L. W. Martin, and R. Ramesh, *Science* **326**, 977 (2009).
- [33] D. G. Schlom, L.-Q. Chen, C. Eom, K. M. Rabe, S. K. Streiffer, and J. Triscone, *Annu. Rev. Mater. Res.* **37**, 589 (2007).
- [34] M. Dawber, K. M. Rabe, and J. F. Scott, *Rev. Mod. Phys.* **77**, 1083 (2005).
- [35] H. Yin, R. Huang, K. D. Hobart, Z. Suo, T. S. Kuan, C. K. Inoki, S. R. Shieh, T. S. Duffy, F. J. Kub, and J. C. Sturm, *J. Appl. Phys.* **91**, 9716 (2002).
- [36] P. M. Mooney, G. M. Cohen, J. O. Chu, and C. E. Murray, *Appl. Phys. Lett.* **84**, 1093 (2004).
- [37] D. G. Schlom, L.-Q. Chen, C. J. Fennie, V. Gopalan, D. A. Muller, X. Pan, R. Ramesh, and R. Uecker, *MRS Bull.* **39**, 118 (2014).
- [38] C. A. Volkert and A. M. Minor, *MRS Bull.* **32**, 389 (2007).
- [39] J. Melngailis, *J. Vac. Sci. Technol. B* **5**, 469 (1987).
- [40] S. Rubanov and P. R. Munroe, *J. Microsc.* **214**, 213 (2004).
- [41] C. R. Hutchinson, R. E. Hackenberg, and G. J. Shiflet, *Ultramicroscopy* **94**, 37 (2003).
- [42] H. L. Cai, X. S. Wu, and J. Gao, *Chem. Phys. Lett.* **467**, 313 (2009).
- [43] D. Kiener, C. Motz, M. Rester, M. Jenko, and G. Dehm, *Mater. Sci. Eng. A* **459**, 262 (2007).
- [44] J. L. Macmanus-Driscoll, *Adv. Funct. Mater.* **20**, 2035 (2010).
- [45] H. Ishiwara, H. Yamamoto, S. Furukawa, M. Tamura, and T. Tokuyama, *Appl.*

Phys. Lett. **43**, 1028 (1983).

- [46] K. Taira, Y. Hirose, S. Nakao, N. Yamada, T. Kogure, T. Shibata, T. Sasaki, and T. Hasegawa, ACS Nano **8**, 6145 (2014).
- [47] Y. Chen, M. H. Yusuf, Y. Guan, R. Jacobson, M. G. Lagally, S. E. Babcock, T. F. Kuech, and P. G. Evans, ASC Nano - Submitt. (2017).
- [48] W. Sun, S. Jayaraman, W. Sun, S. Jayaraman, W. Chen, K. A. Persson, and G. Ceder, Proc. Natl. Acad. Sci. **112**, 3199 (2015).

2 Nanoscale Characterization of Si/SiGe Heterostructures: X-ray Nanobeam Experiment and Diffraction Simulation

*Portions of this chapter were published in *Journal of Applied Physics* **120**, 15304 (2016)

2.1 Introduction

A new generation of x-ray scattering and diffraction techniques based on the use of highly coherent tightly focused x-ray beams from hard x-ray light sources has created opportunities to characterize the nanoscale structure of semiconductors. These x-ray methods simultaneously pose significant challenges in the quantitative interpretation of diffraction data. Tightly focused x-ray beams allow the characterization of the distribution of strain, composition, and lattice orientation at length scales of tens of nanometers. Such length scales are relevant to fundamental physical processes in the formation and interaction of structural defects during epitaxy, the patterning of surface features via self-assembly, and the creation of semiconductor devices [1–4]. This chapter centers on advances to analysis techniques and understanding of nanobeam x-ray diffraction characterization of semiconductor heterostructures. The focused nanobeam, sample, and resultant diffraction patterns will be reproduced with simulations that aid in quantitative analysis. Additionally, this will illustrate the role of small changes in the interface between epitaxial layers to diffraction patterns.

Control of the biaxial distortion of Si is important because strain induces interface band offsets and lowers the degeneracy of the conduction band minima of Si [5,6]. A biaxially strained thin film of Si grown between relaxed SiGe layers breaks this degeneracy and further forms a Si quantum well (QW) layer applicable to quantum

devices, but is accompanied by structural effects associated with plastic relaxation [1,6–8]. With control over the lateral variation of strain it becomes possible to incorporate elastic deformation into the design of quantum devices in new ways, including the possibility of creating devices in which quantum wells are defined completely by strain [9]. Understanding and control on the mesoscopic nanometer-to-micron scale is crucial in Si/SiGe and other semiconductor heterostructures. Thus, it has been an important goal of advanced structural characterization techniques.

X-ray characterization is a powerful tool for evaluating the complex structures of thin films, superlattices, semiconductor heterostructures [10]. Expanding existing x-ray characterization techniques and analysis to nanofocused x-ray beams promises to have a similar positive impact. The highly coherent and convergent x-rays produced by nanofocusing optics complicate the well-established parallel beam picture and provide novel opportunities. Significant progress has already been made in understanding how structural information is encoded in coherent x-ray diffraction patterns acquired with highly convergent hard x-ray beams from nanocrystals and two-dimensional structures. The diffraction problem can be considered using the general framework of coherent diffraction imaging techniques [13–15]. Computational methods are used to retrieve the illumination function and to form the images of projections of the strain along specific crystallographic directions or dislocation strain fields [16–19]. Intricate semiconductor heterostructures face challenges associated with the reciprocal-space overlap of scattering features from individual layers and can be analyzed using computational methods simulating and interpreting the experimental results.

The use of convergent nanobeams to probe materials presents a series of challenges because the x-ray beam can no longer be approximated as a plane wave. This chapter reports the development of methods for the quantitative simulation of coherent x-ray nanobeam diffraction and the analysis of nanodiffraction intensity data acquired from Si/SiGe heterostructures from an arbitrary angle of incidence. Wave-optics simulations are used to predict the diffraction patterns. The steps in the simulation begin with a perfectly collimated and monochromatic plane wave at normal incidence to the zone plate. Alternating phases of the concentric zones are imprinted onto the wavefield, which is propagated to the order sorting aperture using the Fresnel approximation where all amplitude outside the order sorting aperture is set to zero. The Fraunhofer approximation is used to propagate the wavefield to the sample, and kinematic diffraction methods are used to model the coherent x-ray Bragg diffraction patterns from a complex heterostructure illuminated at arbitrary angles of incidence.

Previous studies of the distortion of semiconductor structures using x-ray nanobeams have probed a variety of structural issues, but have not yet closed the gap between experiment and simulation of complex heterostructures. Bragg projection ptychography analysis of focused x-ray nanobeam diffraction patterns have provided high-resolution imaging of tilts and strains in silicon-on-insulator test structures and in prototype field-effect transistor channels [20,21]. Similar lattice rotation and distortion effects are observed in ptychography studies of III-V heterostructures [22]. Nanobeam diffraction studies of Si/SiGe structures show that the lattice of the Si QW is distorted by the relaxation of the SiGe substrate, and by stresses imparted on the semiconductor through interfaces with metal electrodes [23,24]. Other nanobeam diffraction studies have

probed the strain distribution over lateral lengths scales of microns in Ge microstripes, in heteroepitaxial Ge, and in SiGe via rapid mapping techniques [25–28]. In semiconductor

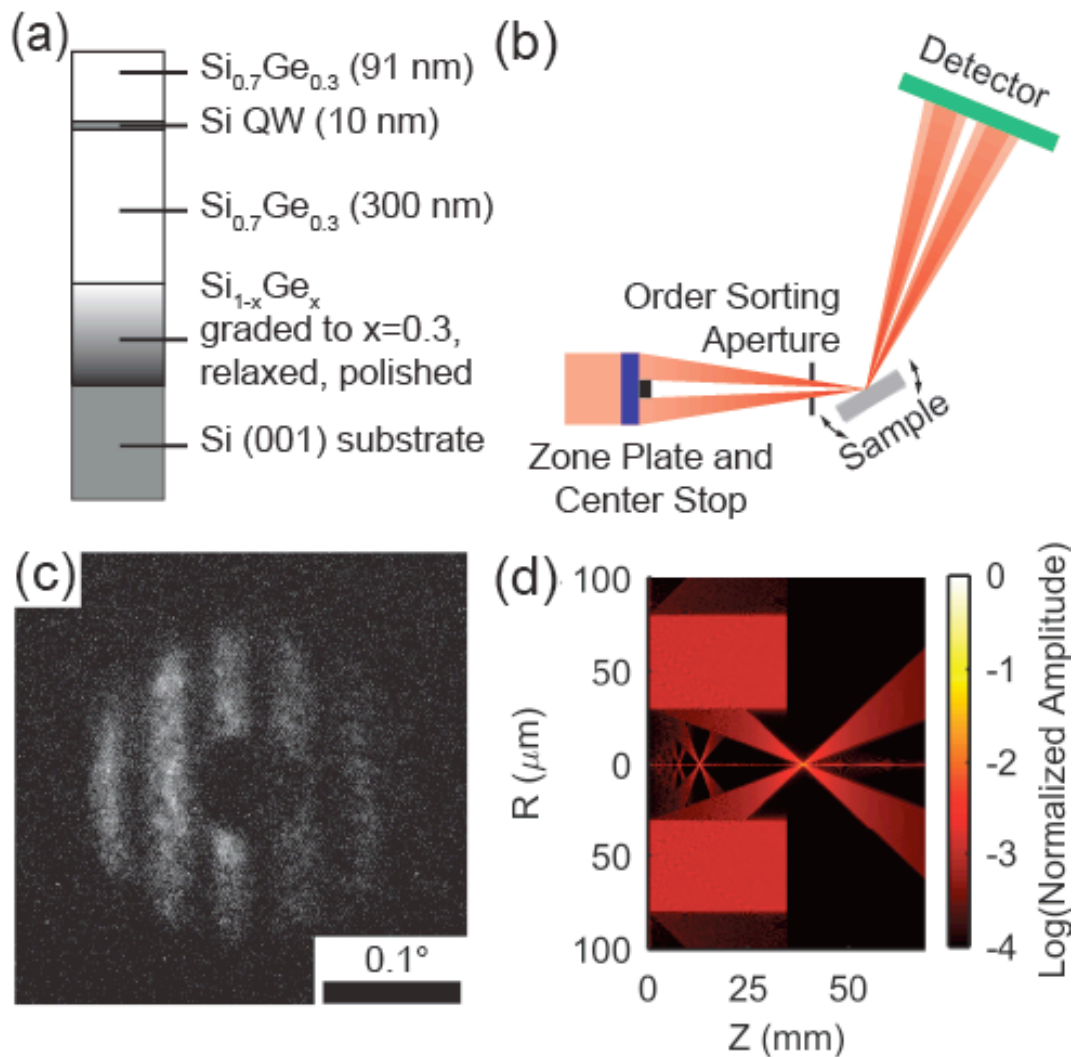


Figure 2.1 (a) Schematic cross section of the Si/SiGe heterostructure grown on a graded SiGe layer on an (001)-oriented Si single crystal substrate. (b) Focused x-ray nanodiffraction geometry using Fresnel zone plate x-ray focusing optics and a two-dimensional CCD detector. Arrows indicate the direction of the sample rotation used to vary the x-ray incident angle. (c) Focused x-ray nanobeam diffraction pattern acquired at an angle close to the Bragg condition of the (004) reflection of the strained-Si QW. Intensity fringes visible as vertical stripes on the diffraction pattern originate from the thickness of the 91 nm-thick top SiGe layer. (d) Radial slice of the three-dimensional simulated wave front propagating from the zone plate to the focus. Cylindrical coordinates Z and R correspond to the distance along the direction between the zone plate and the sample and the distance from the optical axis, respectively.

nanotechnology, x-ray nanobeam techniques provide insight into the distortion of thin semiconductor substrates by self-assembled quantum dots, stresses arising from the freestanding SiGe membranes transferred to a new host substrate, and the effect of patterning the silicon substrate on dislocation formation [29–32]. Advanced analysis techniques will permit the characterization of multilayers, quantum wells, and other intricate heterostructures. This chapter considers, in detail, the nanodiffraction characterization of the Si/SiGe heterostructure shown in Figure 2.1(a), and it demonstrates that the gap between experiment and simulation can be closed.

The key impact of this chapter is the expansion of the quantitative analysis capabilities of nanobeam x-ray diffraction. Much of the previous work involving the simulation of x-ray nanobeam diffraction patterns is based on understanding the diffraction from thin films at a single angle of incidence. The work presented here can simulate more complicated systems relevant in materials engineering including semiconductor heterostructures and complex oxide super lattices. The expansion to an arbitrary angle of incidences is also of significance in materials engineering because x-ray diffraction patterns taken at angle other than the Bragg angle can provide structurally relevant information such as layer thickness. The simulations presented in this chapter have been used to aid in the analysis of Si/SiGe heterostructures. However, the approach is sufficiently broad to be of use for other researchers interested in these complex diffraction patterns, and the simulation has therefore been made available online for general use.

2.2 Experimental Methods

The nanobeam diffraction experiments described in this chapter were performed at the the Hard X-ray Nanoprobe of the Advanced Photon Source at Argonne National Laboratory [33]. The optical configuration of the x-ray measurement is illustrated in Figure 2.1(b). An incident x-ray beam with a photon energy of 10 keV, selected by a two-bounce Si (111) monochromator, was focused to a measured spot size of approximately 50 nm full width at half-maximum (FWHM) at the sample. The focusing optics consisted of a 160 μm -diameter Fresnel zone plate with a 60 μm -diameter center stop. The focusing introduced an overall effective beam divergence of 0.24° . The sample was placed at the first order focus of the zone plate and radiation focused to higher orders was blocked by an order sorting aperture (OSA). The incident angle of the x-rays with respect to the heterostructure was set using the orientation of the sample, as indicated in Figure 2.1(a). The intensity distribution of scattered x-rays was recorded using a two-dimensional charge coupled device (CCD) detector with a pixel size of 13 μm .

The Si/SiGe heterostructure was epitaxially grown using ultrahigh vacuum chemical vapor deposition [23]. A several- μm -thick $\text{Si}_{1-x}\text{Ge}_x$ layer in which the Ge concentration is graded linearly from $x = 0$ to 0.3 was first grown on the (001) Si substrate. During growth, the $\text{Si}_{1-x}\text{Ge}_x$ layer was relaxed forming a network of dislocations arranged in the characteristic cross-hatch pattern [7]. The Si/SiGe heterostructure (91 nm $\text{Si}_{0.7}\text{Ge}_{0.3}$, 10 nm strained-Si QW, 300 nm $\text{Si}_{0.7}\text{Ge}_{0.3}$, 5 nm Si cap layer) was then grown as shown in Figure 2.1(a). A biaxial in-plane tensile strain with a magnitude of approximately 1% is induced in the Si QW by epitaxial growth on the relaxed $\text{Si}_{0.7}\text{Ge}_{0.3}$ layer. The quantum well structures were created by the Eriksson group

in the physics department at UW-Madison before being given to the Evans's group for structural analysis.

2.3 Coherent Diffraction Simulation and Analysis Methods

Diffraction experiments using highly coherent nanobeams produce a complex distribution of scattered intensity. A representative nanobeam diffraction pattern acquired from the Si/SiGe heterostructure is shown in Figure 2.1(c), acquired at an incident angle at which the diffraction pattern exhibits features arising from the (004) Bragg reflection of the strained-Si QW. The incident angle of Figure 2.1(c), $\theta = 27.49^\circ$, corresponds to a nominal wavevector $q_z = 4.68 \text{ \AA}^{-1}$ at the photon energy of this experiment. As discussed in detail through this section, the divergence introduced by the zone plate focusing optics results in the distribution of intensity in the focused x-ray beam of a range of incident angles, a wavevector range $\Delta q_z = 0.038 \text{ \AA}^{-1}$. Interference fringes arising from the 91 nm top SiGe layer have reciprocal space separation of 0.007 \AA^{-1} and thus appear superimposed on the strained-Si QW diffraction pattern in Figure 2.1(c). The 10-nm-thick strained-Si QW produces much more widely spaced thickness fringes separated by 0.063 \AA^{-1} . An example of these widely spaced fringes are apparent as a gradual variation of the scattered intensity across the entire width of the region of the detector illuminated by the divergent zone plate in Figure 2.1(c).

The coherent diffraction patterns were simulated using a method employing the propagation of waves through a system consisting of the focusing optics, the sample, and the x-ray detector. My The approach discussed here was built approach was built on optical methods developed in the group of Prof. Cev Noyan at Columbia University, in collaboration with scientists at Argonne National Laboratory. Their method was reported

in a 2010 paper by Ying *et al.*, which describes the simulation method and a comparison with a very simple silicon-on-insulator sample [14]. Crucially, the work of the Columbia/Argonne group work considered only a single x-ray incidence angle. The work did not describe the sample in a way that would be accurate in the regions of reciprocal space far from the SOI Bragg reflection or allow complex sample structures to be simulated. My work re-creates the numerical methods employed by Ying *et al.* and expanded their approach to allow more complex heterostructures to be considered at arbitrary x-ray incident angles. The simulation procedure consists of calculating the wavefield of the focused x-ray beam produced by the zone plate, computing the wavefield resulting from kinematic diffraction at the sample, and propagating the scattered beam to the detector.

The wavefield of the focused x-ray beam was computed by imprinting the phase imparted by the zone plate onto an incident x-ray plane wave and by propagating the wavefield to the sample using Fresnel diffraction [14]. The simulation was based on zone plate parameters matching the experimental conditions. The Fresnel zone plate was modeled using a binary approximation with Au zones, an outermost zone width of 30 nm, thickness of 400 nm, and diameter of 160 μm . The focal length for this model zone plate at 10 keV was 39 mm, matching the experiment. Simulations assumed a perfectly monochromatic beam and thus did not take into account the finite energy bandwidth of the monochromator. The simulated center stop consisted of an Au cylinder with a diameter of 60 μm and a thickness of 70 μm . The simulated order sorting aperture consisted of a circular aperture with a diameter of 30 μm located 4 mm from the focus. The amplitude outside the aperture of the OSA was set to zero. The intensity of the

focused wavefield produced using this approach is plotted in Figure 2.1(d), yielding a focal spot diameter of 40 nm FWHM. The distribution of intensity is similar to the report by Ying *et al.*, and to other previous reports [14,16,17].

The relationship between the incident and scattered beams was determined by summing the amplitude of radiation scattered by each plane of atoms in the sample. Absorption and multiple scattering were neglected. The amplitude of the scattered beam was simulated by computing the lattice sum of the sample in a coordinate system consistent with its orientation and using the kinematic approximation. Absorption is safely neglected because the SiGe and Si layers are much narrower than their respective attenuation lengths of 109 μm and 134 μm . The lattice of thin films is effectively infinite in the in-plane directions, so the lattice sums along those directions can be replaced with delta functions. For the out-of-plane direction close to the surface normal, the lattice sum for one of the component layers (e.g. the 10 nm Si QW) of a multilayer thin film was computed using:

$$S_1(Q_z) = F_1(Q_z) \sum_{n=0}^{N_1-1} e^{iQ_z(a_1n-z_1)} .$$

Equation 2.1

Here F_1 is the structure factor of an individual unit cell, N_1 is the number of unit cells in the out-of-plane z direction composing this layer, Q_z is the scattering wavevector along z , a_1 is the lattice parameter along this direction, and z_1 is the overall vertical location of the bottom unit cell within the stack of layers within the heterostructure, which is an important consideration when multiple layers are considered as shown in Figure 2.2. The sum for the first component layer becomes:

$$S_1(Q_z) = F_1(Q_z) \frac{\sin \frac{1}{2} Q_z N_1 a_1}{\sin \frac{1}{2} Q_z a_1} e^{\frac{i Q_z ((N_1-1)a_1 - 2z_1)}{2}} .$$

Equation 2.2

With the addition of a second layer with structure factor F_2 , number of unit cells N_2 and lattice parameter a_2 at location z_2 , the total lattice sum is:

$$S_{1+2}(Q_z) = F_1(Q_z) \frac{\sin \frac{1}{2} Q_z N_1 a_1}{\sin \frac{1}{2} Q_z a_1} e^{\frac{i Q_z ((N_1-1)a_1 - 2z_1)}{2}} + F_2(Q_z) \frac{\sin \frac{1}{2} Q_z N_2 a_2}{\sin \frac{1}{2} Q_z a_2} e^{\frac{i Q_z ((N_2-1)a_2 - 2z_2)}{2}} .$$

Equation 2.3.

This approach is sufficiently general to be applied to an arbitrary number of layers of different crystal structure, compositions, and thickness for thin film type structures

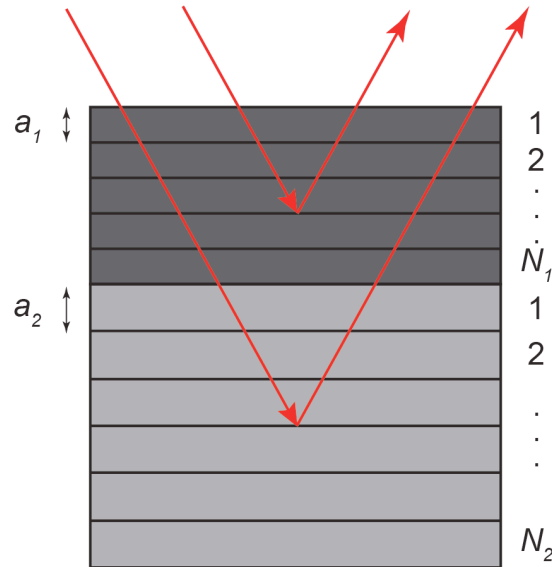


Figure 2.2 The lattice sum method with multiple layers. Here the material represented in dark gray is N_1 layers thick with a lattice parameter of a_1 , and the material represented in light gray is N_2 layers thick with a lattice parameter of a_2 .

provided that the total thickness is far less than the x-ray absorption length. The assumption that multiple scattering and absorption can be neglected is valid for the small thicknesses of the Si and SiGe layers in the present study, and the range of Q considered

is sufficiently narrow that the structure factor for an individual unit cell, $F(Q)$, is treated as a constant. The lattice sum is evaluated at the Q values calculated from the simulated wavefield of the focused beam after the coordinate frame is rotated to the desired diffraction geometry by the rotation matrix:

$$T_i = \begin{bmatrix} \sin\theta & 0 & \cos\theta \\ 0 & 1 & 0 \\ -\cos\theta & 0 & \sin\theta \end{bmatrix}.$$

Equation 2.4

The coordinate frame is rotated to the detector by the rotation matrix:

$$T_d = \begin{bmatrix} \sin(\theta - 2\theta_B) & 0 & \cos(\theta - 2\theta_B) \\ 0 & 1 & 0 \\ -\cos(\theta - 2\theta_B) & 0 & \sin(\theta - 2\theta_B) \end{bmatrix}.$$

Equation 2.5

Here the x-axis is in the scattering plane along a radial direction with respect to the optical axis, the z-axis is along the direction of propagation of the focused x-ray beam, θ is the incident angle of the center of the incoming x-ray beam, θ_B is the Bragg angle, and the origin is at the focus. These matrices are valid for symmetric, out of plane geometries, but could be generalized to allow for arbitrary diffraction conditions.

The simulations described here consider only the 91 nm thick SiGe layer and 10 nm thick strained-Si QW layer, as illustrated in Figure 2.3(a). The 300 nm thick bottom SiGe layer can be neglected because the interface between the 300 nm SiGe and the graded SiGe is too rough to have a well-defined sharp boundary, and interference fringes from these layers are absent from the experimental detector images. The total experimentally observed intensity of the SiGe reflection may, however, include a

contribution from the bottom SiGe layer and thus will not be accurately simulated by this two-layer model. The deeper, graded SiGe layer had a wide range of orientations over a total mosaicity of 0.5° resulting from the plastic relaxation process and did not produce a

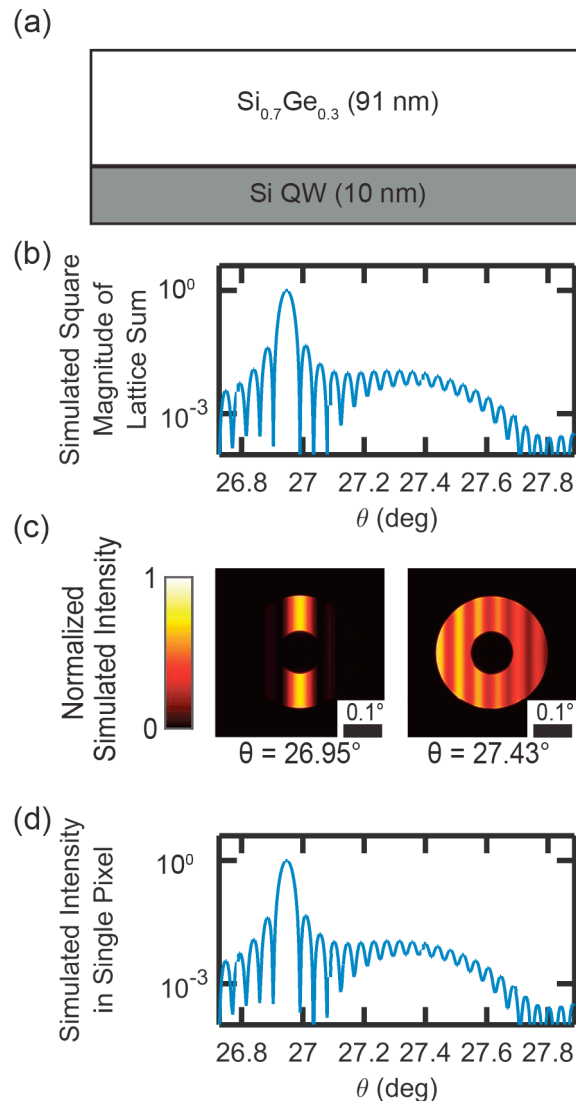


Figure 2.3 (a) Schematic of the model sample used to create the simulated diffraction pattern. (b) Simulated θ - 2θ diffraction pattern created using the lattice sum of the model. The reflections centered at 26.95° and 27.45° arise from the SiGe and strained-Si QW layers, respectively. (c) Simulated diffraction patterns for x-ray incident angles of $\theta=26.95^\circ$ and $\theta=27.43^\circ$. Detector images in part (c) are each normalized to the maximum intensity in each image. (d) Simulated θ - 2θ scan produced by integrating the diffracted intensity in the wave-field simulation over the area of a single pixel of the two dimensional detector.

rod of scattering aligned with the quantum well and capping layer. Similarly, diffraction from the Si substrate and the Si substrate crystal truncation rod were at sufficiently

different orientations that the substrate could be neglected in the simulation. The out-of-plane lattice parameters for Si and SiGe were $a_1=5.387 \text{ \AA}$ and $a_2=5.472 \text{ \AA}$, respectively. With these values, the square magnitude of the lattice sum produced is shown in Figure 2.3(b), plotted as a function of incident x-ray angle θ , with $Q_z = (4\pi\sin\theta)/\lambda$, as would be appropriate for plane-wave illumination.

The lattice sum was rotated into a coordinate system by the incident x-ray angle θ , which allowed the scattered amplitudes to be calculated. Simulated diffraction patterns were produced by propagating the scattered beam to the plane of the detector and recording the square magnitude of the electric field. Images produced in this way are shown in Figure 2.3(c) for incident angle $\theta=26.95^\circ$, an angle corresponding to the most intense scattering from the 91 nm SiGe layer, and $\theta=27.43^\circ$, corresponding to the strained-Si QW layer. The distribution of intensity within the images qualitatively appears to be similar to the intensity distribution along the Q_z direction of the lattice sum. This intensity distribution will be systematically compared to the experimental results below.

The correspondence between the lattice sum and the simulated diffraction pattern can also be confirmed by calculating the intensity falling within an angular range corresponding to a single pixel of the x-ray detector used in the experiment. A simulated θ - 2θ scan produced by computing the intensity scattered into a single-pixel-wide region of the simulated detector is shown in Figure 2.3(d). Intensity features significantly narrower than the total angular range of the zone plate can be simulated accurately as shown by comparing Figure 2.3(b) and Figure 2.3(d). The key result of Figure 2.3(b) and Figure 2.3(d) is that high-resolution diffraction patterns can be experimentally extracted

from experiments with highly divergent coherent x-ray beams, and that these patterns can be subsequently compared with lattice-sum simulations.

One of the most powerful aspects of this simulation approach is the ability to be extended to a wide range of sample composition and angles of incidence. To capitalize on

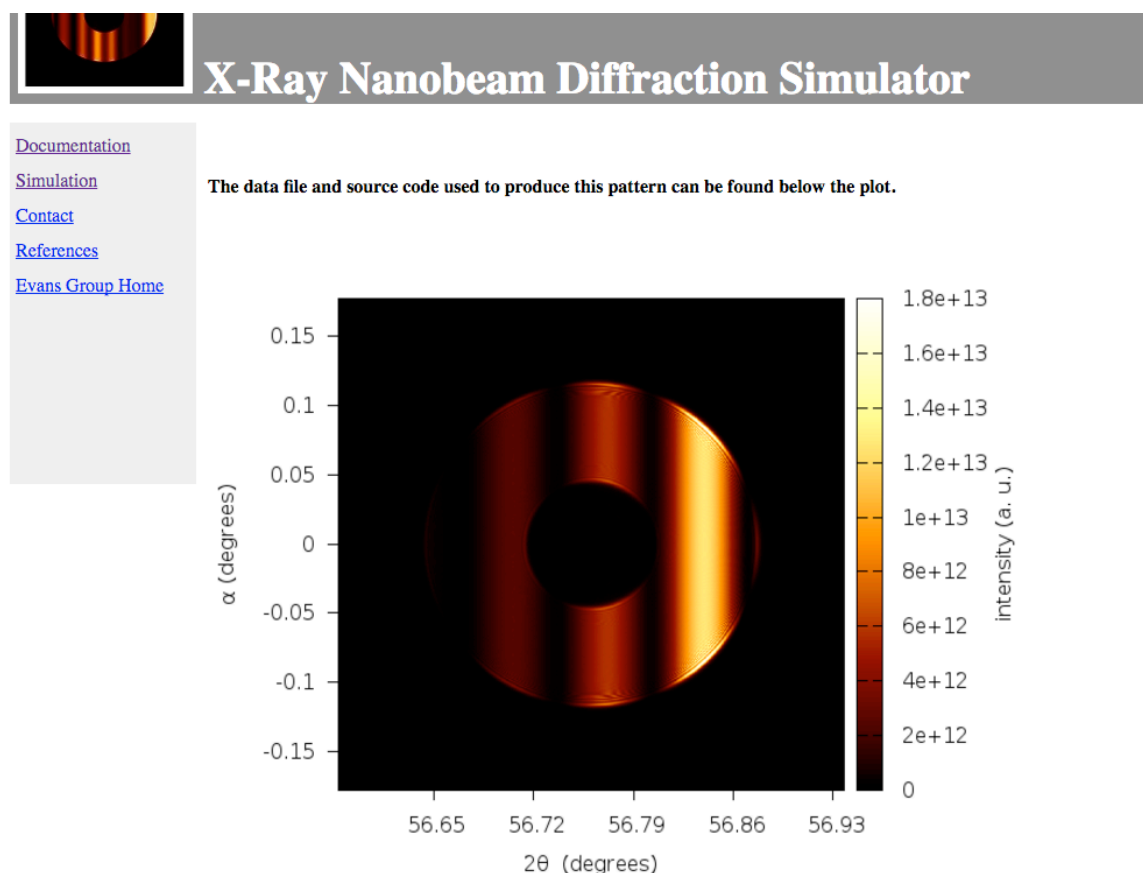


Figure 2.4 Screen shot of the webpage made available to those interested in x-ray nanodiffraction at <http://xray.engr.wisc.edu/nanobeamsimulation/html/index.php>.

that flexibility and to increase the impact of the work presented here, an online simulator has been created for use to anyone who interested in quickly and quantitatively visualizing nanobeam diffraction patterns generated from synchrotron sources. A screen shot of the website it shown in Figure 2.4.

The simplest comparison between the simulation and the nanobeam diffraction data can be obtained by integrating the scattered intensity over the entire angular range

spanned by the zone plate divergence. Simulated and experimentally acquired θ - 2θ scans produced in this way appear in Figure 2.5. The analysis presented in Figure 2.5, however,

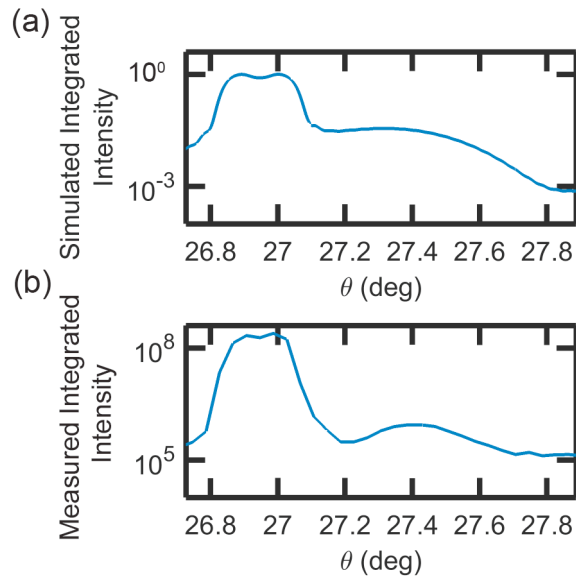


Figure 2.5 (a) Simulated θ - 2θ scan produced by a wave field simulation of the focused beam that has been integrated to include all of the intensity provided by the focusing optics. (b) Measured θ - 2θ scan produced by integrating the intensity over an area greater than the whole image of the zone plate on the detector. The angular resolution is set by the width of the zone plate, which broadens the narrow SiGe peak and eliminated the narrow thickness fringes.

does not take advantage of the high degree of coherence of the focused x-ray beam, and thus does not allow the high spatial frequency features in the sample structure to be resolved. The interference fringes arising from the 91 nm SiGe layer, for example, are absent from Figure 2.5 because range of wavevectors spanned by the zone plate convergence angular width, $\Delta q_z = 0.038 \text{ \AA}^{-1}$, is greater than the spacing between the SiGe fringes, $\Delta q_z = 0.007 \text{ \AA}^{-1}$. At incident angles near the SiGe peak at $\theta = 26.95^\circ$, the sharp SiGe reflection appears throughout the range of angles subtended by the zone plate and the integrated intensity across the entire zone plate is approximately constant. The simulated SiGe reflection in Figure 2.5(a) thus has the angular width expected from the divergence of the zone plate, $\theta = 0.24^\circ$, rather than the intrinsic angular width set by the

thickness of the SiGe layer. The dip in the intensity near the center of the SiGe peak in both simulation and experiment arises from the obstruction of the center of the zone plate by the center stop. A higher total intensity occurs when the sample is misoriented with respect to the center of the x-ray beam but at a sufficiently small angle that some portion of the divergent beam still meets the Bragg condition. The minimum between the SiGe and Si QW peaks at $\theta = 27.19$ is less pronounced in the simulated data than the experimental data because the intensity of interference fringes depends on the interface structure, which is not a parameter included in this model. A small difference between the simulation and experimental data in Figure 2.5 is in the intensity of the SiGe reflection. The experimental data like includes a contribution from the 300 nm SiGe buffer layer that was not considered in the simulation. Analysis using the integration off the full angular range of the zone plate, as in Figure 2.5, does not capture key structural features.

More detailed structural insight can be obtained by comparing the simulated intensity distribution with the experimental diffraction patterns. A high-resolution comparison of experimentally acquired and simulated diffraction patterns is shown in Figure 2.6. Figure 2.6(a) shows the lattice sum prediction of a θ - 2θ scan. Simulated and experimental diffraction patterns acquired in the angular region near the SiGe (004) reflection are shown in Figure 2.6(b), at incident angles indicated by the blue ticks in Figure 2.6(a). At the incident angle at which the center of the zone plate meets the SiGe (004) Bragg reflection, the shadow of the center stop appears at the center of the diffraction pattern. In the adjacent images, acquired at incident angles different by steps of 0.04° , a vertical stripe of intensity appears because the difference between the actual incident angle and the nominal SiGe Bragg angle is less than the divergence of the zone

plate. The angular separation between the center of the zone plate and the SiGe diffracted intensity changes with varying incident angle. Note that the angular width of the central

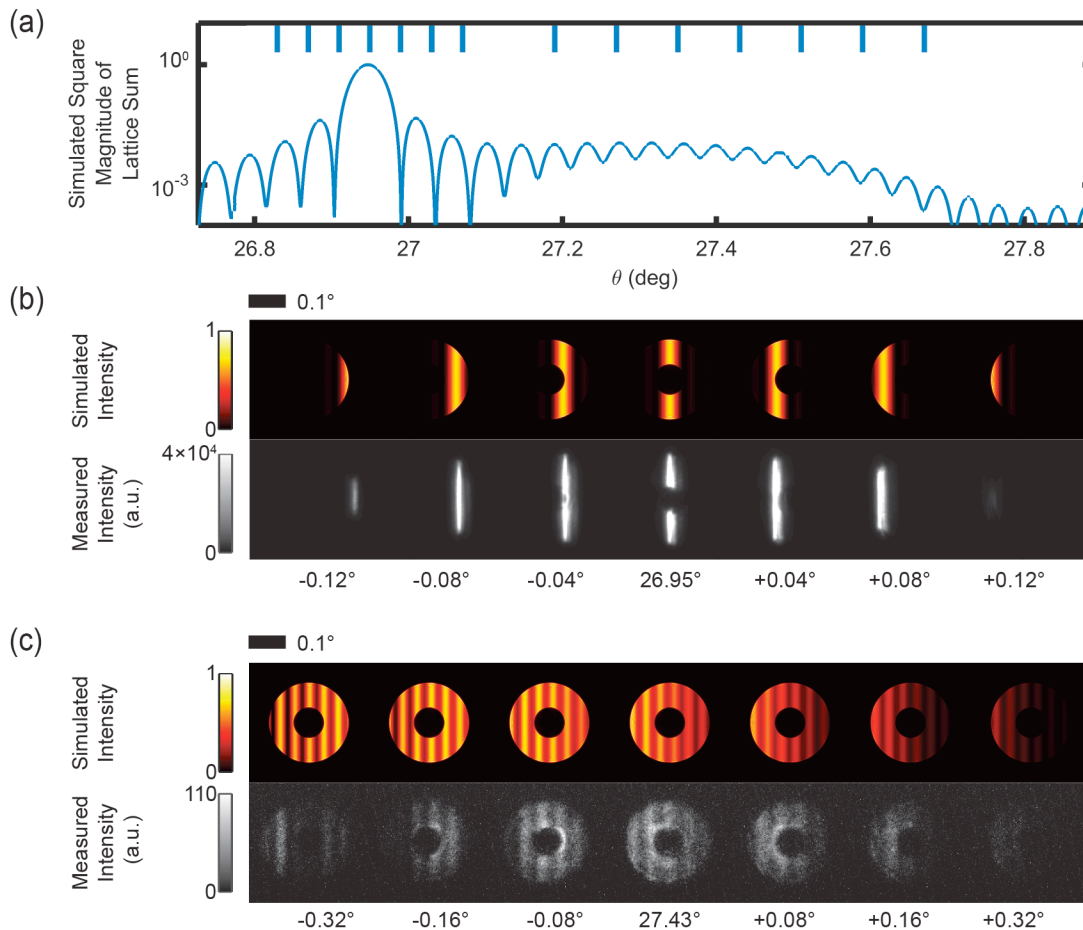


Figure 2.6 (a) Simulated θ - 2θ scan using the lattice sum method. Blue lines on the top axis correspond to the values of the incident angle where experimental and simulated diffraction patterns are shown below. (b) Simulated (top row) and experimental (bottom row) diffraction patterns acquired near the SiGe (004) reflection. (c) Simulated (top row) and experimental (bottom row) diffraction patterns acquired at the strained-Si QW (004) reflection.

fringe of the SiGe reflection is much narrower than the zone plate divergence.

Simulated and experimentally acquired intensity distributions for incident angles near the Bragg condition of the strained-Si QW are shown in Figure 2.6(c). The central image of Figure 2.6(c) has an incident angle $\theta = 27.43^\circ$ and the remaining images were acquired at 0.08° steps from this value. The thinness of the Si QW causes its intensity to

be distributed across a wide range of angles, nearly matching the zone plate divergence. As the incident angle increases from values less than the nominal Bragg angle to larger values, the intensity range spanned by the images moves from the region of the intensity minimum between the SiGe peak and the strained-Si QW peak, to the strained-Si QW peak, and then to the low-intensity range at higher angles. Interference fringes from the SiGe layer appear as vertical stripes moving across diffraction patterns in Figure 2.6(c).

The systematic comparison of simulated and experimental diffraction patterns can be used to extract structural information from small areas of the Si/SiGe heterostructure. Previous studies with smaller-numerical-aperture optics (and thus smaller beam divergence) have shown that the orientation of the strained-Si QW varies from location to location along the surface because of the randomness in the relaxation of the SiGe layer [23]. The variation in the orientation of the strained-Si QW leads to variation in the intensity and angular position of the diffracted beam. The variation in the intensity of the diffracted beam is very small in the present case because the divergence of the incident x-ray beam and the high width of the strained-Si QW reflection combine to make the effective angular widths of the reflections very broad. Figure 2.7(a) shows a spatial map of the integrated intensity in a region with a width of 1.5 μm , using diffraction patterns acquired with a fixed angle of $\theta = 27.49^\circ$. The variation of the integrated intensity of the diffracted beam within the area imaged in Figure 2.7(a) is extremely small, varying by 0.3%. Changes in the orientation are not sufficiently large to move the reflection off of the Bragg condition. Changes in the total thickness across this area are similarly small.

Differences in the orientation of the Si QW lead to systematic variation in the observed diffraction patterns across the area imaged in Figure 2.7(a). The nanobeam

diffraction patterns shown in Figure 2.7(b) correspond to the two locations indicated in Figure 2.7. These locations are separated by 500 nm and acquired with the same incident

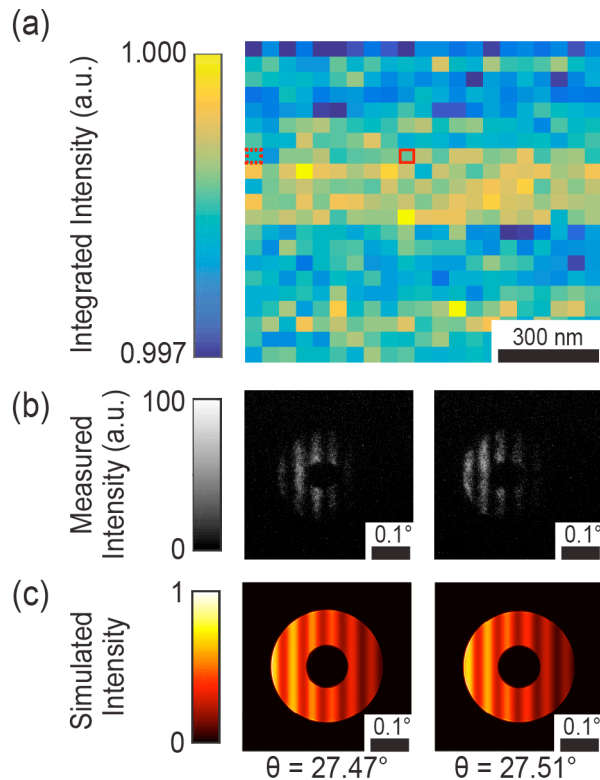


Figure 2.7 (a) Map of the integrated intensity of individual diffraction patterns at a fixed incident angle. (b) Focused x-ray nanobeam diffraction patterns measured at points indicated by the dotted and solid red boxes in (a). (c) Simulated diffraction patterns for two different effective incident angles with respect to the strained-Si QW.

angle, $\theta = 27.49^\circ$. The diffracted intensity at the two locations is distributed to different angles due to the difference in the local orientation of the Si QW. The orientation of the Si QW is determined by the local orientation of the SiGe buffer layer, which exhibits variations due to the randomness of the plastic relaxation during growth [8]. The orientation of the SiGe and Si QW layers thus vary simultaneously and the series of fringes across the Si QW due to the SiGe thickness are observed in each location.

Diffraction patterns acquired at intermediate locations between the endpoint positions, Figure 2.7(b), exhibit a gradual shift of the angular location of the diffracted

intensity between adjacent images. This shift indicates that the strained-Si QW lattice is gradually rotated through the difference in orientations. This is coincidentally approximately equal to angular spacing between fringes, 0.045° . The simulated diffraction patterns for these two orientations are shown in Figure 2.7(c), and are in agreement with the observed intensity. The two local incident angles (measured with respect to the planes of the strained-Si QW) were 27.47° and 27.51° , respectively.

2.4 Influence of Interfacial Structure on Diffraction

The simulations produced and evaluated in this chapter can be broadened to aid in the understanding of the role of interfaces between epitaxial layers. The simulated and

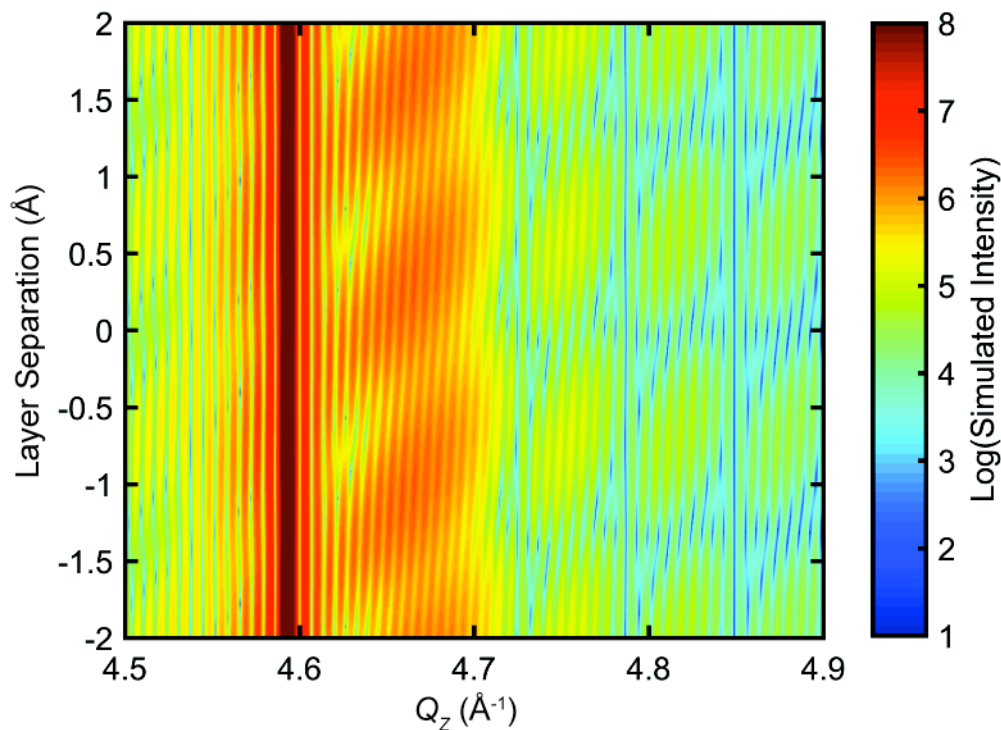


Figure 2.8 Lattice sum of the Si/SiGe heterostructure as a function of reciprocal lattice vector and layer separation. The highest intensity region at 4.59 \AA^{-1} is the Bragg peak of the SiGe layer.

experimental diffraction patterns of the Si QW and SiGe (004) peak have some key differences attributed to the interfacial structure between the two layers. In particular, the

interference pattern between the Si QW layer and the SiGe layer leads to a broad minimum in intensity between the Si QW peak and the SiGe peak that is not a function of either independent layer. The minimum in intensity is more pronounced in the experimental data than in the simulated data shown previously. One critical assumption in the simulated data shown previously is that each layer contains an integer number of unit cells, and that that number is constant over the region illuminated by the beam. The former assumption can be relaxed in the simulation by allowing one-quarter unit cells to exist at the interface between the two layers, which produces the Figure 2.8.

Interfacial lattice steps with heights smaller than unit cells in the Si QW and SiGe layer are physically reasonable because the diamond unit cell structure shared by Si and

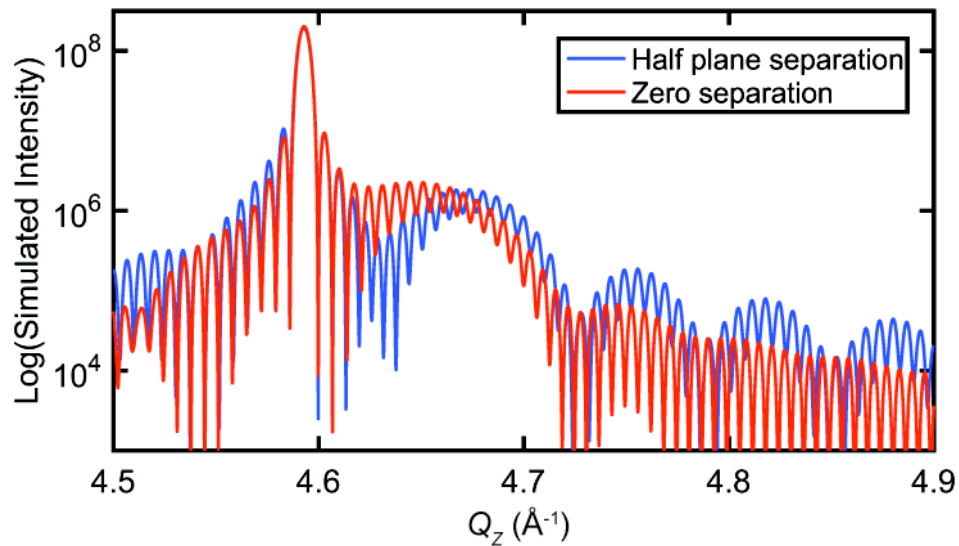


Figure 2.9 Two line profiles of the lattice sum calculated in Figure 2.8. The blue simulation is the result of the interference between the two layers when half a layer of empty space is added.

SiGe is made up of four distinct planes of atoms in the out-of-plane direction. Therefore, one-quarter unit cell corresponds to one atomic plane. The interfacial structure of the epitaxial Si QW and SiGe layers could reasonably include fractions of unit cells of one or

both layers due to the thicknesses being slightly different from an integer number of unit cells, steps at the interface, or some combination of the two factors.

In order to account for the difference between the amplitude and intensities of the broader thickness fringes arising from the thin Si WQ layer in the simulation, the diffraction pattern was plotted as a function of increasing distance between the two layers without adding additional atomic planes. The addition of a vacuum layer changes the interference of the two diffraction patterns with each other due to the phase change associated with their relative locations, while keeping the total scattered intensity constant. The plot shown in Figure 2.8 shows a periodicity related to exactly one-quarter of the average lattice parameter of the structure, which means that the phase offset between the two layers is periodically repeating with every atomic step. The periodicity is expected because it matches the periodic structure of the crystal itself. This information could be used to better estimate the interfacial structure between the two layers.

A second effect apparent in the simulations of different interface structures is the estimation of the lattice parameter of the Si QW. The change in the depth of local minimum in the diffraction pattern alters the apparent location of the peaks of the x-ray reflection arising from the Si QW layer as shown in Figure 2.9. Interestingly, this interfacial phenomenon could unexpectedly influence the nominal lattice parameter of thin layers in complex heterostructures as observed through x-ray diffraction techniques. The simple application of the Bragg equation to find interatomic spacing may need more careful consideration in quantum well devices.

2.5 Conclusion

The combination of nanobeam diffraction experiments with the simulation methods presented here allows key features in thin film heterostructures to be determined precisely. The synthesis of semiconductor heterostructures often results in the creation of structural defects, lattice misorientation and tilts, or interfacial atomic steps which can have an impact on the performance or stability of devices. The Si/SiGe system discussed here is, for example, a promising route to quantum devices, but requires further understanding the role of defects and interface features to be developed. Such features can have a negative impact on conduction band valley-splitting and can reduce device performance [34–36]. If such features can be mastered, Si and SiGe offer to allow quantum devices to be created using the low spin-orbit coupling and zero nuclear spin of Si, the high tunability of SiGe alloys' electronic properties with composition, and the facilitated integration of III-V semiconductor materials [31,37].

The results presented here demonstrate and experimentally confirm a versatile coherent diffraction modeling approach for the interpretation of far-field intensities using a highly convergent hard x-ray nanobeam. The model evaluated in this chapter faithfully reproduces the angular distribution of diffracted x-ray intensity within a range narrower than the divergence of the zone plate. Insight into the diffraction patterns produced with highly divergence x-ray beams allows for the robust quantitative analysis of these complex diffraction patterns.

These methods provide insight into structural parameters of a wider range of heteroepitaxial materials, complex oxides, super lattices, and can be very broadly applied in cases where existing coherent diffraction methods cannot yet be applied. Additionally,

work is currently ongoing to extend these methods to incorporate the effects of dynamical diffraction in systems with lattice matches substrates. Beyond this Si/SiGe system and the relevant semiconducting materials, the simulation approach described here can be applied to other important heterostructures including complex oxides such as $\text{Pb}(\text{Zr},\text{Ti})\text{O}_3$ (PZT), or ferroelectric superlattices where the lattice strain distribution is one among different parameters which lead to the formation of exotic polarization domains [38–40].

Other coherent diffraction analysis methods, including phase retrieval methods such as coherent diffraction imaging or ptychography, have so far been based on the analysis of well-defined isolated reciprocal-space distributions of the scattered x-ray intensity. When diffraction signals that stem from layers with different lattice spacings significantly overlap, solving for the phase component of the crystal electron density becomes complicated. The simulations described here provide key insight when phase retrieval approaches are compromised by the presence of multiple layers with similar lattice parameters that simultaneously contribute to the intensity patterns.

2.6 References

- [1] M. A. Lutz, R. M. Feenstra, F. K. Legoues, P. M. Mooney, and J. O. Chu, Appl. Phys. Lett. **724**, 724 (1995).
- [2] P. G. Evans, P. P. Rugheimer, M. G. Lagally, C. H. Lee, A. Lal, Y. Xiao, B. Lai, and Z. Cai, J. Appl. Phys. **97**, 103501 (2005).
- [3] C. S. Ritz, H. J. Kim-Lee, D. M. Detert, M. M. Kelly, F. S. Flack, D. E. Savage, Z. Cai, P. G. Evans, K. T. Turner, and M. G. Lagally, New J. Phys. **12**, 103011 (2010).
- [4] P. M. Mooney and J. O. Chu, Annu. Rev. Mater. Sci. 335 (2000).
- [5] J. R. Watling, L. Yang, M. Boriçi, R. C. W. Wilkins, A. Asenov, J. R. Barker, and S. Roy, Solid. State. Electron. **48**, 1337 (2004).
- [6] F. A. Zwanenburg, A. S. Dzurak, A. Morello, M. Y. Simmons, L. C. L. Hollenberg, G. Klimeck, S. Rogge, S. N. Coppersmith, and M. A. Eriksson, Rev. Mod. Phys. **85**, 961 (2013).
- [7] D. E. Eastman, C. B. Stagarescu, G. Xu, P. M. Mooney, J. L. Jordan-Sweet, B. Lai, and Z. Cai, Phys. Rev. Lett. **88**, 156101 (2002).
- [8] P. M. Mooney, J. L. Jordan-Sweet, and S. H. Christiansen, Appl. Phys. Lett. **79**, 2363 (2001).
- [9] T. Thorbeck and N. M. Zimmerman, AIP Adv. **5**, 87107 (2015).
- [10] T. B. U. Pietsch, V. Holy, *High-Resolution X-Ray Scattering* (Springer, New York, 2004).
- [11] E. E. Fullerton and I. K. Schuller, Phys. Rev. B **45**, 9292 (1992).
- [12] U. Pietsch, V. Holy, and T. Baumbach, *High-Resolution X-Ray Scattering: From*

Thin Films to Lateral Nanostructures. (Springer, Berlin, 2004).

- [13] S. O. Hruszkewycz, M. V. Holt, M. Allain, V. Chamard, S. M. Polvino, C. E. Murray, and P. H. Fuoss, *Opt. Lett.* **40**, 3241 (2015).
- [14] A. Ying, B. Osting, I. C. Noyan, C. E. Murray, M. Holt, and J. Maser, *J. Appl. Cryst.* **43**, 587 (2010).
- [15] S. O. Hruszkewycz, M. V Holt, A. Tripathi, J. Maser, and P. H. Fuoss, *Opt. Lett.* **36**, 2227 (2011).
- [16] H. M. Quiney, a. G. Peele, Z. Cai, D. Paterson, and K. a. Nugent, *Nat. Phys.* **2**, 101 (2006).
- [17] F. Mastropietro, D. Carbone, a. Diaz, J. Eymery, a. Sentenac, T. H. Metzger, V. Chamard, and V. Favre-Nicolin, *Opt. Express* **19**, 19223 (2011).
- [18] M. a Pfeifer, G. J. Williams, I. a Vartanyants, R. Harder, and I. K. Robinson, *Nature* **442**, 63 (2006).
- [19] Y. Takahashi, A. Suzuki, S. Furutaku, K. Yamauchi, Y. Kohmura, and T. Ishikawa, *Phys. Rev. B - Condens. Matter Mater. Phys.* **87**, 121201 (2013).
- [20] S. O. Hruszkewycz, M. V. Holt, C. E. Murray, J. Bruley, J. Holt, a. Tripathi, O. G. Shpyrko, I. McNulty, M. J. Highland, and P. H. Fuoss, *Nano Lett.* **12**, 5148 (2012).
- [21] M. V. Holt, S. O. Hruszkewycz, C. E. Murray, J. R. Holt, D. M. Paskiewicz, and P. H. Fuoss, *Phys. Rev. Lett.* **112**, 165502 (2014).
- [22] A. I. Pateras, M. Allain, P. Godard, L. Largeau, G. Patriarche, A. Talneau, K. Pantzas, M. Burghammer, A. A. Minkevich, and V. Chamard, *Phys. Rev. B - Condens. Matter Mater. Phys.* **92**, 205305 (2015).
- [23] P. G. Evans, D. E. Savage, J. R. Prance, C. B. Simmons, M. G. Lagally, S. N.

- Coppersmith, M. A. Eriksson, and T. U. Schulli, *Adv. Mater.* **24**, 5217 (2012).
- [24] J. Park, Y. Ahn, J. A. Tilka, K. C. Sampson, D. E. Savage, J. R. Prance, C. B. Simmons, M. G. Lagally, S. N. Coppersmith, M. A. Eriksson, M. V. Holt, and P. G. Evans, *APL Mater.* **4**, 66102 (2016).
- [25] G. A. Chahine, M. H. Zoellner, M. I. Richard, S. Guha, C. Reich, P. Zaumseil, G. Capellini, T. Schroeder, and T. U. Schüllli, *Appl. Phys. Lett.* **106**, (2015).
- [26] M. Richard, M. H. Zoellner, G. A. Chahine, P. Zaumseil, G. Capellini, M. Ha, P. Storck, T. U. Schu, and T. Schroeder, *ACS Appl. Mater. Interfaces* **7**, 26696–26700 (2015).
- [27] G. A. Chahine, M. I. Richard, R. A. Homs-Regajo, T. N. Tran-Caliste, D. Carbone, V. L. R. Jaques, R. Grifone, P. Boesecke, J. Katzer, I. Costina, H. Djazouli, T. Schroeder, and T. U. Schüllli, *J. Appl. Cryst.* **47**, 762 (2014).
- [28] M. H. Zoellner, M. I. Richard, G. A. Chahine, P. Zaumseil, C. Reich, G. Capellini, F. Montalenti, A. Marzegalli, Y. H. Xie, T. U. Schüllli, M. Haberlen, P. Storck, and T. Schroeder, *ACS Appl. Mater. Interfaces* **7**, 9031 (2015).
- [29] L. A. B. Marcal, M. I. Richard, R. Magalhaes-Paniago, F. Cavallo, M. G. Lagally, O. G. Schmidt, T. U. Schulli, C. Deneke, and A. Malachias, *Appl. Phys. Lett.* **106**, 151905 (2015).
- [30] P. G. Evans, D. S. Tinberg, M. M. Roberts, M. G. Lagally, Y. Xiao, B. Lai, and Z. Cai, *Appl. Phys. Lett.* **87**, 44 (2005).
- [31] D. M. Paskiewicz, S. A. Scott, D. E. Savage, G. K. Celler, and M. G. Lagally, *ACS Nano* **5**, 5532 (2011).
- [32] V. Mondiali, M. Bollani, S. Cecchi, M. I. Richard, T. Schüllli, G. Chahine, and D.

- Chrastina, *Appl. Phys. Lett.* **104**, 21918 (2014).
- [33] M. Holt and S. Vogt, (2006).
- [34] P. W. Deelman, L. F. Edge, and C. A. Jackson, *MRS Bull.* **41**, 224 (2016).
- [35] S. Goswami, K. a. Slinker, M. Friesen, L. M. McGuire, J. L. Truitt, C. Tahan, L. J. Klein, J. O. Chu, P. M. Mooney, D. W. van der Weide, R. Joynt, S. N. Coppersmith, and M. a. Eriksson, *Nat. Phys.* **3**, 41 (2006).
- [36] M. Friesen, M. A. Eriksson, and S. N. Coppersmith, *Appl. Phys. Lett.* **89**, 202106 (2006).
- [37] J. J. L. Morton, D. R. McCamey, M. a. Eriksson, and S. a. Lyon, *Nature* **479**, 345 (2011).
- [38] J. Y. Jo, P. Chen, R. J. Sichel, S. H. Baek, R. T. Smith, N. Balke, S. V. Kalinin, M. V. Holt, J. Maser, K. Evans-Lutterodt, C. B. Eom, and P. G. Evans, *Nano Lett.* **11**, 3080 (2011).
- [39] P. Zubko, N. Jecklin, A. Torres-Pardo, P. Aguado-Puente, A. Gloter, C. Lichtensteiger, J. Junquera, O. Stephan, and J. M. Triscone, *Nano Lett.* **12**, 2846 (2012).
- [40] A. K. Yadav, C. T. Nelson, S. L. Hsu, Z. Hong, J. D. Clarkson, C. M. Schlepüetz, A. R. Damodaran, P. Shafer, E. Arenholz, L. R. Dedon, D. Chen, A. Vishwanath, A. M. Minor, L. Q. Chen, J. F. Scott, L. W. Martin, and R. Ramesh, *Nature* **530**, 198 (2016).

3 Fabrication and Characterization of Strontium Titanate Sheets

*Portions of this chapter were published in *APL Materials* **4**, 126108 (2016)

3.1 Introduction

The creation of thin mechanically compliant complex oxide single crystals has the potential to enable new scientific and technological directions by allowing strain to be used in new ways to control functional properties ranging from electron transport to magnetism [1]. In existing demonstrations of this effect in covalent semiconductors, such as Si, the elastic compliance of nanoscale sheets can be used to create heterostructures. These heterostructures enable new strategies for the realization of quantum devices without defects resulting from plastic relaxation [2,3]. A persistent challenge in advancing towards thin materials in perovskite complex oxides, however, is that lithographic processing of thin substrates can lead to low structural quality in terms of non-uniform thickness, roughness, buckling, or defect density [4–6]. Alternative approaches based on chemical exfoliation of large-unit-cell oxide compounds can create ultrathin substrates, but have a severely limited range of compositions and crystallographic orientations [7].

This chapter addresses the creation and characterization of submicron-thick SrTiO₃ (STO) sheets, which elucidate a processing-structure relationship in complex oxide systems and produce sheets with sufficiently low defect densities for subsequent use as substrates for thin film growth. The submicron thickness scale of these sheets is particularly important. It enables elastic strain sharing over a critical range of imposed strains, 0.1 to 1%, for which elastic distortions result in significant changes in the

properties of complex oxides. Synchrotron x-ray nanodiffraction shows that the processing of these sheets does not introduce extended structural defects or large variations in lattice parameter, and that the resulting materials have sufficient structural quality to serve as substrates for epitaxial growth.

Previous methods for the creation of thin oxide crystals have important limitations. Exfoliated sheets with thicknesses of a single unit cell can be fabricated using a colloidal suspension of perovskite sheets from a Dion-Jacobson phase [7]. Exfoliation, however, yields a narrow range of thicknesses, on the order of 1-2 nm, has fixed (001) orientation set by the layering of the parent phase, and relatively small micron-scale crystals. A second method, epitaxial growth and lift-off, involves etching a sacrificial layer and transfer to a new substrate [8,9]. Lift-off requires a specific combination of etchant chemistries and sacrificial layers and has so far been developed for only a few layer compositions and orientations.

Lithographic methods for the creation of nanostructures have employed physical patterning methods, including focused ion beam (FIB) lithography and reactive ion etching [10]. The removal of material during patterning is accompanied by the creation of structural defects ranging from vacancies to extended defects [11]. Ion collisions lead to the removal of the milled material through a process that is not strongly dependent on oxide composition [11]. Ion-induced damage is a significant concern, however, in the use of FIB to create oxide nanostructures. The generation of defects during FIB is described using a collision cascade model, in which ions participate in a series of independent two-body collisions [12]. The ion-lattice collisions can displace atoms from lattice sites, creating vacancies and interstitials, which can coalesce to form dislocation [6,13]. The

resulting microstructure is described using a mosaic model and yields increased angular width of x-ray reflections [14]. In addition, vacancies in STO result in a well-known lattice expansion [15]. At high ion doses there are sufficient atomic displacements to produce a transformation to an amorphous structure, either directly beneath, or adjacent to, the location of the ion beam. The transverse straggle of ions creates such an amorphous region with a depth of tens of nanometers and changes the chemistry and functional properties of material outside the region being milled [13,16,17].

The key impact of this chapter is the lithographic fabrication of complex oxides into structures relevant for elastic strain sharing. The advantages of using lithographic patterning include the variable range of possible thicknesses and orientations, as well as not requiring a transfer process. Other commonly used methods based on exfoliated sheets or epitaxial lift-off can have the problem of fixed thickness and orientation or the need for a rigid host substrate. An important challenge of the lithographic technique presented in this chapter, FIB, is the introduction of defects into the final structure. The milling and annealing procedure here was chosen in such a way to minimize the incorporation of defects. Further development of the simulation and analysis of x-ray diffraction patterns produced with a focused beam was needed to accurately measure the rocking curve widths of the lithographically fabricated structures. The rocking curve analysis showed that the final structures had similar rocking curve width to those of bulk substrates used for complex oxide growth.

3.2 Focused Ion Beam Milling of SrTiO₃

Structural features introduced during milling, including mosaic blocks, strain, point defects, and curvature, result in an increase in the angular width of x-ray rocking curves [18,19]. The intensity and width of the (002) Bragg reflection in Ga-ion-milled

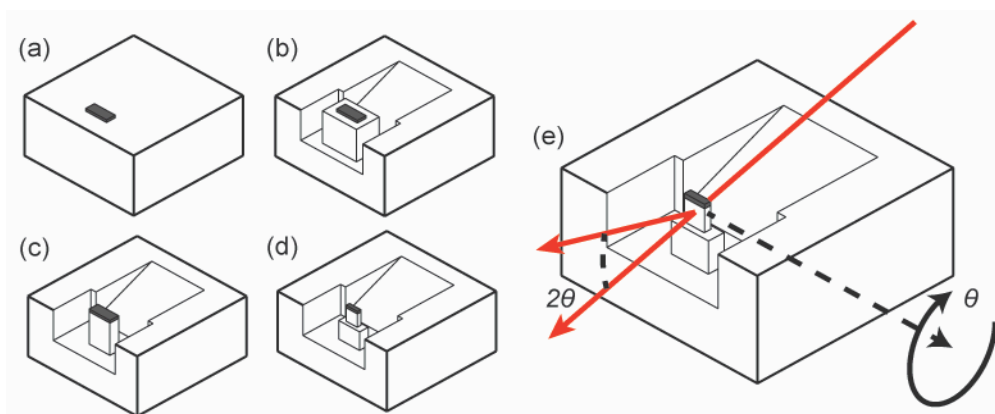


Figure 3.1 Schematic of the FIB procedure and x-ray geometry of the STO sheets. (a) Deposition of a protective C cap. (b) Coarse milling and trench creation at 14 nA. (c) Intermediate milling at 4 nA. (d) Fine milling at 300 pA. (e) X-ray scattering geometry.

BiFeO₃ thin films, for example, are reduced and broadened as a result of the electric fields of surface charges and defects [19]. Bragg reflections of STO thin films can be broadened by misfit dislocations resulting from epitaxial growth and a similar effect can be expected from ion milling [18].

The substrates for this study were (001)-oriented STO single crystals (Crystec, Inc.). Ion milling was performed with a Ga⁺ ion beam at an ion kinetic energy of 30 keV. A protective amorphous C layer with a thickness of 1 μm was deposited before milling using ion-beam-activated local chemical vapor deposition to protect a 1 μm × 14 μm area as shown in Figure 3.1(a). The C deposition process was conducted by introducing a hydrocarbon gas precursor while a 50 pA ion beam was rastered through the deposition area. The 1 μm thickness of the protective layer is larger than the 10-100 nm stopping depth of the ions [12].

The ion milling was conducted in three steps of decreasing beam current, using a procedure based on the lift-out method of transmission electron microscopy sample preparation [11,20]. An initial coarse milling step at a relatively high current of 14 nA was used to create a trench with a depth of 10 μm surrounding the region in which the

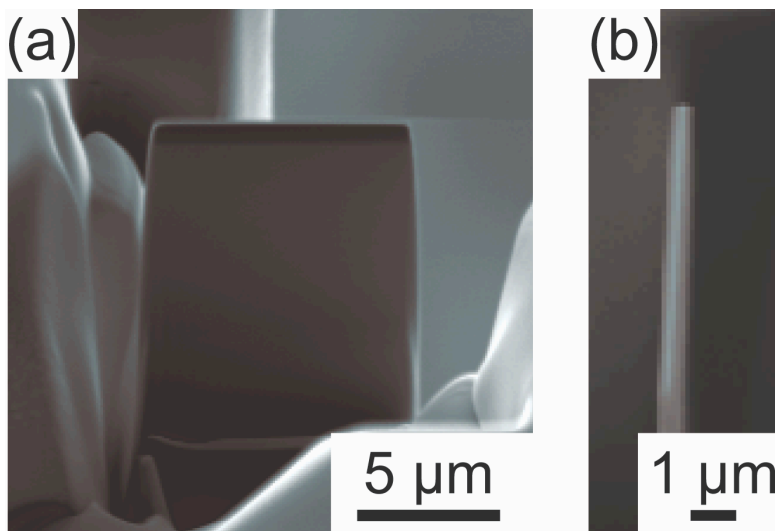


Figure 3.2 SEM image of (a) large (110) face and (b) top edge of a 500-nm-thick STO sheet produced by FIB milling. The dimensions of the face are 9.5 μm \times 10.2 μm . The darker region on the top is the protective C cap.

sheet was fabricated as shown in Figure 3.1(b). The trench was designed to allow subsequent characterization using x-ray nanodiffraction. Figure 3.1(c) shows milling at an intermediate current of 4 nA then removed STO to within approximately 500 nm of the final sheet. A low-current fine milling step was then conducted at 300 pA as shown in Figure 3.1(d). The sheet and trench allow for x-ray nanodiffraction as shown in Figure 3.1(e). Scanning electron microscopy (SEM) images of an STO sheet with a [110] surface normal and a thickness of 500 nm are shown in Figure 3.2(a) and (b).

Sheets with different thermal histories were created in order to evaluate the effects on thermal annealing in air on the STO sheets and on the near-surface regions of the bulk substrates. The annealing step was conducted at 1000 $^{\circ}\text{C}$ for 50 h, which was reached

with heating and cooling rates of 20 °C/min. Recrystallization of amorphous layers of STO created through ion bombardment and sputter deposition has been achieved by annealing at 350 °C and 1100 °C respectively [21,22]. The annealing procedure used in this study will likely recrystallize the amorphous region of the sidewall of the STO sheet caused by the transvers straggle of the Ga⁺ during milling. Samples were sputter-coated with a 100 nm carbon layer to reduce charging during x-ray exposure, which can lead to chemical and structural degradation in insulators [23].

3.3 X-ray Characterization with Convergent Nanobeam

X-ray nanobeam diffraction studies were conducted using zone-plate x-ray focusing optics at station 2ID-D of the Advanced Photon Source at Argonne National Laboratory. The diffraction experiment was conducted in a transmission geometry, as shown in Figure 3.4(a), in order to avoid illuminating the STO substrate. The x-ray photon energy was $E = 10.1$ keV, selected with a double-bounce Si (111) monochromator. The zone plate had diameter $D_{zp} = 160$ μm, outermost zone width 100 nm, zone thickness 1.6 μm, and focal length $L_f = 130$ mm at 10.1 keV. The center stop and order-sorting aperture consisted of a 60 μm-thick Au cylinder with a 40 μm diameter and a 20 μm-diameter hole in a Pt disk, respectively. The x-ray focal spot has a large angular convergence, $D_{zp}/L_f = 0.07^\circ$, leading to complex diffraction patterns. The focused beam had a full-width-at-half-maximum (FWHM) diameter of approximately 200 nm at the sample. Diffracted x-rays were detected with a charge-coupled device with 80 μm pixels (Mar 165, Mar Inc.).

Figure 3.3 shows an SEM image of the sheets (a) with a plot of the transmitted beam intensity (b). The color scale represents the intensity of the beam where yellow is

more intense. The bright regions in the graphs indicate the location of the milled trench in the sample, where it appears as a region of larger transmitted intensity in the Figure 3.3(b). The absorptions length in STO at this beam energy is $67\ \mu\text{m}$, so the 500 nm-thick

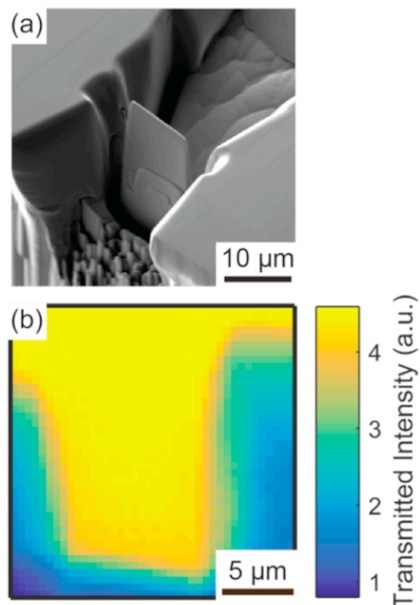


Figure 3.3 (a) SEM image of the milled sheet recessed into bulk STO. (b) Plot of transmitted x-ray intensity versus position. The bright region shows the trench milled into the substrate; the sheet cannot be resolved because the 500 nm thickness does not strongly absorb.

sheet can be expected to absorb only 0.74% of the incident intensity. The sheet appears as a weakly absorbing feature, absorbing 3.2% of the incident beam, in Figure 3.3(b). An SEM image in Figure 3.3(a) shows the same region of the sample, and the experimental diffraction geometry is shown in Figure 3.4(a). Unfortunately, the focused beam from the zone plate does not have excellent contrast. The majority of the x-ray intensity is within the FWHM of the beam, however, much of the intensity is in concentric rings centered at the beam focus. This intensity is broadly distributed about the beam, and could interact with the bulk sample. The experiment takes place at a Bragg reflection, which means that these weak wavefronts will interact with strong scatters at the Bragg condition. Some of

the intensity being scattered to the detector is likely from the bulk material, rather than the milled sheet.

Experimental diffraction patterns from milled and annealed (110)-oriented 500-nm-thick STO sheets are shown in Figure 3.4(b). The incident angle of the center of the

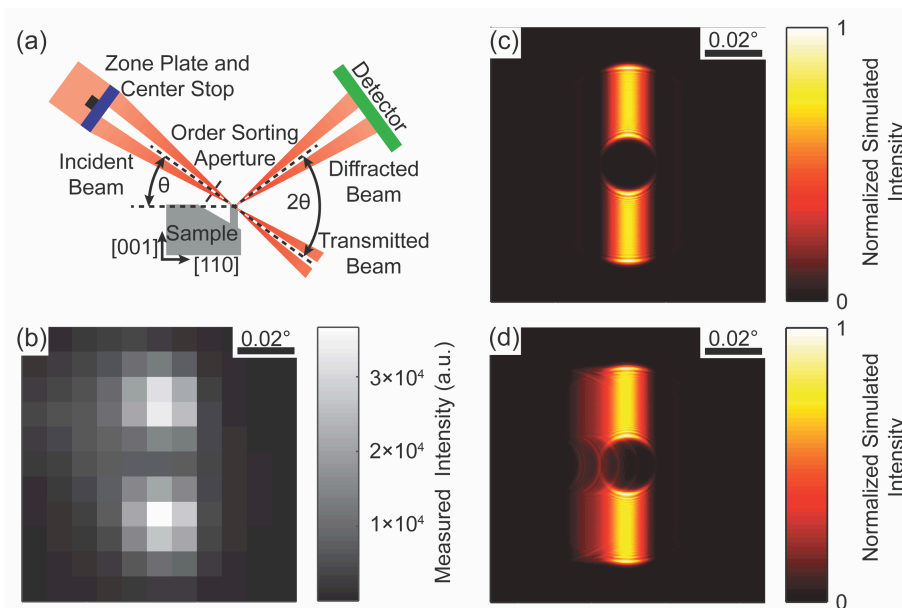


Figure 3.4 (a) Schematic of the synchrotron x-ray nanodiffraction experiment. (b) Experimental diffraction pattern of the (002) Bragg reflection of a (110) annealed STO sheet. (c) A simulated (002) diffraction pattern using the same focusing optics as in the experiment and an ideal 500 nm thick STO sample. (d) Five incoherently summed mosaic blocks of STO with orientations differing in θ over a range of 0.013° . The off center blocks each have one eighth the intensity of the block in the center of the image.

focused beam for Figure 3.4(b) was $\theta = 18.322^\circ$, which corresponds to the STO (002) Bragg reflection. X-ray rocking curves were acquired by scanning the x-ray incident angle, θ , through a total range of 0.1° . Interpreting rocking curves acquired with a nanobeam is challenging because the incoming x-ray beam is not defined by a single wavevector, but a range of wavevectors corresponding to the angular divergence of the focused x-ray beam.

The diffraction experiment was simulated using wave-optics methods that faithfully reproduce the angular and spatial beam distribution at the focal spot, followed

by a simulation of kinematic diffraction by the sample, and propagation to the detector [24,25]. A simulated diffraction pattern with focusing optics and sample orientation matching the experiment is shown in Figure 3.4(c). The region of high intensity in Figure 3.4(c) vertically spans the angle subtended by the zone plate and has a horizontal width inversely proportional to the height of the illuminated region of the sample. The dark circle at the center of the simulated diffraction pattern in Figure 3.4(c) corresponds to the projection of the shadow of the center stop onto the x-ray detector.

An additional complication arises because mosaic blocks with orientations differing from the nominal Bragg condition by an angle less than half of the beam divergence also satisfy the Bragg condition for some part of the convergent incident beam. A defective sample was considered by simulating multiple crystals with angular offsets. The scattering from each mosaic block was summed incoherently to simulate diffraction patterns from mosaic crystals.

Figure 3.4(d) shows a simulated diffraction pattern of a distribution of five mosaic blocks with identical lattice parameters misoriented equally over 0.013° in θ . The relative intensity and mutual orientation of the misoriented blocks were chosen in order to match the experimental result in Figure 3.4(b). Note that the difference in the orientation of the blocks allows them to be distinguished in the diffraction pattern.

3.4 Discussion of Mosaic Distribution and Lattice Expansion

Diffraction patterns for an experimental rocking curve of an unprocessed STO crystal are shown in Figure 3.5(a). Figure 3.5(a) shows diffraction patterns of the (002) Bragg reflection acquired at different sample orientations. Figure 3.5(a) exhibits a vertical region of high diffracted intensity that moves across the detector. The shadow of

the center stop appears at the center of the image at $\theta = 18.322^\circ$. The diffraction pattern has high intensity at all angles within a range equal to the angular divergence of the incident focused x-ray nanobeam.

The mosaic distribution within a conventional rocking curve scan is evaluated by measuring the angular width of the integrated diffracted x-ray intensity as a function of

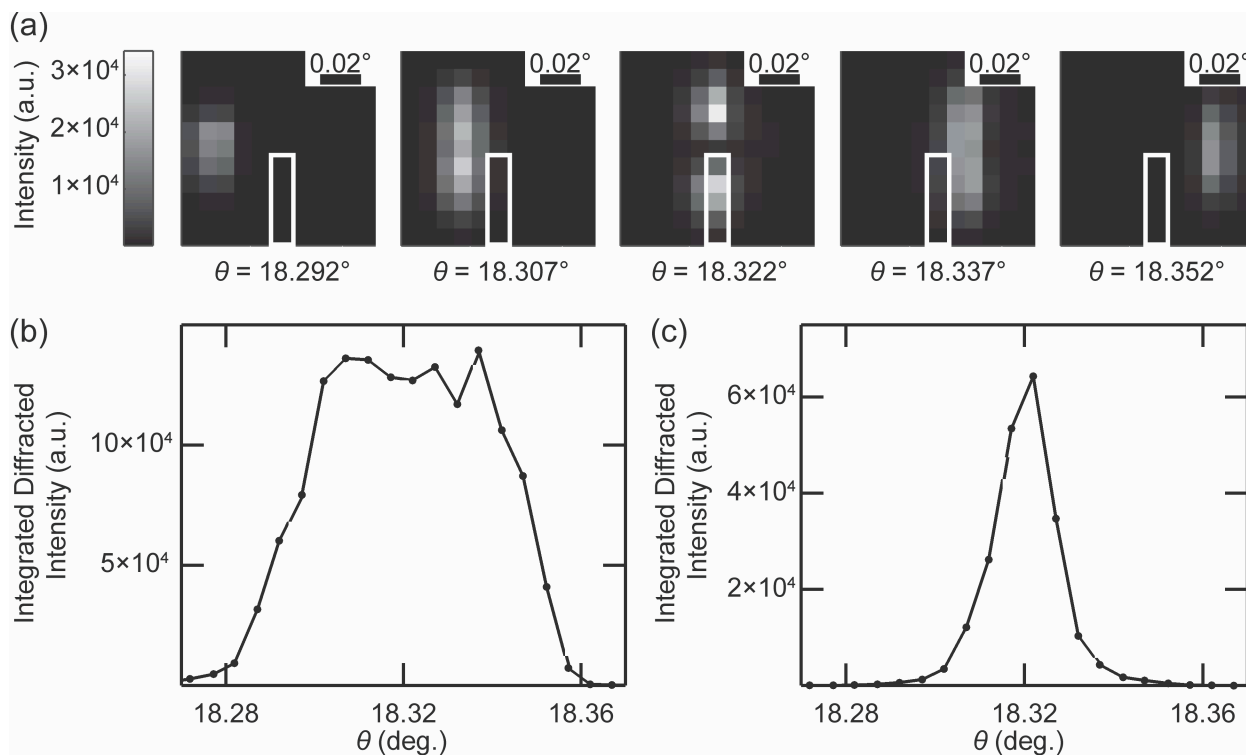


Figure 3.5 (a) Diffraction patterns of the (002) Bragg reflection from bulk unprocessed STO acquired with different sample orientations ranging from $\theta = 18.292^\circ$ to $\theta = 18.352^\circ$. The region of high x-ray intensity moves from left to right as θ increases. The shadow of the center stop is apparent at $\theta = 18.322^\circ$. (b) Integrated intensity as a function of angle for the diffraction patterns shown in (a). The intensity of the rocking curve is approximately constant over an angular range equal to the zone plate divergence because part of the divergent beam meets the Bragg condition for all angles in this range. (c) Narrow rocking curves produced by integrating within the region of interest indicated by the white box in (a).

the sample orientation [26]. With the convergent focused x-ray nanobeam, however, the angular width of the total intensity is set by the beam divergence rather than by the mosaic width. Figure 3.5(b) shows the integrated intensity as a function of the sample

orientation, exhibiting a full-width-at-tenth-maximum of 0.073° , matching the angular width of the incident beam, 0.070° .

Examining the dependence of the intensity within small areas of the diffraction patterns as a function of sample orientation allows far more precise study of the mosaicity of the sample than the total integrated intensity. The intensity integrated in a smaller

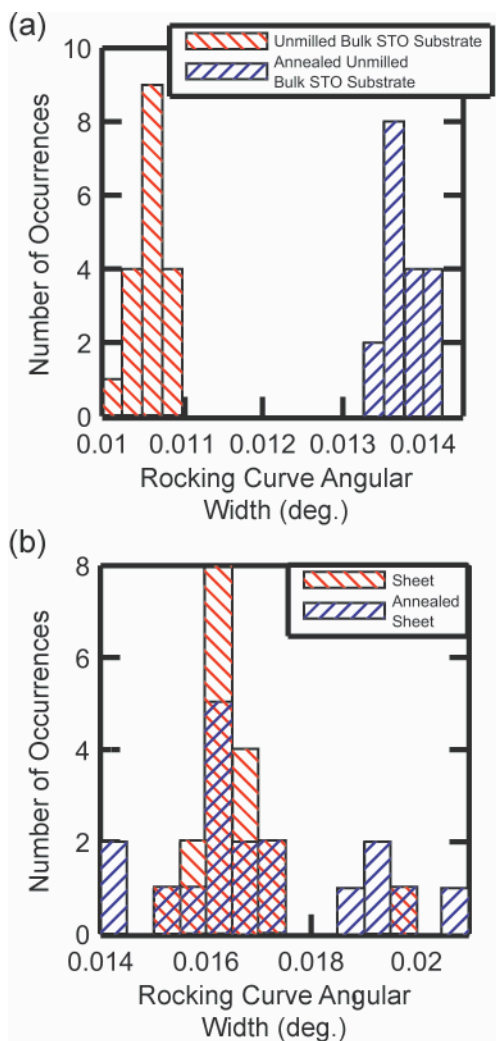


Figure 3.6 (a) Histograms of rocking curve widths of bulk STO before and after annealing. (b) Histograms of rocking curve widths of STO sheets. The most frequent width in both cases is 0.016° .

region of the detector, as shown in Figure 3.5(c), exhibits features much narrower than the angular width of the total integrated intensity. When a narrow range of the detector is

integrated, the x-ray rocking curve has an angular width set by the angular width of the detector pixel, in this case 0.01° , rather than by the entire focused beam. Other sources of broadening such as the finite energy bandwidth of the experiment have been neglected. The intensity peak in Figure 3.5(c) has a FWHM of 0.011° , matching this expectation.

X-ray rocking curve measurements were used to examine the degree of homogeneity in the STO sheets and to evaluate the structural effect of each processing step. Structural studies using the method shown in Figure 3.5(c) were repeated at multiple locations for milled and unmilled STO sheets, and annealed STO substrates. Histograms of the angular widths of the diffracted intensity are shown in Figure 3.6(a). The angular widths increase from 0.010° to 0.014° upon annealing. A possible origin of the increased mosaic width after annealing is a change in the oxygen vacancy concentration in the surface region of STO due the difference between the annealing conditions and the bulk STO growth conditions. At this energy and incident angle the x-ray beam will probe $10\ \mu\text{m}$ into the bulk STO, and variation in the lattice parameter over that thickness will impose a strain gradient that increases the rocking curve width.

The FIB patterning and annealing processes lead to slight increases in the rocking curve angular width in comparison with bulk STO. Figure 3.6(b) shows a histogram of the narrow-region rocking curve widths taken from a series of locations across the (110)-oriented STO sheets with a thickness of 500 nm. The x-ray rocking curves were acquired from regions of the samples that were separated by distances of 200 nm. The most frequently observed width in both annealed and unannealed sheets is 0.016° . The process of patterning the STO sheets thus resulted in an increase of rocking curve width from 0.01° to 0.016° .

There are several possible origins of the slight increase in width arising from the patterning and annealing of the STO samples. It is possible that that the increase results from the introduction of dislocations into the STO sheet during the patterning as shown in

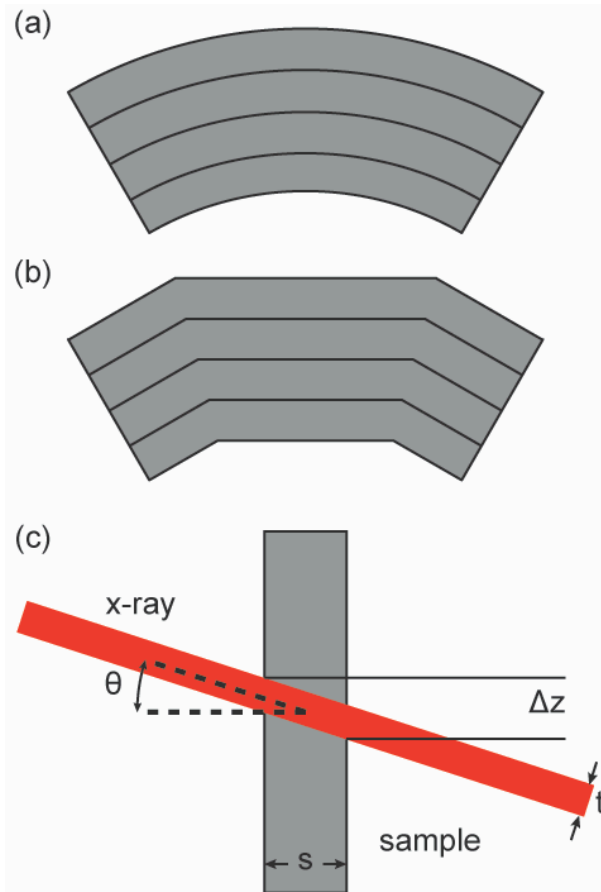


Figure 3.7 (a) STO plans that have been elastically or plastically bent to cause a curvature in the STO sheet. (b) STO planes with low angle gran boundaries (c) schematic of the height of STO sheet illuminated by the nanofocused x-ray beam.

Figure 3.7(a) and (b). An upper limit of the dislocation density in the sheet can be determined by assuming that each dislocation creates a mosaic block. The dislocation density required to produce the observed width can be found using $D_{dis} = (\Delta\beta)^2/9b^2$, where D_{dis} is the dislocation density, $\Delta\beta$ is the rocking curve width, and b is the Burgers vector [18]. If the dislocations were ordering into a low energy structure then features like low angle grain boundaries could form as shown in Figure 3.7(b). The most common

Burgers vector observed in transmission electron microscopy studies of STO is $\frac{1}{2}\langle 110 \rangle$ [27]. The dislocation density corresponding to an angular width of 0.016° wide rocking curve in STO is thus 10^7 cm^{-2} . This density is sufficiently small that we cannot expect even one dislocation within the area defined by the beam width and the sample thickness. This density of dislocations is thus sufficiently low that we cannot attribute the small increase in mosaic width to the introduction of dislocations in the sheet during milling and annealing.

A second possibility is that the angular width of the STO reflections arises from the overall curvature of the 500-nm-thick STO sheet. The curvature was separately measured by examining the systematic shift in the Bragg angle as a function of the position of the x-ray beam as it was scanned along the height of a single milled and unannealed sheet through points spaced 200 nm apart. The radius of curvature measured in this way was $R = 7 \text{ mm}$. The effective difference in orientation across the illuminated region of the sheet, as shown in Figure 3.7(c), is $\Delta z/R$, where Δz is illuminated height given by $\Delta z = s \tan(\theta) + t / \cos(\theta)$ and t and s are the focal spot size and sheet thickness, respectively, as shown schematically in Figure 3.7 (c). The expected angular width due to the curvature of the sheet is thus 0.003° , which is only a factor of four less than the difference in quadrature between the angular width of the bulk unprocessed STO and the unannealed STO sheets.

The creation of point defects such as oxygen vacancies can be studied by evaluating the change in the average lattice parameter of the sheets. The lattice expansion, Figure 3.8, was calculated using the 2θ angle (defined as in Figure 3.4(a)) with the peak intensity in the rocking curve scans. The lattice expansion after milling was

0.06%, referred to the bulk STO lattice parameter. The subsequent annealing step reduces the expansion to 0.03%. An oxygen vacancy concentration of approximately 0.09% with respect to the number of oxygen lattice sites would result in the observed lattice

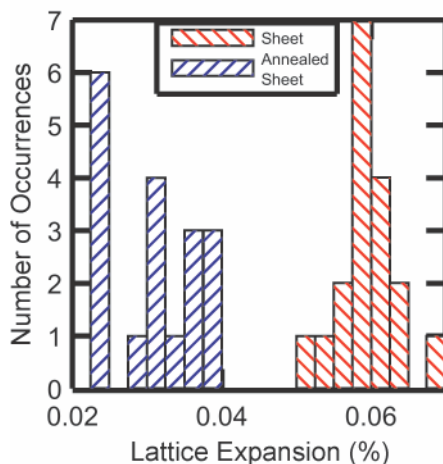


Figure 3.8 Histograms of the lattice expansion in the STO sheets acquired in the same locations as Figure 3.6(b).

parameter [15]. We thus conclude that the oxygen vacancy concentration is less than 0.1% after the FIB process. A gradient of lattice parameters resulting from an inhomogeneous distribution of vacancies would alter the rocking curve widths. The change in x-ray rocking curve width in the bulk STO due to annealing could be a result of a change in lattice parameter over the depth probed by the x-ray beam. Although x-ray photoelectron spectroscopy (XPS) would normally be an excellent tool for determining oxygen vacancy concentrations, the concentrations in this work would be too low to detect with these techniques. For example, the detection limit of oxygen vacancy concentration with XPS in BaTiO_3 is approximately 1% [28]. These values are an order of magnitude above the expected oxygen vacancy concentration from the observed lattice expansion. I hypothesize that the process of annealing in air reduces the concentration of oxygen vacancies and thus accounts for the reduction in lattice expansion after annealing.

3.5 Conclusion

This chapter demonstrates that focused ion beam methods can be used to create oxide crystals that are likely thin enough to be elastically compliant with arbitrary orientation and low defect density. The knowledge gained about the effects of a lithographic patterning technique on structural quality of perovskite materials provides valuable insight for future research on strain engineering in complex oxide systems. X-ray nanodiffraction using tightly focused beams indicates that the increase in the rocking curve width is at most a factor of two, small enough that mosaic widths fall within a range typically used for epitaxial growth [29].

3.6 References

- [1] D. G. Schlom, L.-Q. Chen, C. J. Fennie, V. Gopalan, D. A. Muller, X. Pan, R. Ramesh, and R. Uecker, *MRS Bull.* **39**, 118 (2014).
- [2] M. M. Roberts, L. J. Klein, D. E. Savage, K. A. Slinker, M. Friesen, G. Celler, M. A. Eriksson, and M. G. Lagally, *Nat. Mater.* **5**, 388 (2006).
- [3] P. M. Mooney, G. M. Cohen, J. O. Chu, and C. E. Murray, *Appl. Phys. Lett.* **84**, 1093 (2004).
- [4] D. M. Paskiewicz, D. E. Savage, M. V Holt, P. G. Evans, and M. G. Lagally, *Sci. Rep.* **4**, 4218 (2014).
- [5] G. Gopalakrishnan, D. A. Czaplewski, K. M. McElhinny, M. V. Holt, J. C. Silva-Martínez, and P. G. Evans, *Appl. Phys. Lett.* **102**, (2013).
- [6] C. R. Hutchinson, R. E. Hackenberg, and G. J. Shiflet, *Ultramicroscopy* **94**, 37 (2003).
- [7] B. W. Li, M. Osada, T. C. Ozawa, Y. Ebina, K. Akatsuka, R. Ma, H. Funakubo, and T. Sasaki, *ACS Nano* **4**, 6673 (2010).
- [8] D. Paskiewicz, R. Sichel-Tissot, E. Karapetrova, L. Stan, and D. D. Fong, *Nano Lett.* **16**, 534 (2016).
- [9] D. Lu, D. J. Baek, S. S. Hong, L. F. Kourkoutis, Y. Hikita, and H. Y. Hwang, *Nat. Mater.* **15**, 1255 (2016).
- [10] R. Maaß, D. Grolimund, S. Van Petegem, M. Willimann, M. Jensen, H. Van Swygenhoven, T. Lehnert, M. A. M. Gijs, C. A. Volkert, E. T. Lilleodden, and R. Schwaiger, *Appl. Phys. Lett.* **89**, 111 (2006).
- [11] J. Mayer, L. A. Giannuzzi, T. Kamino, and J. Michael, *MRS Bull.* **32**, 400 (2007).

- [12] C. A. Volkert and A. M. Minor, *MRS Bull.* **32**, 389 (2007).
- [13] S. Rubanov and P. R. Munroe, *J. Microsc.* **214**, 213 (2004).
- [14] P. Gay, P. B. Hirsch, and A. Kelly, *Acta Metall.* **1**, 315 (1953).
- [15] H. L. Cai, X. S. Wu, and J. Gao, *Chem. Phys. Lett.* **467**, 313 (2009).
- [16] D. Kiener, C. Motz, M. Rester, M. Jenko, and G. Dehm, *Mater. Sci. Eng. A* **459**, 262 (2007).
- [17] A. Stanishevsky, B. Nagaraj, J. Melngailis, R. Ramesh, L. Khriachtchev, and E. McDaniel, *J. Appl. Phys.* **92**, 3275 (2002).
- [18] Z. Y. Zhai, X. S. Wu, H. L. Cai, X. M. Lu, J. H. Hao, J. Gao, W. S. Tan, Q. J. Jia, H. H. Wang, and Y. Z. Wang, *J. Phys. D: Appl. Phys.* **42**, 105307 (2009).
- [19] W. Siemons, C. Beekman, J. D. Fowlkes, N. Balke, J. Z. Tischler, R. Xu, W. Liu, C. M. Gonzales, J. D. Budai, and H. M. Christen, *APL Mater.* **2**, 22109 (2014).
- [20] T. Yaguchi, T. Kamino, T. Ishitani, and R. Urao, *Microsc. Microanal.* **5**, 365 (1999).
- [21] C. W. White, L. A. Boatner, P. S. Sklad, C. J. McHargue, J. Rankin, G. C. Farlow, and M. J. Aziz, *Nucl. Instruments Methods Phys. Res. B* **32**, 11 (1988).
- [22] F. Wang, M. Badaye, Y. Yoshida, and T. Morishita, *Nucl. Instruments Methods Phys. Res. B* **118**, 547 (1996).
- [23] L. Gregoratti, T. O. Montes, A. Locatelli, and M. Kiskinova, *J. Electron Spectros. Relat. Phenomena* **170**, 13 (2009).
- [24] A. Ying, B. Osting, I. C. Noyan, C. E. Murray, M. Holt, and J. Maser, *J. Appl. Cryst.* **43**, 587 (2010).
- [25] J. A. Tilka, J. Park, Y. Ahn, A. Pateras, K. C. Sampson, D. E. Savage, J. R. Prance,

- C. B. Simmons, S. N. Coppersmith, M. A. Eriksson, M. G. Lagally, M. V. Holt, and P. G. Evans, *J. Appl. Phys.* **120**, 15304 (2016).
- [26] T. B. U. Pietsch, V. Holy, *High-Resolution X-Ray Scattering* (Springer, New York, 2004).
- [27] J. Yamanaka, *Mater. Trans.* **42**, 1131 (2001).
- [28] J. L. Wang, J. Leroy, G. Niu, G. Saint-Girons, B. Gautier, B. Vilquin, and N. Barrett, *Chem. Phys. Lett.* **592**, 206 (2014).
- [29] M. D. Biegalski, D. D. Fong, J. A. Eastman, P. H. Fuoss, S. K. Streiffer, T. Heeg, J. Schubert, W. Tian, C. T. Nelson, X. Q. Pan, M. E. Hawley, M. Bernhagen, P. Reiche, R. Uecker, S. Trolrier-Mckinstry, and D. G. Schlom, *J. Appl. Phys.* **104**, 114109 (2008).

4 Stressor-Layer-Induced Elastic Strain Engineering in SrTiO₃ Complex Oxide Sheets

4.1 Introduction

The deliberate introduction of elastic strain with magnitudes on the order of 0.01% to 1% is a powerful way to control the functional properties of complex oxides. Elastic strain in nanoscale materials can raise or lower the mobility of charge carriers and ions, change the magnitude or symmetry of the electronic band gap, shift the Curie temperatures of magnetic and ferroelectric phase transitions, or modify ferroelectric nanodomain configurations through energy-competition mechanisms [1–6]. Physical phenomena arising from elastic strain are often studied and controlled in complex oxides by employing the large stresses arising from coherent heteroepitaxy, during which the in-plane lattice parameter of the thin film is constrained to match the lattice parameter of the substrate [7]. The use of this epitaxial lattice mismatch to create elastic strain is, however, limited to a finite number of discrete values by the compositions of available substrates. For example, a BaTiO₃ (BTO) thin film coherently grown on SrTiO₃ (STO) has a fixed in-plane elastic strain of -2% [8]. Other values of the elastic mismatch strain can only be achieved by changing the composition, and hence lattice parameter, of the substrate [9]. It has not been possible in general to choose arbitrary values of the elastic strain because the range of compositions and lattice parameters of suitable single-crystal substrates is limited. In addition, a systematic exploration of strain effects can require the development of different surface preparation and epitaxial growth procedures for each substrate composition. This chapter describes an experimental test of a single example of an

alternative approach in which a thin complex oxide sheet is strained by a stressor layer. The magnitude of the elastic strain is set by the stress in the stressor, allowing the lattice parameter to be precisely selected. This approach, demonstrated here, can be used to introduce strain in an STO sheet distorted by a calibrated silicon nitride layer without the formation of structural defects.

Elastic strain in complex oxides can be particularly important in ferroelectric and ferromagnetic materials. In ferroelectrics, for example, the elastic strain, ϵ , in BTO grown on an elastically compliant STO sheet could in principle be set in a range between -2% and 0 by selecting the thicknesses of the BTO layer or the STO sheet. Here the strain is defined as $\epsilon = (a_{\text{BTO, film}} - a_{\text{BTO}}) / a_{\text{BTO}}$ in terms of the unstressed and thin-film in-plane lattice parameters a_{BTO} and $a_{\text{BTO, film}}$. Varying the strain over this range would change the ferroelectric Curie temperature of BTO by more than 100 °C [2]. Similarly, in the heteroepitaxial growth of the magnetic complex oxide $\text{La}_{0.7}\text{Sr}_{0.3}\text{MnO}_3$ on STO imposes an strain on the order of 1% and relaxation near grain boundaries leads to regions of increased Curie temperature [10].

Elastic strain sharing in oxides can employ processing techniques that have been developed for semiconductors, but which have not yet been explored in a wider range of materials. Elastic strain has been exploited in several contexts in semiconducting materials. For example, the introduction of strain on the order of 1% has enabled dramatic improvements in the performance of Si field-effect transistors [11]. Strain in InGaAs heterostructures on compliant substrates shifts the wavelength of infrared semiconductor lasers [12]. The optical properties of Ge depend sensitively on elastic strain, which can be used to induce a change in the bandgap from indirect to

direct [13,14]. Strained-Si/relaxed SiGe heterostructures grown on compliant sheets exhibit reduced local variations in strain and crystallographic tilt in comparison with layers grown on graded SiGe directly on Si [15]. Advances in the control of strain in complex oxides promises to bring a similarly precise level of control.

A crucial challenge associated with elastic strain sharing in complex oxides has been the creation of single-crystal sheets that have the defect density, composition, and crystal structure of commonly used bulk substrate materials. The oxide sheets must be sufficiently thin to produce relevant values of elastic strain using the range of experimentally available stresses. Complex oxide sheets that are sufficiently thin for studies of elastic strain sharing have been created by chemical exfoliation, epitaxial lift-off, and lithographic techniques [16–20]. The first two methods, however, face significant experimental challenges. Chemical exfoliation often results in an ensemble of micron-scale sheets rather than a thin layer with large lateral extent [18]. Similarly, sheets created via epitaxial lift-off can involve two-dimensional mechanical constraint imposed by the rigid substrate to which they are transferred, rendering them unsuitable for elastic strain sharing [16].

The key impacts of this chapter are the creation of an elastically strained complex oxide sheet and the further development of x-ray nanobeam analysis to accurately measure the strain. The complex oxide sheet was strained through the creation of a trilayer heterostructure that applied an elastic strain. The simplicity of the trilayer structure allows me to use a quantitative model developed for semiconducting heterostructures to accurately predict the dependence of strain on sheet thickness and thin films stress thickness product. The strain predicted with this model resulted in small

changes of the x-ray diffraction pattern narrower than the width of the zone plate divergence. This chapter explores the necessary advances required to quantitatively interpret and simulate the effect small strain has on nanobeam diffraction patterns. This insight is then used to calculate the strain of small complex oxide sheets.

4.2 Fabrication and Characterization of Strain SrTiO₃ Sheets

This chapter centers on STO sheets fabricated a lithographic approach starting from a large STO single crystal. As shown in Figure 4.1(a) the structure consists of a submicron-thick STO sheet with a non-stoichiometric silicon nitride (SiN) layer deposited on each of its planar faces. The STO sheets were fabricated from an STO single crystal using focused ion beam (FIB) lithography and had a thickness $t_{STO} = 510$ nm and area of $10 \times 10 \mu\text{m}^2$. The FIB steps were conducted using a process developed to reduce the introduction of defects by reducing the milling current in a series of steps as the lithography progressed towards finer-scale features [21]. Under these conditions, FIB yields STO sheets that have the same x-ray nanobeam diffraction rocking curve widths as the bulk unprocessed STO crystal [19]. A scanning electron microscope image of an STO sheet before the deposition of the SiN layers is shown in Figure 4.1(b).

The SiN stressor layers were deposited by plasma-enhanced chemical vapor deposition (PT-70, Plasma-Therm) with a sample temperature of 250 °C. The N₂O, 2% SiH₄ in N₂, and 5% NH₃ in N₂ flow rates were 420, 500, and 80 sccm, respectively, with total pressure of 850 mTorr. The plasma was produced with a power of 36 W at 13.56 MHz and a bias of -28.6 V. The deposition yielded a 270 nm-thick SiN layer conforming to the complex geometry of the STO sheet. Figure 4.1(c) and (d) show side and perspective views of the STO sheet after the deposition of the SiN stressors.

The design of the SiN/STO/SiN structure is guided by a mechanical model based on the balance of forces applied to the sheet [22]. A schematic of the force balance is

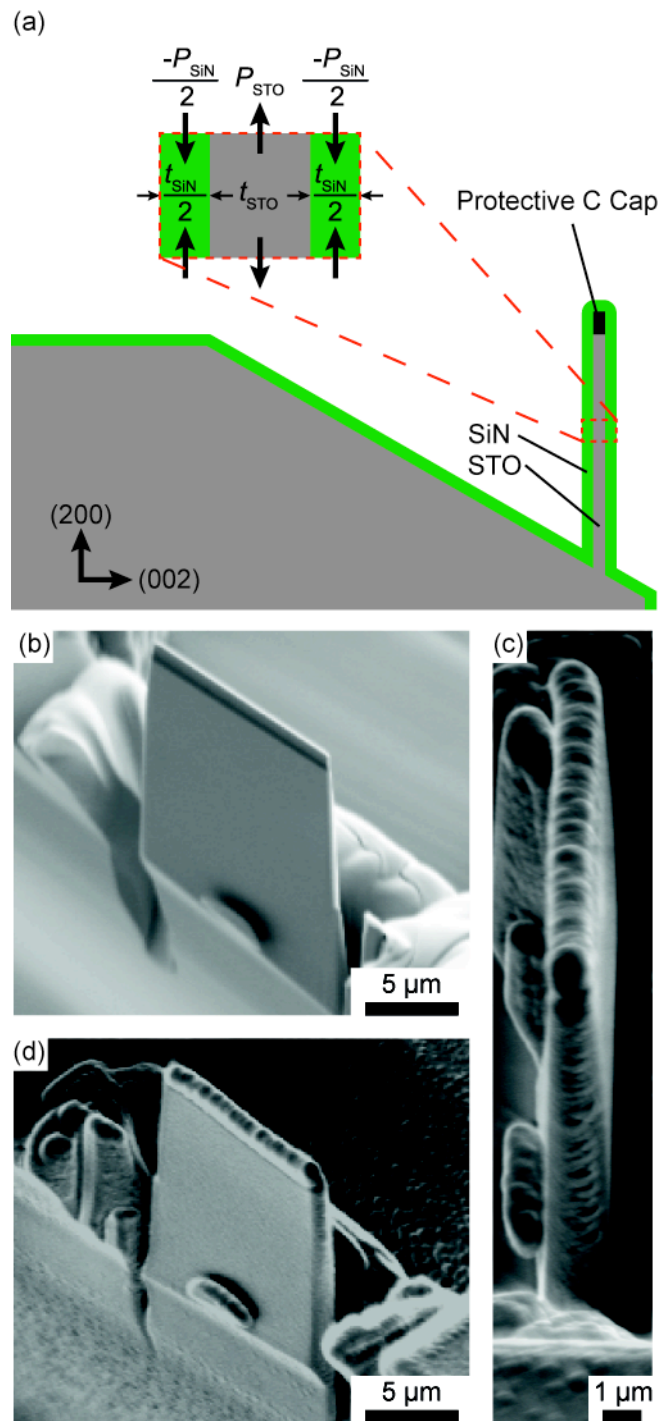


Figure 4.1(a) Schematic of the STO sheet with SiN stressor layers. Scanning electron microscopy images of a 510-nm-thick STO sheet (b) without (c-d) with a 270-nm-thick SiN layer deposited on the face. The large face of the sheet has area $10 \times 10 \mu\text{m}^2$.

shown in the inset of Figure 4.1(a). The mechanical description of the strained STO sheets was simplified by assuming that the thicknesses and stresses in both SiN layers are equal and that the STO sheet is not curved by the stress. Effects from the edges can be neglected because the sheets have a large width-to-thickness aspect ratio on the order of 20. The SiN sheets apply a biaxial tensile force per unit length of magnitude P , corresponding to a biaxial compressive stress-thickness product equal to $-P/2$ in each of the stressor layers. The individual SiN stressor layers have thickness, $t_{\text{SiN}}/2$. In Cartesian coordinates defined such that the axes x and y lie within the plane of the STO sheet with x along the direction of the bulk substrate normal, the non-zero elements of the stress tensor within the sheet are $\sigma_{11} = \sigma_{22} = \sigma_{\text{STO}}$. The stress has a magnitude $\sigma_{\text{STO}} = P/t_{\text{STO}}$. The fractional change in the interplanar spacing, d , in the in-plane [100] direction is $\varepsilon_{\text{STO}} = P/(M_{\text{STO}} t_{\text{STO}})$, where $M_{\text{STO}} = 395$ GPa is the biaxial modulus for STO (100) [22,23].

The magnitude of the stress-thickness product in the SiN stressors depends on their deposition conditions, thickness, thermal history, and stoichiometry. The stress in the SiN layers is influenced by small differences in the Si:N ratio and the incorporation of hydrogen during deposition [24–26]. The parameters P and t_{STO} can be chosen to select the strain induced in STO. The stress-thickness product applied by the two SiN layers, which is equal to P , was measured by evaluating the curvature introduced by a SiN layer deposited on one side of a Si wafer [27]. The stress-thickness product applied by the SiN film measured in this way was $P = 28$ GPa·nm, and the predicted strain in the STO sheet was 1.4×10^{-4} .

The strain introduced in the STO sheets by the SiN stressors was measured using synchrotron x-ray nanobeam diffraction. Figure 4.2(a) shows a schematic of the

nanodiffraction measurement, including the angular definitions of the incident and diffracted x-ray beams. The nanodiffraction studies were conducted at station 2-ID-D of the Advanced Photon Source at Argonne National Laboratory using a photon energy of

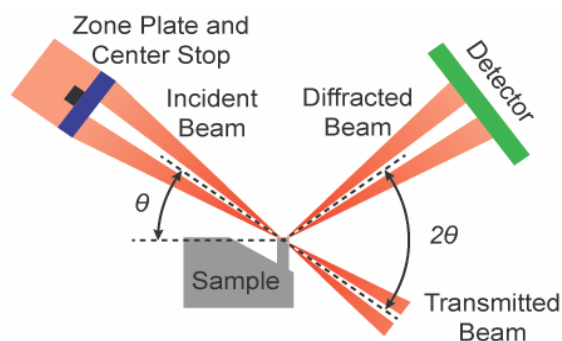


Figure 4.2 Schematic of the x-ray scattering geometry showing the definitions of the angles θ and 2θ .

10.1 keV, selected with a (111) Si monochromator. Zone-plate based focusing optics using a 160 μm diameter zone plate with a 100 nm wide outermost zone were used to create a full-width-at-half-maximum diameter of 200 nm at the focus. Diffracted x-rays were detected using an x-ray charge-coupled device (Princeton Quad-RO, Princeton Instruments) with square pixels on a grid with a 24 μm spacing, positioned 1 m from the x-ray focal spot. The focused beam had a convergence angle of 0.07° , which makes it impossible to define a unique angle for the incident and diffracted beams. Thus, the effective incident angle, θ , is defined as be the angle between the central axis of the focused x-ray beam and the (200) planes in the STO substrate. The angle 2θ refers to the angle between the center of the focused x-ray beam and the location of each detector pixel.

Figure 4.3 illustrates the complications associated with the uncertainty associated with the x-ray divergence. The experimental diffraction patterns from Chapter 3 are used

for illustrative purposes before the diffraction data from the current and more complicated heterostructures are introduced. In this example, three different incoming

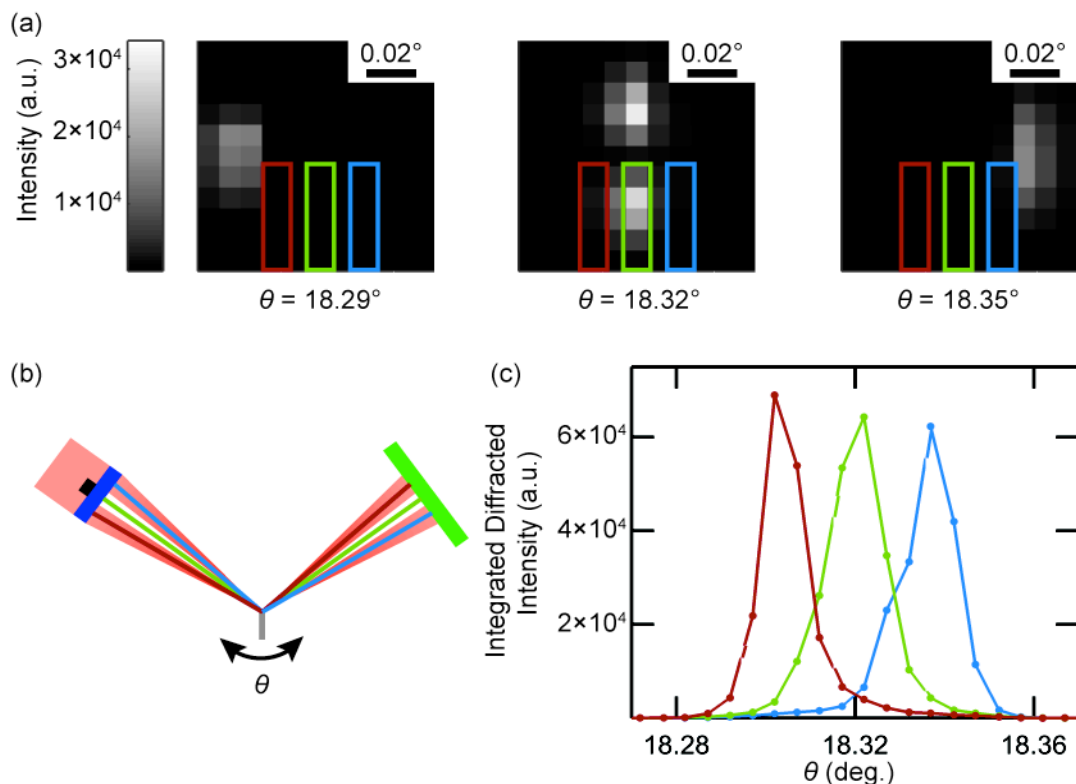


Figure 4.3 (a) Three experimental diffraction patterns taken different incident angles each with three different rectangular regions of interest with colors corresponding to the vectors and peaks in (b) and (c) respectively. (b) Schematic x-ray scattering showing different incident wavevectors within a single incident angle. (c) Three rocking curve peaks corresponding to the rectangles in (a).

wavevectors are chosen to represent the incoming x-ray beam, and the color associated with each rectangular area of interest in Figure 4.3(a) correspond to the same color in Figure 4.3(b) and (c). Three incident angles are shown in Figure 4.3(a) with three different regions of interest shown at slightly different detector locations all within the divergence of the zone plate, which correspond nominally to three different values of 2θ . The incoming and diffracted wavevectors responsible for the scattered intensity to each rectangular region of interest can be traced in Figure 4.3(b), where the three colors are all show with the sample value of 2θ and different angles of incidence. Figure 4.3(c) shows

three separate rocking curves created from the three colored rectangles in Figure 4.3(a) which all have a different value of θ for the location of the peak x-ray intensity. The depiction of three separate peaks as a function of incidence angle is most commonly associated with the presence of a mosaic microstructure. However, The features shown in Figure 4.3 originate from a single crystal and are in fact multiple representations of the same Bragg reflection observed at different locations within the divergence of the zone plate.

The tensile stress applied to the STO sheet by the SiN stressor leads to an expansion of the (200) in-plane lattice constant of the sheet, and thus to a smaller incident angle, θ . The predicted angular shift in the Bragg angle is 0.003° , much less than the 0.07° angular divergence of the focused x-ray beam. A change in either the lattice parameter or the crystallographic orientation could result in an angular shift of the expected magnitude, complicating the analysis of the diffraction experiment.

The x-ray diffraction results were compared with an x-ray optical simulation in order to distinguish the strain from effects associated with the tilt of the lattice. The simulation propagates the incident x-ray beam from the zone plate to the sample using the Fresnel approximation, computes the amplitude and phase of the diffracted beam using the kinematic approximation, and propagates the diffracted beam from the sample to the detector [28–30]. The kinematic approximation accurately reproduces the x-ray diffraction patterns of the sheets. The diffraction patterns of the bulk STO reference sample were calculated using the Darwin dynamical theory of x-ray diffraction because bulk STO is many times thicker than the x-ray extinction depth, $0.5 \mu\text{m}$, and dynamical scattering effects such as multiple scattering and primary extinction cannot be neglected.

Dynamical effects were incorporated into the simulation by assuming that the bulk STO consisted of a perfect one-dimensional array of STO unit cells with infinite thickness [30].

The bulk STO measurement was used as a reference for the orientation and spacing of the (200) planes in the STO sheet. Three diffraction patterns from an x-ray

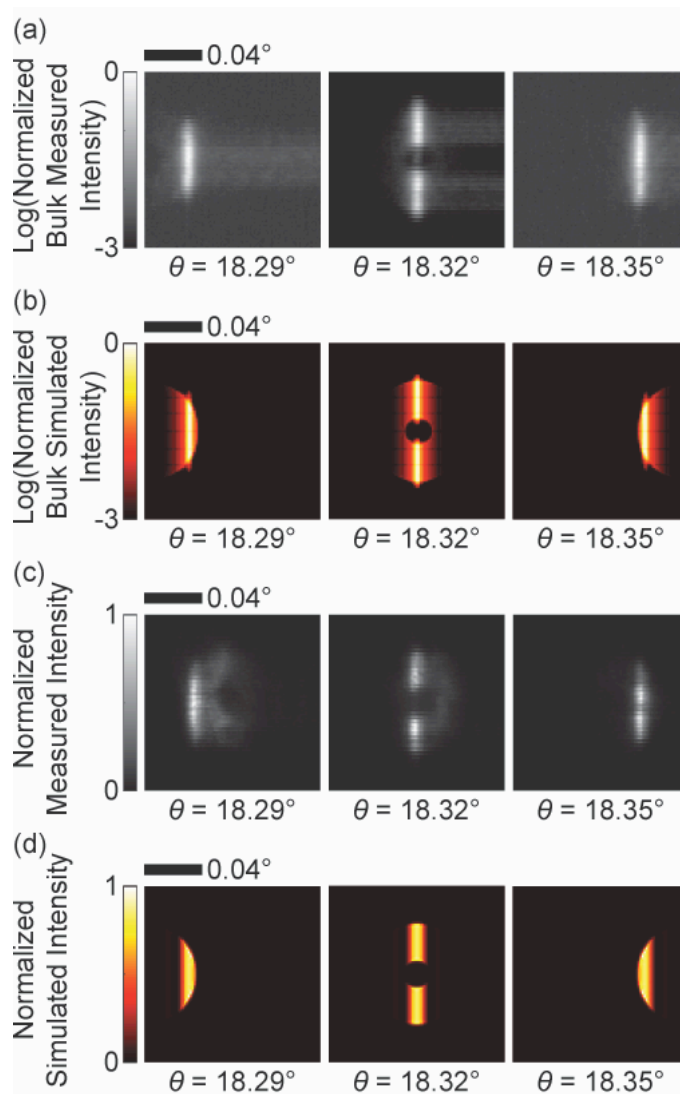


Figure 4.4 (a) Diffraction patterns of the (200) STO bulk Bragg reflection. (b) Simulated dynamical diffraction patterns of the (200) bulk Bragg reflection. (c) Diffraction patterns of the (200) STO sheet. (d) Simulated kinematic diffraction patterns of the (200) STO sheet. rocking curve of bulk STO substrate are shown in Figure 4.4(a). Simulated diffraction patterns for bulk STO at the same incident angle using dynamical diffraction are shown

in Figure 4.4(b). The experimental diffraction pattern from an STO sheet and the corresponding kinematic diffraction simulations are shown in Figure 4.4(c) and 2(d), respectively.

The angular widths of the high-intensity regions of the diffractions patterns in Figure 4.4 are significantly different for the STO sheet and bulk STO. In the case of the sheets, for which the kinematic approximation is appropriate, the width of the reflection is inversely proportional to the number of atomic planes illuminated by the x-ray beam, leading to the relatively broad intensity distribution in Figure 4.4(c) and 2(d). The angular width of the diffraction from the STO sheet in the diffraction pattern is 9 mdeg, in agreement with the 9 mdeg prediction from the kinematic simulation shown at the nominal Bragg condition of Figure 4.4(d). The predicted width of the Darwin reflectivity curve from the bulk STO in the dynamical diffraction simulation is 3 mdeg, and measured to be 4 mdeg [30,31]. The measured angular width is also increased due to the effective variation in the Bragg angle introduced by the approximately 2 eV energy bandwidth of the x-ray radiation, which is 4 mdeg.

4.3 Analysis and Discussion of Nanodiffraction Patterns

The x-ray beam divergence leads to great difficulty when trying to distinguish the effect of tilt from strain. Figure 4.5(a) shows a simulated diffraction pattern at the nominal Bragg condition while Figure 4.5(b) and (c) show a simulated diffraction pattern from a crystal that has been tilted and strained respectively. The strain and tilt are chosen such that they lead to similar shifts in the diffracted x-ray intensity on the detector. In the case of this ideal simulation, the two diffraction patterns are discernable using the direction of the curvature from the outer edge of the zone plate. In experimental diffraction data,

however, fine features resulting from ideal focusing optics and perfect samples are unsuitable to distinguish the origin of angular shifts. A more robust feature, such as the

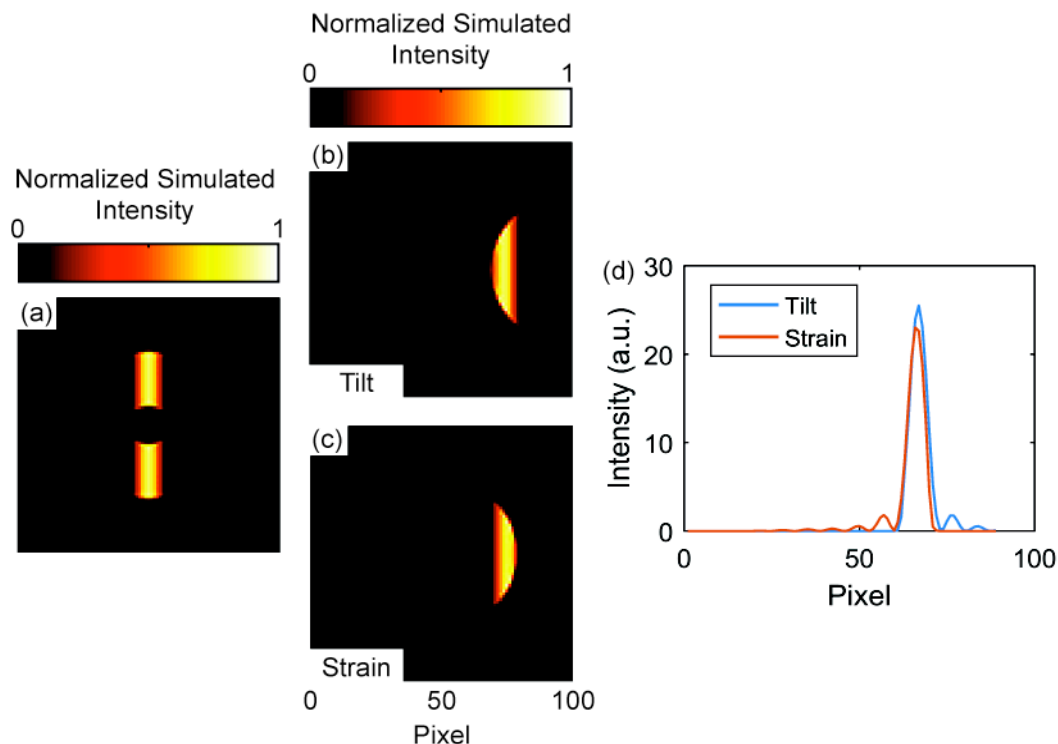


Figure 4.5 (a) Simulated diffraction pattern at the nominal Bragg condition. (b) Tilt and (c) strain resulting in the sample angular shift in the diffraction pattern. (d) The integrated intensity of the tilt and strain shown as a function of pixel in the horizontal direction highlighting the difficulty in distinguishing the effects of tilt and strain.

location of the peak intensity in terms of pixels on the detector is also unsuitable as shown in Figure 4.5(d), which shows that the changes in strain and tilt produce overlapping x-ray peaks when the changes are within the angular divergence of the zone plate. The divergence of the focused beam thus requires analysis different from what is available through the study of a single x-ray diffraction pattern.

The strain and tilt can be separately measured in the diffraction study by using an analysis procedure involving collecting diffraction patterns over a range of incident angles greater than the zone plate divergence. This was illustrated by using a series of simulated diffraction patterns. The distribution of intensity along the vertical direction of

the diffraction patterns, e.g., Figure 4.4, does not depend on the STO lattice parameter or on the tilt in the θ angular direction. Each diffraction pattern can thus be integrated along the vertical direction to obtain the angular distribution of diffracted x-ray intensity at each incidence angle. The simulated vertically integrated intensity is plotted as a function of θ in Figure 4.6(a), which has vertical and horizontal axes related to the θ and 2θ angles,

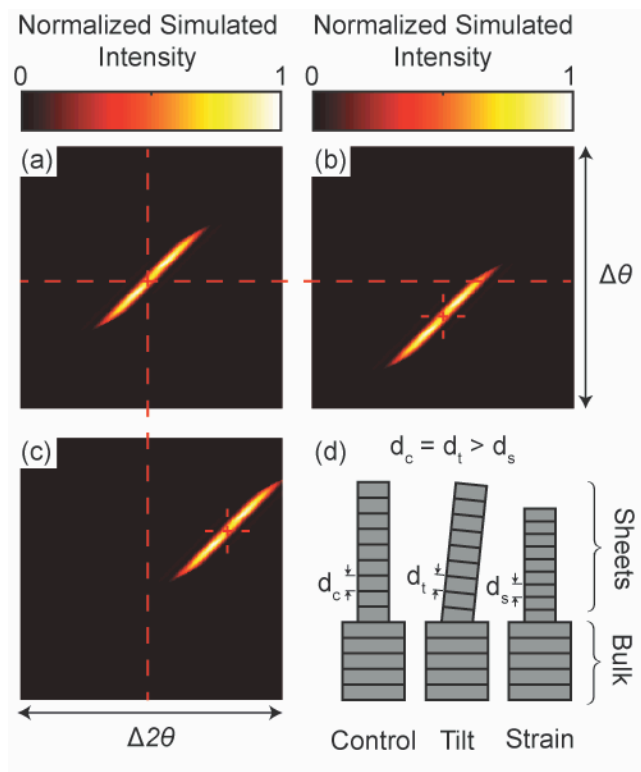


Figure 4.6 Simulated STO rocking curves for (a) unstrained STO with zero tilt, (b) unstrained STO with a 0.1° tilt, and (c) -0.2% strained STO with zero tilt. The dotted lines and crosses are a guide to the eye. (d) Schematic of tilt and strain in the STO sheets with lattice spacing d .

respectively. The plots in Figure 4.6(a) were used to separately determine the shifts of the diffraction patterns $\Delta\theta$ and $\Delta 2\theta$ with respect to the bulk STO. Shifts of the center of the intensity along the $\Delta 2\theta$ direction of Figure 4.6(a) arise from a change in the lattice parameter caused by elastic strain. Shifts in the $\Delta\theta$ direction arise from changes in the orientation of the STO crystal without change in lattice parameter.

The simulations used to construct Figure 4.6(a) were repeated for a series of combinations of strain and tilt in order to illustrate the effects of the orientation and strain in the STO sheet on the diffraction patterns and confirm the interpretation of the shifts $\Delta\theta$ and $\Delta 2\theta$. Figure 4.6(b) shows a simulated diffraction pattern for an STO sheet with zero strain and an orientation offset by 0.03° . The region of high intensity in Figure 4.6(b) is shifted exclusively in the $\Delta\theta$ direction with respect to the untilted diffraction pattern in Figure 4.6(a). The intensity in Figure 4.6(b) is not shifted in the $\Delta 2\theta$ direction with respect to bulk STO because there is no change in the interplanar spacing. Figure 4.6(c) shows a complementary simulation in which the STO sheet has an in-plane strain of -0.2% and has zero tilt, resulting in a shift along the $\Delta 2\theta$ and $\Delta\theta$ directions. Figure 4.6(d) is a schematic representation of STO sheets with (i) zero tilt and zero strain, (ii) non-zero tilt, and (iii) non-zero strain.

The strain was evaluated by measuring values of $\Delta 2\theta$ using x-ray rocking curves acquired across a $9\ \mu\text{m}$ wide \times $4\ \mu\text{m}$ high area of x-ray beam positions on STO sheets. Histograms of strain measured at 43 locations within these areas of STO sheets with and without SiN stressor layers are shown in Figure 4.7(a). The strain in each case was computed using the angle of the bulk STO substrate (200) reflection as a reference. The histogram of strain in the STO sheets without SiN stressor layers is shifted by approximately 6×10^{-4} with respect to bulk STO, reflecting the effect of the FIB processes used to create the thin sheets. A similar value of the strain was observed in previous studies of FIB-patterned STO, and has a magnitude consistent with the formation of point defects during ion-beam milling [19].

The strain measured from the STO sheet with the stressors has a different distribution than the sheet without the stressor, as shown in Figure 4.7(a). The strain distribution of the STO with SiN layers shows that the most commonly measured strain was shifted to higher values than the bare STO sheet. Small changes in the interplanar spacing on the (200) planes are expected from point-to-point variation in composition or irregularities in the SiN-STO interfaces. The strain is evaluated using the statistical mode rather than the mean because of the non-Gaussian distribution of the measured values and the small number of points in bare STO sheets. The difference between the modes of the strain distributions shown in Figure 4.7(a) is 1.3×10^{-4} . This measured strain agrees with the mechanical model prediction of 1.4×10^{-4} .

4.4 Conclusion

This observation of elastic strain sharing in STO sheets also points to a broader application of this approach. Figure 4.7(b) illustrates a range of values of strain that can be produced with strain sharing by modifying the controllable parameters: thickness and stress-thickness product. In this example, the strain predicted using the mechanical model is shown as a function of thickness of the STO sheet for stress-thickness products of $P = 15, 28, \text{ and } 45 \text{ GPa}\cdot\text{nm}$. These values of P are within the range of values available in SiN deposition [26]. The strain measured for the 510 nm-thick STO sheet probed in this experiment is indicated as an asterisk within Figure 4.7(b) and falls near the black line representing the stress-thickness product applied in this experiment.

Elastic strain sharing in lithographic structures is a widely applicable strategy for producing elastically strained complex oxides. STO sheets can be elastically strained through the deposition of SiN thin films to induce strain with magnitude sufficiently large

to modify physical properties relevant to magnetism, ferroelectricity, and ionic transport. Selecting the stress-thickness product in the stressors and the thicknesses of the sheets provides the opportunity to precisely choose the elastic strain. This control is achieved

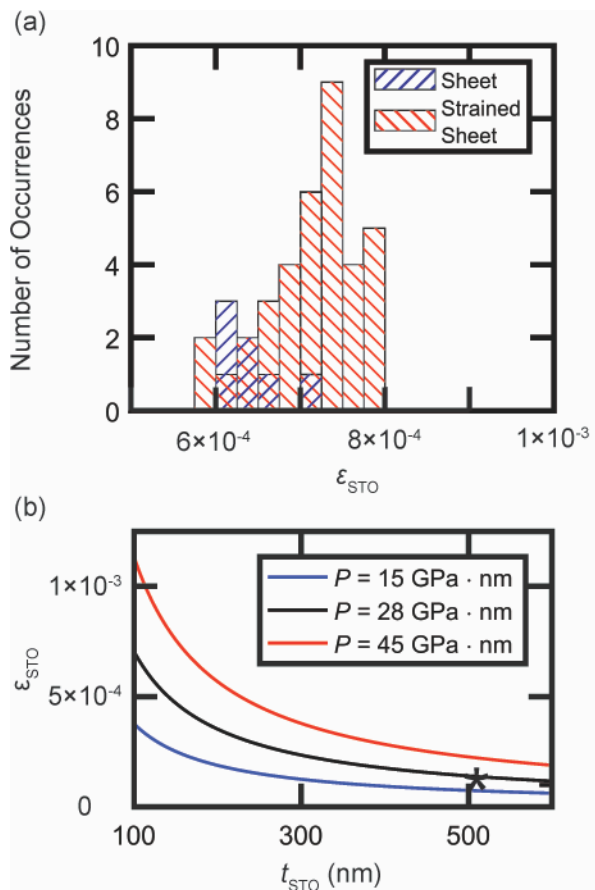


Figure 4.7 Histogram of strain measured from the (200) rocking curves in the STO sheets without a SiN layer (blue cross hatched) and with a SiN layer (red cross hatched). The change in lattice parameter of the bare STO sheet arises from the FIB processing. The increase in lattice parameter after SiN deposition agrees with the mechanical prediction for an elastically strained sheet. (b) Predicted strain in STO sheets as a function of thickness of the STO sheet for different stress-thickness product. The black line is the experimental stress, and the black asterisk represents the experimentally measured stress and strain.

without changes in composition or increases in dislocation density, as evidenced by the observed rocking curve widths [19]. The approach can be extended to sheets of larger lateral size and can provide a route to the fabrication of complex oxides with improved properties for a range of technological applications in electronics and optics.

4.5 References

- [1] D. J. Kim, J. P. Maria, A. I. Kingon, and S. K. Streiffer, *J. Appl. Phys.* **93**, 5568 (2003).
- [2] K. J. Choi, M. Biegalski, Y. L. Li, A. Sharan, J. Schubert, R. Uecker, P. Reiche, Y. B. Chen, X. Q. Pan, V. Gopalan, L.-Q. Chen, D. G. Schlom, and C. B. Eom, *Science* **306**, 1005 (2004).
- [3] C. Donnerer, Z. Feng, J. G. Vale, S. N. Andreev, I. V. Solovyev, E. C. Hunter, M. Hanfland, R. S. Perry, H. M. Rønnow, M. I. McMahon, V. V. Mazurenko, and D. F. McMorrow, *Phys. Rev. B* **93**, 174118 (2016).
- [4] P. G. Radaelli, G. Iannone, M. Marezio, H. Y. Hwang, S. W. Cheong, J. D. Jorgensen, and D. N. Argyriou, *Phys. Rev. B* **56**, 8265 (1997).
- [5] B. Yildiz, *MRS Bull.* **39**, 147 (2014).
- [6] G. Catalan, J. Seidel, R. Ramesh, and J. F. Scott, *Rev. Mod. Phys.* **84**, 119 (2012).
- [7] D. G. Schlom, L.-Q. Chen, C. J. Fennie, V. Gopalan, D. A. Muller, X. Pan, R. Ramesh, and R. Uecker, *MRS Bull.* **39**, 118 (2014).
- [8] H. P. Sun, W. Tian, X. Q. Pan, J. H. Haeni, and D. G. Schlom, *Appl. Phys. Lett.* **84**, 3298 (2004).
- [9] D. G. Schlom, L. Q. Chen, X. Pan, A. Schmehl, and M. A. Zurbuchen, *J. Am. Ceram. Soc.* **91**, 2429 (2008).
- [10] Y. A. Soh, P. G. Evans, Z. Cai, B. Lai, C. Y. Kim, G. Aeppli, N. D. Mathur, M. G. Blamire, and E. D. Isaacs, *J. Appl. Phys.* **91**, 7742 (2002).
- [11] S. E. Thompson, M. Armstrong, C. Auth, M. Alavi, M. Buehler, R. Chau, S. Cea, T. Ghani, G. Glass, T. Hoffman, C. H. Jan, C. Kenyon, J. Klaus, K. Kuhn, Z. Ma,

- B. McIntyre, K. Mistry, A. Murthy, B. Obradovic, R. Nagisetty, P. Nguyen, S. Sivakumar, R. Shaheed, L. Shifren, B. Tufts, S. Tyagi, M. Bohr, and Y. El-Mansy, *IEEE Trans. Electron Devices* **51**, 1790 (2004).
- [12] A. M. Jones, J. L. Jewell, J. C. Mabon, E. E. Reuter, S. G. Bishop, S. D. Roh, and J. J. Coleman, *Appl. Phys. Lett.* **74**, 1000 (1999).
- [13] M. El Kurdi, M. Prost, A. Ghrib, S. Sauvage, X. Checoury, G. Beaudoin, I. Sagnes, G. Picardi, R. Ossikovski, and P. Boucaud, *ACS Photonics* **3**, 443 (2016).
- [14] P. H. Lim, S. Park, Y. Ishikawa, and K. Wada, *Opt. Express* **17**, 16358 (2009).
- [15] D. M. Paskiewicz, D. E. Savage, M. V Holt, P. G. Evans, and M. G. Lagally, *Sci. Rep.* **4**, 4218 (2014).
- [16] D. Paskiewicz, R. Sichel-Tissot, E. Karapetrova, L. Stan, and D. D. Fong, *Nano Lett.* **16**, 534 (2016).
- [17] D. Lu, D. J. Baek, S. S. Hong, L. F. Kourkoutis, Y. Hikita, and H. Y. Hwang, *Nat. Mater.* **15**, 1255 (2016).
- [18] B. W. Li, M. Osada, T. C. Ozawa, Y. Ebina, K. Akatsuka, R. Ma, H. Funakubo, and T. Sasaki, *ACS Nano* **4**, 6673 (2010).
- [19] J. A. Tilka, J. Park, K. C. Sampson, Z. Cai, and P. G. Evans, *APL Mater.* **4**, 126108 (2016).
- [20] S. R. Burns, J. M. Gregg, and V. Nagarajan, *Adv. Funct. Mater.* **26**, 8367 (2016).
- [21] J. Mayer, L. A. Giannuzzi, T. Kamino, and J. Michael, *MRS Bull.* **32**, 400 (2007).
- [22] P. M. Mooney, G. M. Cohen, J. O. Chu, and C. E. Murray, *Appl. Phys. Lett.* **84**, 1093 (2004).
- [23] A. G. Beattie and G. A. Samara, *J. Appl. Phys.* **42**, 2376 (1971).

- [24] A. G. Noskov, E. B. Gorokhov, G. A. Sokolova, E. M. Trukhanov, and S. I. Stenin, *Thin Solid Films* **162**, 129 (1988).
- [25] P. Temple-Boyer, C. Rossi, E. Saint-Etienne, and E. Scheid, *J. Vac. Sci. Technol. A* **16**, 2003 (1998).
- [26] Y. Toivola, J. Thurn, R. F. Cook, G. Cibuzar, and K. Roberts, *J. Appl. Phys.* **94**, 6915 (2003).
- [27] P. A. Flinn, D. S. Gardner, and W. D. Nix, *IEEE Trans. Electron Devices* **34**, 689 (1987).
- [28] J. A. Tilka, J. Park, Y. Ahn, A. Pateras, K. C. Sampson, D. E. Savage, J. R. Prance, C. B. Simmons, S. N. Coppersmith, M. A. Eriksson, M. G. Lagally, M. V. Holt, and P. G. Evans, *J. Appl. Phys.* **120**, 15304 (2016).
- [29] A. Ying, B. Osting, I. C. Noyan, C. E. Murray, M. Holt, and J. Maser, *J. Appl. Cryst.* **43**, 587 (2010).
- [30] A. Pateras, J. Park, Y. Ahn, J. A. Tilka, M. V. Holt, C. Reichl, W. Wegscheider, T. A. Baart, J. P. Dehollain, U. Mukhopadhyay, L. M. K. Vandersypen, and P. G. Evans, **Submitted**, (2017).
- [31] J. Als-Nielsen and D. McMorrow, *Elements of Modern X-Ray Physics*, Second Edition (John Wiley & Sons, Ltd, 2011).

5 Lateral Solid-Phase Epitaxy in Complex Oxide Sheets

5.1 Introduction

The functional properties of complex oxides include ferroelectricity, magnetism, and the coexistence of these properties in multiferroic materials. Each of these properties depend sensitively on the conditions under which crystalline thin films or nanostructures are fabricated [1,2]. In ferroelectric thin films and nanomaterials, for example, fabrication effects such as the generation of strain via lattice mismatch can have a crucial role in defining the direction and domain pattern of the remnant polarization [3]. The strain and orientational effects can be used to manipulate functional properties, including shifting the ferroelectric transition temperature [4,5].

Crystalline oxide thin films are conventionally synthesized through vapor-phase deposition techniques, such as molecular beam epitaxy (MBE) or pulsed laser deposition (PLD), for which the epitaxial relationships and domain formation mechanisms have been widely studied. An important aspect of these approaches is that the final crystalline form of the thin film is created during the deposition of the materials. These approaches typically rely on surface diffusion to form crystalline phases directly on a two-dimensional surface [6–8]. One limitation for techniques such as MBE or PLD is the inability to create thin films with complex geometries. High quality conformal coatings have been successfully created using atomic layer deposition (ALD) for many oxide materials. [9] For complex oxide systems the temperature required to create a crystalline thin film is often greater than the maximum temperatures typically tolerated by the organic precursors used in ALD. [10]

An alternative epitaxial growth process called solid-phase epitaxy (SPE) relies on a process by which a crystalline thin film is formed through the crystallization of an initially amorphous thin film. SPE occurs at relatively low temperatures, and can have different kinetic constraints than conventional growth techniques, and even lead to the formation of bulk thermodynamically unstable phases [11–13]. The low temperatures required to create thin films via SPE also have the advantage of requiring a low thermal budget. This has been a key issue in the development of semiconductor devices where thermal annealing can have the detrimental effects of mechanical relaxation through the introduction of dislocations, or a reduction in the abruptness of interfaces through the diffusion of dopant atoms [14,15]. Ultimately, the range of geometries and materials that capitalizes on SPE can be broadened with greater understanding of the fundamental mechanisms governing the crystallization of complex oxide thin films.

Previous work on the SPE of SrTiO_3 (STO) from STO (001) single crystals and SiO_2/Si (001) crystalline substrates has provided insight into the nucleation and growth of STO through SPE. Figure 5.1 shows a schematic of the SPE tested previously. The critical insight is that the rates of nucleation and growth depend on whether a crystalline/amorphous interface is created during the deposition process [16]. In the homoepitaxial SPE example shown in Figure 5.1(a) the crystalline/amorphous interface begins to move vertically toward the surface immediately upon annealing. The amorphous STO thin film immediately crystallizes because the pre-existing crystalline template provided by the (001) STO substrate eliminates the need for the creation of an STO nucleus before crystal growth can occur.

Figure 5.1(b) shows a schematic of the nucleation and growth of the STO on the $\text{SiO}_2/(001)$ Si substrate demonstrating a period of time after annealing has begun in which there is no SPE because the STO must first undergo a nucleation step before growth. The nuclei created within the amorphous STO deposited on $\text{SiO}_2/(001)$ Si are

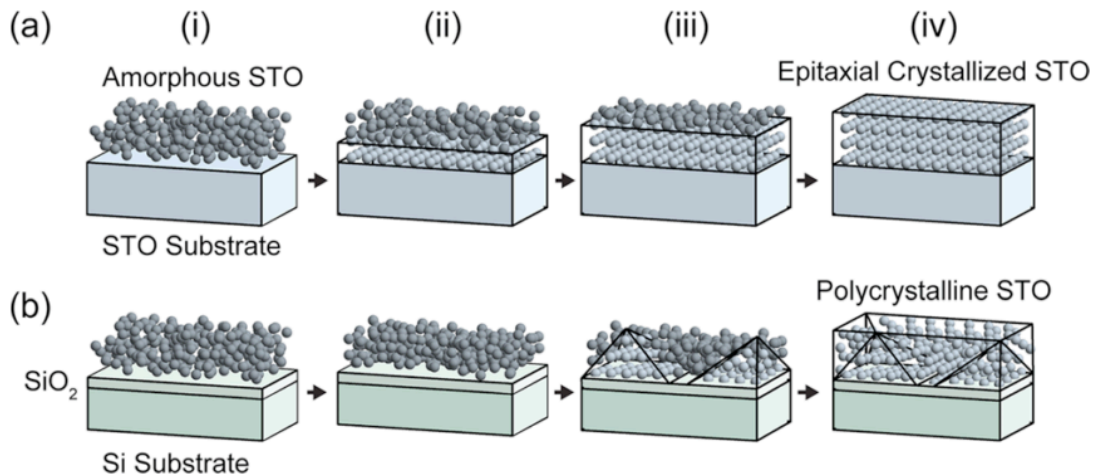


Figure 5.1 (a) Schematic of SPE of STO on STO: (i) amorphous STO as deposited on an (001) crystalline STO substrate, (ii and iii) crystallization of STO as the crystalline/amorphous interface moves toward the surface, (iv) fully crystallized STO. (b) Schematic of SPE of STO on $\text{SiO}_2/(001)$ Si: (i) amorphous STO as deposited on the $\text{SiO}_2/(001)$ Si substrate, (ii) period of annealing during which no nucleation and growth of the crystalline STO forms, (iii) nucleation and growth of crystalline STO into amorphous STO, (iv) fully crystallized polycrystalline STO on $\text{SiO}_2/(001)$ Si. Taken from Chen *et al.* (2017).

distributed stochastically throughout the bulk of the film, at the surface, or at the SiO_2/STO interface. The resulting thin film is a polycrystalline as shown in the final panel of Figure 5.1(b).

A systematic study of SPE of STO on both single crystal (001) STO and $\text{SiO}_2/(001)$ Si provided insight into the SPE of STO in more complicated systems. The incubation time between the start of thermal annealing and the nucleation of a crystalline STO phase sets a hypothetical upper limit to the annealing time. During this time no nuclei are expected to form in an amorphous STO thin film. The templated growth process of STO on STO, however, requires no nuclei formation and can begin

simultaneously with thermal annealing. The differences in the crystallization and growth processes of amorphous STO between SiO₂/(001) Si and (001) STO substrates can be exploited to create systems that exhibit large lateral SPE. An amorphous STO thin film deposited on an SiO₂/(001) Si substrate that is exposed to sparsely distributed STO seed

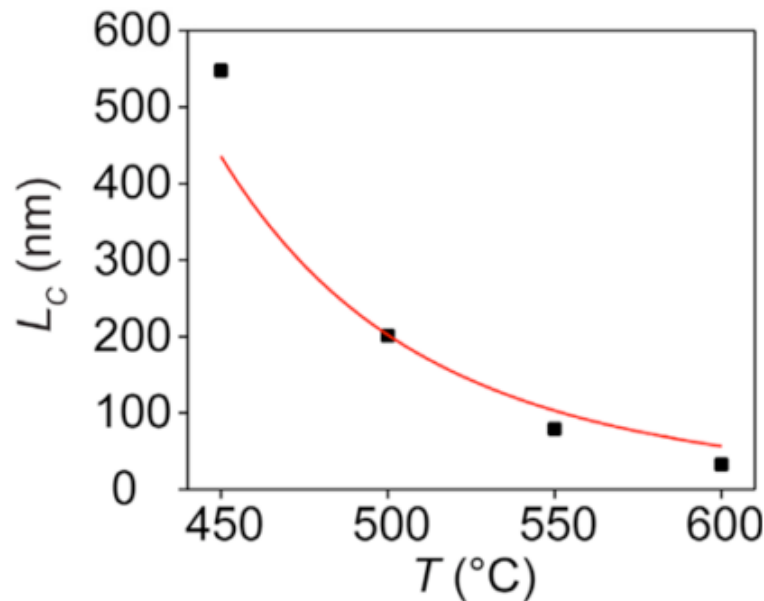


Figure 5.2 Minimum distance, L_C , that can be crystallized before nucleation is expected to take place away from seed crystal. Adapted from Chen *et al.* (2017).

crystals and annealed will exhibit crystal growth from the STO seeds exclusively so long as the annealing time is less than the incubation time. The shortest possible distance that SPE from STO can proceed, without encountering an STO crystal that nucleated randomly on the SiO₂/(001) Si substrate, is represented by a scenario in which the randomly created nucleus appears directly next to the crystalline/amorphous boundary exactly at the end of the incubation time. The hypothetical prediction for that distance, L_C , at a given temperature is the product of the incubation time and growth velocity at that temperature. L_C is plotted as a function of temperature in Figure 5.2.

Two systems are described in the study of SPE presented in this chapter: (i) homoepitaxial growth of STO from isolated nanoscale STO seed crystals and (ii) the heteroepitaxial growth of STO from millimeter-scale SrRuO₃ (SRO) single-crystal sheets. Two experiments that probe different aspects of the crystallization of complex oxides using SPE were used to study two systems of interest. The hypotheses underpinning these experiments are directly derived from the concepts described in the previous paragraph. Specifically, nucleation and growth can be separately controlled and that nucleation is relatively slow away from crystalline interfaces. In the case of an SRO seed crystal, the STO undergoes solid-phase heteroepitaxy to form a crystalline STO thin film above the SRO seed. Additionally, micron size grains of STO grow laterally from the SRO with an out-of-plane orientation different from the SRO. Crystalline STO grown from STO seeds has also been used to study the lateral growth of the crystalline/amorphous STO interface. The lateral SPE studied in this chapter has been used to measure growth velocities and verify the temperature range over which crystals can grow laterally without interacting with crystals nucleated at locations other than the crystalline seed.

The key impacts of this chapter are demonstrating lateral SPE over microns and measuring the growth rate. Previous experiments in these systems indicated that lateral growth across long distances was possible, but did not provide a means for testing that hypothesis. This chapter presents a change in the geometry that allows for two-dimensional planar growth using complex oxide seeds to template SPE. The demonstration of large lateral growth distances is highly encouraging for the prospect of these systems to create complex non-planar or three-dimensional thin films through SPE.

The measured growth rate of the lateral SPE is in excellent agreement with the measured through vertical growth rate. These growth rates pose interesting questions for future work on understanding the mechanism of lateral SPE more thoroughly.

5.2 Lateral Solid-Phase Epitaxy of SrTiO₃ from SrRuO₃ Seed Crystals

The SRO seeds on Si were created by D. M. Paskiewicz at Argonne National Laboratory and provided to the Evans's group for further processing and characterization. The processing techniques were based on epitaxial lift-off and are summarized by the

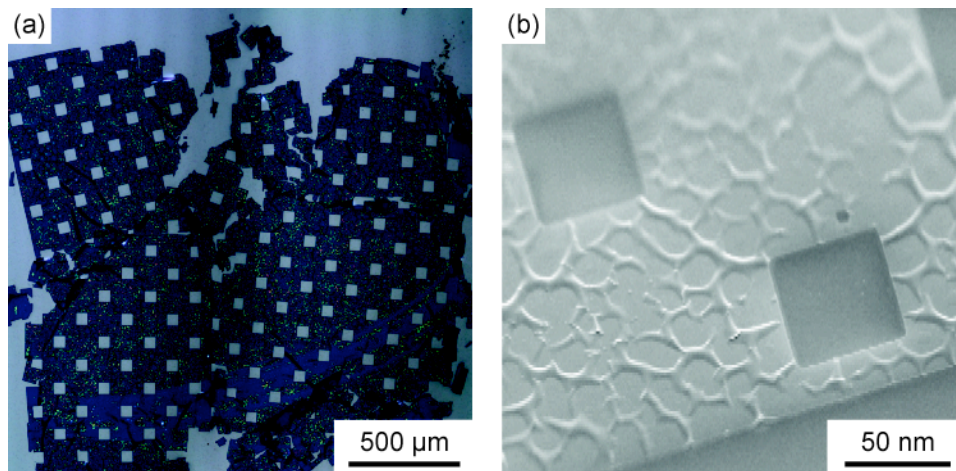


Figure 5.3 (a) Optical image of the SRO seed after it has been transferred to the a Si substrate. (b) SEM image of the same SRO sheet. The wrinkles present in the SRO are a defect from the imperfect transfer process.

following [17]. TiO₂-terminated STO was patterned with photoresist to create 50×50 nm² holes. Amorphous MgO was sputtered deposited on the surface, and acetone was used to remove the photoresist leaving behind MgO pillars. SRO was epitaxially deposited on STO with off-axis RF sputtering, and the MgO mask was selectively etched away with a phosphoric acid (H₃PO₄) solution. The SRO sheets were released by partially dissolving the STO substrate in HF/HNO₃/H₂O and floated to a new Si substrate creating the structure shown in Figure 5.3. The final SRO was 50 nm thick with an area of 2×2

mm² and has 50 × 50 nm² holes on a square grid with 142 nm spacing. The large lateral extent of the seed as well as the periodic arrangement of the holes is readily apparent in Figure 5.3(a). The nanoscale imperfections near the holes and sharp boundaries of the SRO are shown in Figure 5.3(b). The (001) direction of SRO is normal to the surface of the Si (001) substrate to which it was transferred. The SRO/STO heterostructure was created by sputtering an 60 nm thick amorphous layer of STO onto the (001) SRO seed on an (001) Si substrate, as shown in Figure 5.4(b). The heterostructure was annealed at 450 °C for 36 h, resulting in epitaxy on the top of the seed and lateral crystallization from its edges as shown in Figure 5.4(c).

STO thin films that have undergone various annealing conditions were mounted and then aligned with the focused x-ray nanoprobe at Station 26 ID-C of the Advanced Photon Source. The experiments employed an x-ray beam with a photon energy of 9 keV. The samples were aligned using the (004) Bragg reflection of the Si substrate supporting the SRO sheets. A charge-coupled device (CCD) area detector was employed to detect the diffracted x-ray intensity. The x-ray nanoprobe experiments were carried out using three key parameters of the SRO/STO structure: the (002) Bragg reflections of both the materials and the fluorescence of the Ru atoms in the SRO. The out-of-plane (002) Bragg reflection of SRO is at $2\theta = 41.1^\circ$, which is 0.4° lower in 2θ than the out-of-plane (002) STO Bragg reflection. The x-ray detector spans an angular range of 1.3° in 2θ . The angular ranges of the detector and Bragg reflections combine with the widths of SRO and STO Bragg reflections and the 0.4° convergent x-ray beam allow the incident angle to be chosen to capture diffracted x-ray intensity from both materials simultaneously. The total intensity of (002) reflection was an important aspect of understanding the location and

orientation of the SRO and STO, so all of the angular intensity scattered from the divergence zone plate was used to evaluate the presences of crystalline (001) STO. The sample was rastered through the x-ray beam to create a two-dimensional map of the diffracted signal. Additionally, the Ru fluorescence is captured to easily distinguish and verify the boundary of the SRO seed crystal.

A comparison of the (002) STO Bragg reflection intensity and the Ru

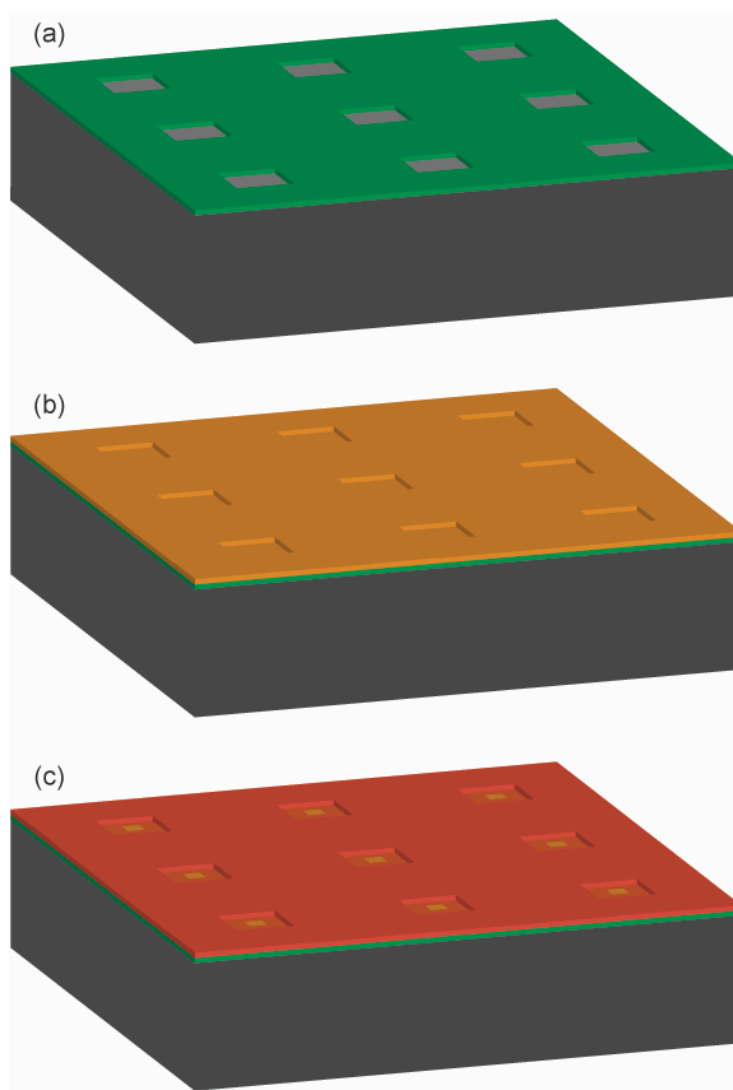


Figure 5.4 Schematic of the lateral SPE of STO on single crystal SRO seeds (a) 50 nm thick SRO seeds, shown in green, with 50 nm square holes spaced throughout the structure that has been transferred to a Si (001) substrate. (b) 50 nm thick layer of amorphous STO is sputtered over the whole surface. (c) The heterostructure is annealed at 450 C for various times. The dark red represents the (002) heteroepitaxially STO on SRO, the dark orange represents the directionally grown lateral SPE STO, and the light orange is the amorphous STO thin film.

fluorescence as a function of location as the beam is driven off the edge of the SRO seed is shown in Figure 5.5(a). The (002) STO Bragg reflection and Ru fluorescence were used to indicate the location of (002) oriented STO and the single crystal SRO seed respectively. The SRO seed crystal has sharp interfaces leading to abrupt changes in the Ru fluorescence intensity as function of location when the x-ray beam is rastered on and off the SRO seed. The blue line in Figure 5.5(a) is a plot of the Ru fluorescence intensity as a function of location, and the sharp drop in intensity is defined as the location of the edge at distance 0. The (002) STO Bragg reflection intensity, shown in red in Figure 5.5(a), measured simultaneously with the Ru fluorescence indicates the location of heteroepitaxial SPE of STO on SRO. Changes in the (002) intensity as a function of distance indicate the extent to which (002) STO has grown from the edge of the SRO seed. Figure 5.5 shows that the drop in (002) STO intensity and Ru fluorescence intensity are coincident to within tens of nm, and that the (002) STO does not extend laterally over ones of μm away from the STO. To study why the STO (002) reflection does not persist beyond the SRO seed electron backscattered diffraction (EBSD) studies were conducted to learn the crystallinity and orientation of the STO near the SRO seed.

Electrons scattered by more than 90° with respect to the primary beam are considered backscattered electrons. There is a finite probability that some backscattered electrons will be further inelastically scattered as they escape to the free surface. The diffuse background created from this inelastic scattering can be captured by positioning a CCD sufficiently close to the sample and pole piece within a scanning electron microscope (SEM). In order to increase the EBSD signal, the sample is often tilted to an extreme angle with respect to the primary beam, 70° in these experiments. In the case of a

highly perfect crystal, the periodic arrangement of atoms leads to diffraction from the crystal as the inelastically scattered electrons escape the surface. The diffracted electrons are scattered away from their original path by an angle equal to the Bragg angle, θ [18].

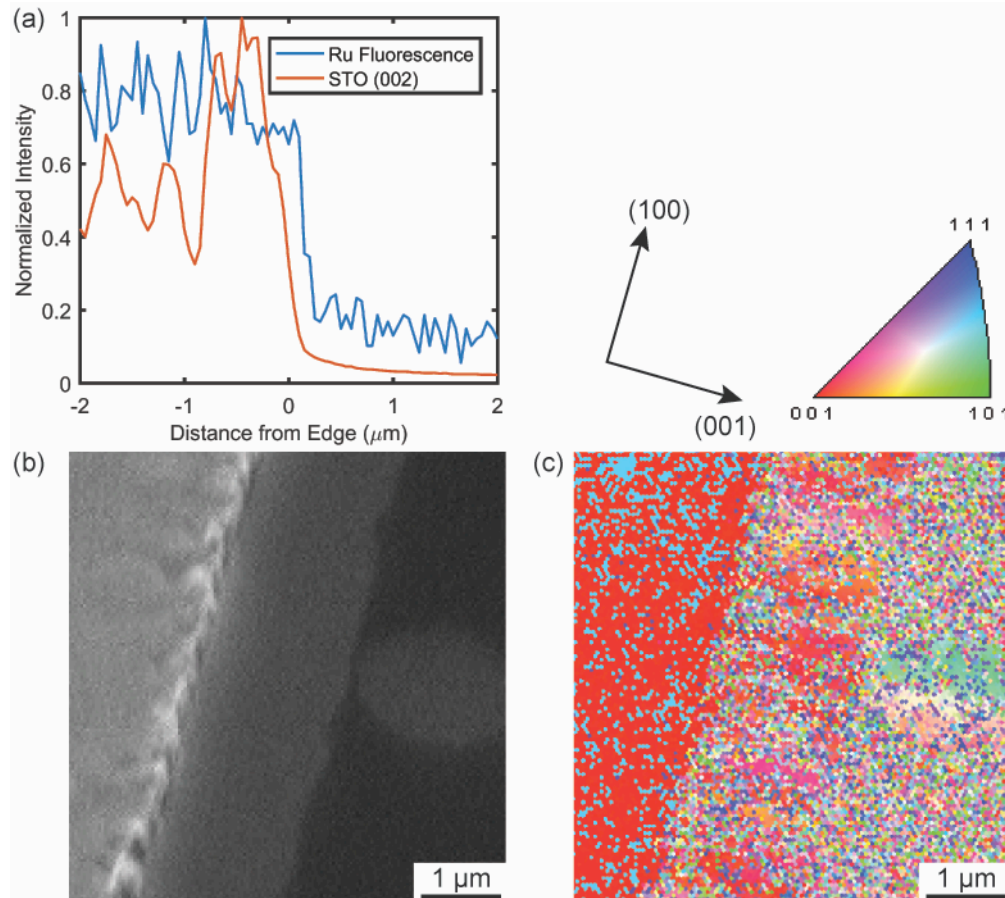


Figure 5.5 (c) X-ray nanodiffraction intensity of the (002) STO peak plotted on the same scale as the Ru fluorescence intensity. The intensity drops in (c) show that the (002) STO ends at the boundary of the SRO seed crystals. (a) Secondary electron SEM image of STO crystallized on SRO. (b) EBDS of the same area shown in (a) with the inverse pole figure color scale corresponding to the directions shown below the image.

This diffraction leads to a series of light and dark parallel lines superimposed on the diffuse background with thickness and direction related to the interatomic spacing and orientation on the crystalline sample. The CCD collects a large angular range of scattered electrons, which allows multiple lines of diffracted intensity to be collected simultaneously. The pattern with which the lines intersect can be used to solve to the

crystallographic orientation of the material being probed. This process repeated at each location through which the electron beam is rastered can be used to create a spatial map of the crystallographic orientation in a technique called orientational imaging microscopy as shown in Figure 5.5.

EBSD provides a powerful complement to the structural information gained at the hard x-ray nanoprobe. The electron diffraction data is acquired quickly – for example, the images shown in Figure 5.5(b) and (c) required roughly 30 min to obtain – and they provide in-plane and out-of-plane orientation information. The hard x-ray nanoprobe can provide structural information such as lattice parameters and crystallographic tilt of buried layers, as well as compositional information through the use of an x-ray fluorescence detector.

Figure 5.5(b) shows a secondary electron SEM image of the SRO/STO structure after 36 h annealing in air. The image is shown for an area at the edge of one of the holes created during the SRO lift-off. These regions near the edge of the holes created by the SRO lift-off are shown schematically in Figure 5.4(c), where heteroepitaxially grown STO on SRO, directed crystal growth of crystalline STO, and amorphous STO are represented by red, dark orange, and light orange respectively. The bright region at the left of Figure 5.5(b) represents the SRO seed with crystalline STO. The grey region in the center of Figure 5.5(b) is an area of crystalline STO with large grains. The darkest region shown to the right of the image is the amorphous STO. The change in contrast as a function of crystallinity and composition in Figure 5.5(b) provides valuable information about the distance of the crystalline/amorphous interface from the SRO seed crystal, which is 1.8 μm . The orientation of the STO crystallized through directed crystal growth cannot be

readily deduced from the SEM image, but it can be compared to the EBSD data shown in Figure 5.5(c) to better illustrate the location of the different orientations shown through EBSD.

Figure 5.5(c) shows an EBSD map of the in-plane orientations of the STO crystalline sheet with the axes directions and color scale depicted above the image. Each location at which the electron beam generated an EBSD pattern is represented by a single colored pixel in the map shown in Figure 5.5(c). The EBSD pattern was used to fit the crystallographic orientation of the STO at the location of the electron beam. That orientation corresponds to a color shown in the color scale at the top of Figure 5.5(c) such that the indices at the corners of the color scale are related to the crystallographic directions shown at the top of Figure 5.5(c). The processes of fitting and coloring each crystallographic orientation is repeated for every pixel shown in Figure 5.5(c) in order to create the EBSD map. The mostly red left region of the EBSD map represents the in-plane (001) orientation of the STO grown heteroepitaxially on the SRO seed, which is consistent with expected orientation of the underlying SRO seed. The randomly colored region to the right of the EBSD map is from the amorphous region of the STO thin film and a result of arbitrarily fitting the background and noise. The in-plane (001) orientation is coincident with the SRO out-of-plane seed crystal. Between the SRO and the amorphous regions, there are large grains of STO oriented with the same in-plane orientation as the SRO. These grains are apparent by the large red regions shown intermittently through the portion of the thin film that has undergone lateral SPE. It is not clear what causes these regions to grow near the SRO, or what sets their orientation.

However, the change in angle is sufficiently large that it would not meet the out-of-plane (002) STO Bragg condition.

The design and creation of the SRO/STO heterostructure capitalized on the incubation time associated with the nucleation of crystalline STO on SiO₂/(001) Si to create crystalline STO that grew over a micron away from the edge of the SRO seed crystal. The (002) direction of SRO was templated onto the STO that was grown directly above the SRO seed indicating vertical SPE. The crystalline STO grown away from the edge of the SRO does not maintain the same out-of-plane orientation but does share a relationship with at least one in-plane direction. The difference between the out-of-plane orientation between the crystalline STO grown on the SRO and the STO grown off the edge indicates that the lateral SPE likely originates from the SRO edge.

5.3 Lateral Solid-Phase Epitaxy of SrTiO₃ from SrTiO₃ Seed Crystals

The work on solid-phase homoepitaxy was extended to the study of lateral SPE of STO on isolated nanoscale STO seeds. The samples based on the STO on STO seeds were created using a method that capitalized on the imperfect contact between a shadow mask and a Si surface. Figure 5.6 is a schematic with a greatly exaggerated vertical scale of the fabrication steps used to create the homoepitaxial STO structure. A stainless steel shadow mask with 200 μm holes was placed on a Si with a native oxide. STO was sputtered onto it as shown in Figure 5.6(a) leaving large areas of amorphous STO after the shadow mask was removed as shown in Figure 5.6(b). The area of the Si substrate open to the deposition process received all of the sputtered flux, while the area of the Si substrate far away from the shadow mask opening was completely shadowed and received no flux. The boundary at the shadow mask openings had an intermediate STO

coverage that decreased with increasing distance from the opening. At some location from the shadow mask openings, the STO coverage was non-zero and sufficiently sparse to create isolated STO seeds. A schematic example of a region sparsely covered STO is

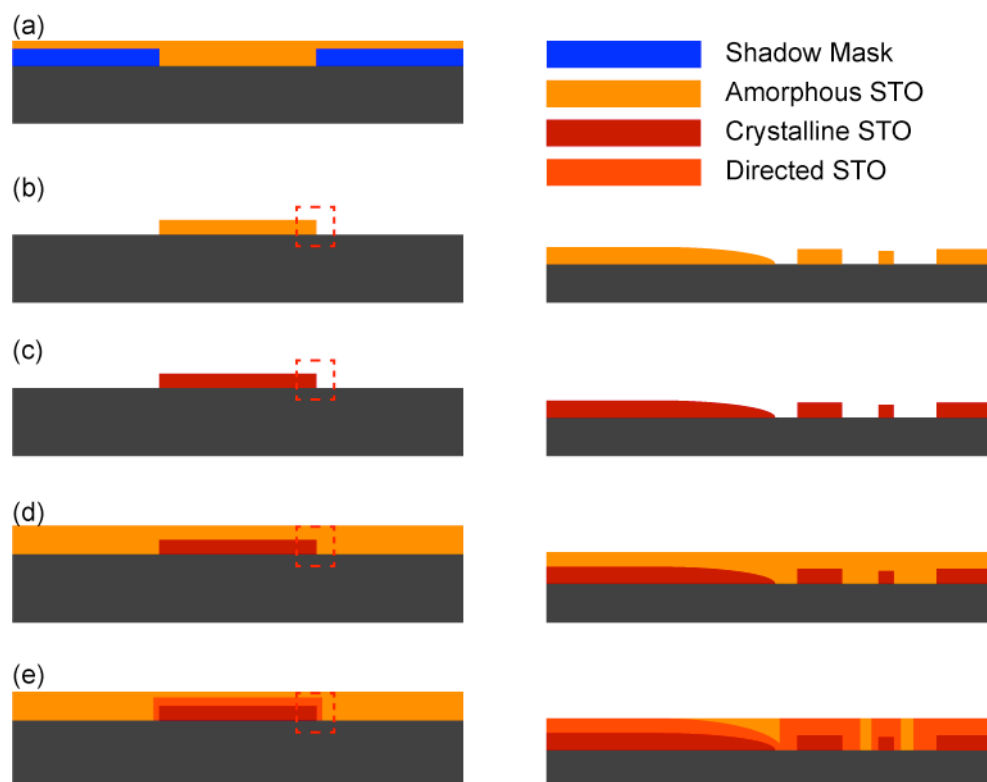


Figure 5.6 Schematic of STO seeds and STO on STO SPE. (a) Amorphous STO deposited through a shadow mask. (b) Mask is removed and leaves behind isolated amorphous STO near the boundary of the shadow mask. (c) The sample is annealed for 3 h at 650 °C. (d) A second amorphous STO layer is deposited over the whole surface. (e). Material is annealed for various times at 450 °C. The dark orange represents the directed crystal growth from the STO crystalline STO seeds.

shown by the right side column of the in Figure 5.6 and correspond to the red dotted boxes shown in the left column. The STO on Si deposited through the shadow mask was annealed at 650 °C for 3 h in order to crystallize the STO show in red in Figure 5.6(c). The crystalline STO seeds sizes range from 100 – 900 nm, and likely have no preferred crystallographic orientation because they were not templated by the underlying Si substrate

The STO seed crystals created using this shadow mask technique were then used to template homoepitaxial SPE. Amorphous STO thin films were sputtered on top of the STO seeds and annealed at 450 °C for times ranging from 4.5 – 36 h in order to explore the time dependence of STO SPE. The crystalline STO created during the first annealing step act as seeds for the subsequent SPE of STO. The light orange layer in Figure 5.6(d) represents a second amorphous STO thin film sputtered onto the surface. The dark orange regions of the thin film shown in Figure 5.6(d), between the red STO crystal and the light

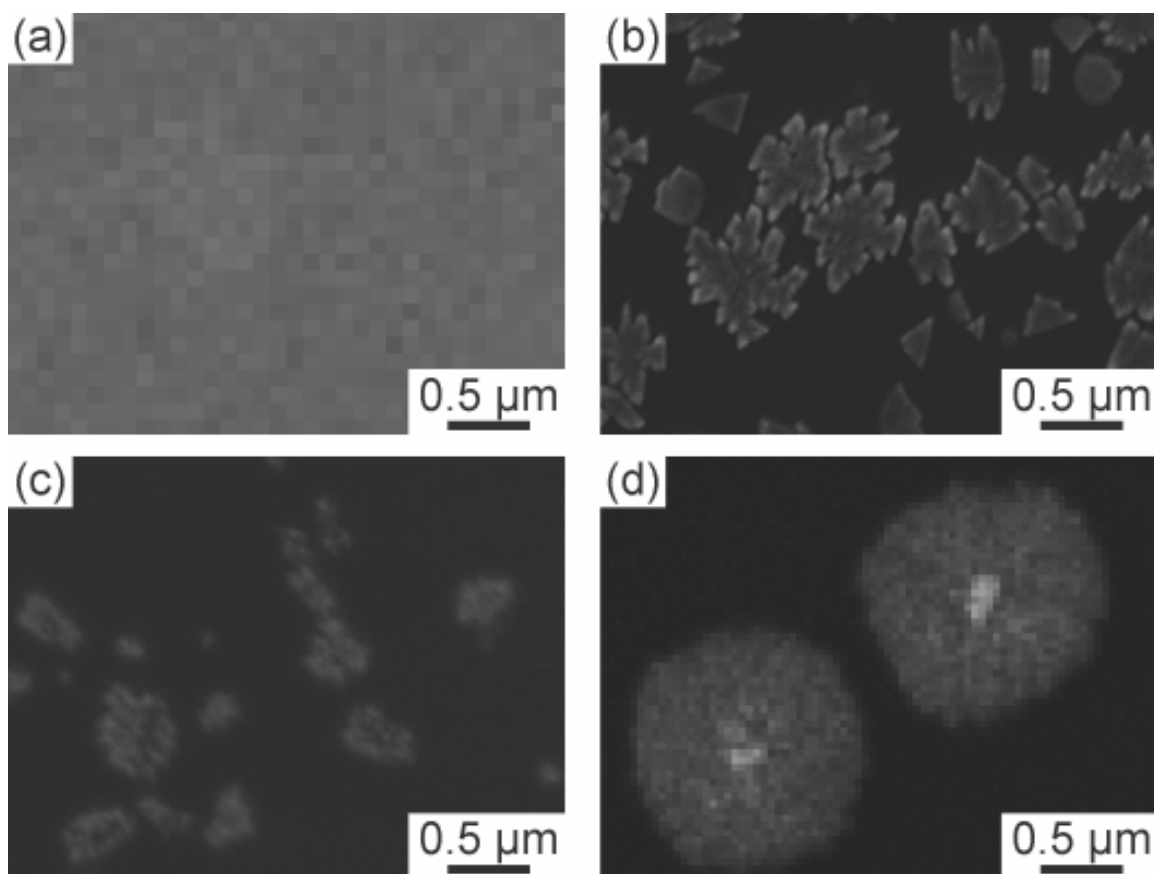


Figure 5.7 Secondary electron SEM images of the STO crystallized from the STO seed. (a) First 60 nm thick amorphous layer. (b) After first anneal at 650 °C for 3 h. (c) Second 60 nm thick amorphous layer. (d) Final structure after annealing at 450 °C for 6 h

orange amorphous STO, represents the directed crystal growth of STO through amorphous STO.

The sizes of the crystallized regions of STO were characterized using SEM. Figure 5.7 shows SEM images of each processing step after the shadow mask has been removed and corresponds to Figure 5.6(b)-(e). The images shown in Figure 5.7 are from

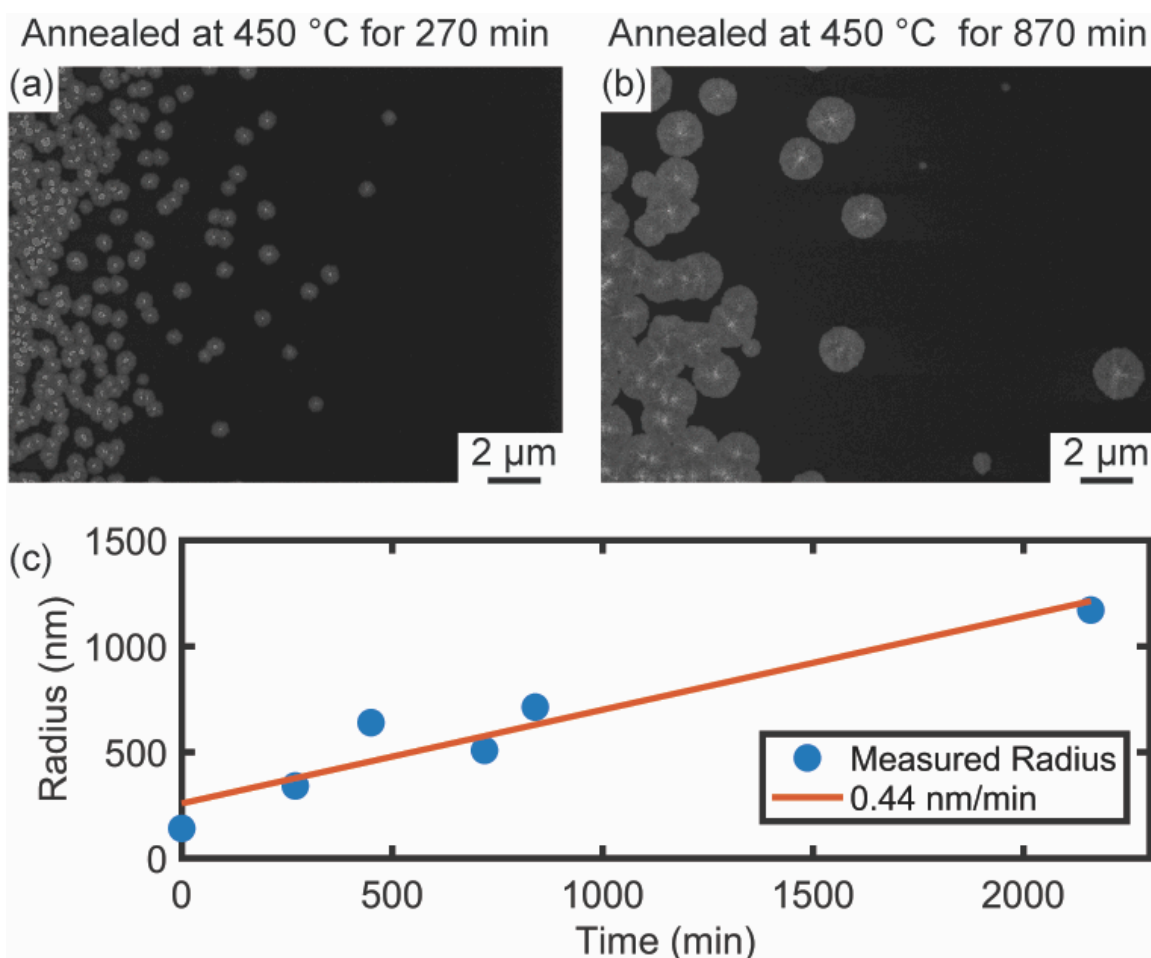


Figure 5.8 (a) Secondary electron SEM image of an STO film that was annealed for 270 min. The gray disks represent crystalline STO that has grown into the dark amorphous region, and the bright objects located in the center of the gray disks are the nucleation sites for the STO growth. **(b)** Similar SEM image taken of an STO film that was annealed for 870 min. **(c)** Scatter plot of the average crystalline radius measured from representative disks within STO films with different annealing times. The data are fit with a line to determine a growth rate of 0.44 nm/min.

a single sample cut into successively smaller portions after each processing step. They do not represent images of the same location of the sample at each step. As a result of using different samples for each SEM image, the coverage of the STO seeds is not uniform because the effects from the distance from the shadow mask boundary are not uniform.

Figure 5.7(a) shows an SEM image after the deposition of the amorphous STO thin film. Figure 5.7(b) is an SEM after 3 h annealing in air at 650 °C. The larger crystals that have multiply facets might be polycrystalline while the smaller crystals with three or four edges are likely single crystal STO. The dark regions between the STO crystals are bare Si, meaning that the STO, Sr, Ti, or some combination of those compounds and elements, can diffuse over hundreds of nm on Si with native oxide over the 3 h at 650 °C. Figure 5.7(c) is an SEM image of the crystalline STO seeds that have had a 60 μm amorphous STO thin film sputtered on top. Figure 5.7(d) is an SEM image of the final laterally crystallized STO after annealing at 450 °C for 6 h. The sizes of the disks shown in Figure 5.7(d) are used to determine the growth rates of lateral SPE in STO.

The final crystalline structures formed through SPE consist of circles of crystalline STO growing into the amorphous STO regions from the original seed where the seeds are sparse as shown in Figure 5.7(d). The radii of the circular crystalline regions are used to measure the growth velocity of crystalline STO at 450 °C. The crystallization from the isolated STO seeds occurs with a different geometric arrangement than in the crystallization on SRO. Due to the large lateral distances crystallized in the amorphous thin films, the vertical SPE from the STO seeds take place over a time scale many times shorter than any lateral growth, and any time associated with vertical SPE before a transition to a purely lateral growth front between the crystalline/amorphous interface can be safely neglected.

Figure 5.8 shows two SEM images of the final homoepitaxial STO structure a 270 min and at 870 min as well as a plot used to measure the lateral growth rate of STO. I expect that increases in the free energy of the crystalline phase through strain will result

in a lower crystallization velocity. However, the measured growth rate shown in Figure 5.8 (c) is 0.44 nm/min, in excellent agreement with the vertical SPE.

5.4 Conclusion

This chapter focuses on the nucleation and growth processes of crystalline STO from amorphous STO on SiO₂/(001) Si, (001) STO and (001) SRO single crystals. The lateral SPE growth of STO from STO seed crystals rate is consistent with the previous growth rate measured in vertical SPE. The SRO/STO structure created a system with directed lateral crystal growth through amorphous STO. Crystalline grains with a lateral extent of more than microns can be fabricated a temperature lower than those typically required for vapor-phase epitaxy. These results provide experimental evidence that SPE is a promising technique for the fabrication of thin films in complex three-dimensional geometry, or in systems requiring relatively low temperatures.

5.5 References

- [1] D. G. Schlom, L. Q. Chen, X. Pan, A. Schmehl, and M. A. Zurbuchen, *J. Am. Ceram. Soc.* **91**, 2429 (2008).
- [2] K. J. Choi, M. Biegalski, Y. L. Li, A. Sharan, J. Schubert, R. Uecker, P. Reiche, Y. B. Chen, X. Q. Pan, V. Gopalan, L.-Q. Chen, D. G. Schlom, and C. B. Eom, *Science* **306**, 1005 (2004).
- [3] R. J. Zeches, M. D. Rossell, J. X. Zhang, A. J. Hatt, Q. He, C.-H. Yang, A. Kumar, C. H. Wang, A. Melville, C. Adamo, G. Sheng, Y.-H. Chu, J. F. Ihlefeld, R. Erni, C. Ederer, V. Gopalan, L. Q. Chen, D. G. Schlom, N. A. Spaldin, L. W. Martin, and R. Ramesh, *Science* **326**, 977 (2009).
- [4] N. A. Pertsev, A. G. Zembilgotov, and A. K. Tagantsev, *Phys. Rev. Lett.* **80**, 1988 (1998).
- [5] N. A. Pertsev, A. K. Tagantsev, and N. Setter, *Phys. Rev. B* **61**, 825 (2000).
- [6] J. L. Macmanus-Driscoll, *Adv. Funct. Mater.* **20**, 2035 (2010).
- [7] L. Yan, Y. Yang, Z. Wang, Z. Xing, J. Li, and D. Viehland, *J. Mater. Sci.* **44**, 5080 (2009).
- [8] D. H. Kim, X. Sun, T. C. Kim, Y. J. Eun, T. Lee, S. G. Jeong, and C. a. Ross, *ACS Appl. Mater. Interfaces* **8**, 2673 (2016).
- [9] A. R. Akbashev, G. Chen, and J. E. Spanier, *Nano Lett.* **14**, 44 (2014).
- [10] H. Maret, D. Weisberg, H. M. Chan, and N. C. Strandwitz, *Cryst. Growth Des.* **16**, 1662 (2016).
- [11] H. Ishiwara, H. Yamamoto, S. Furukawa, M. Tamura, and T. Tokuyama, *Appl. Phys. Lett.* **43**, 1028 (1983).

- [12] K. Taira, Y. Hirose, S. Nakao, N. Yamada, T. Kogure, T. Shibata, T. Sasaki, and T. Hasegawa, *ACS Nano* **8**, 6145 (2014).
- [13] W. Sun, S. Jayaraman, W. Sun, S. Jayaraman, W. Chen, K. A. Persson, and G. Ceder, *Proc. Natl. Acad. Sci.* **112**, 3199 (2015).
- [14] D. C. Houghton, *J. Appl. Phys.* **70**, 2136 (1991).
- [15] M. J. Kumar, S. Member, and S. Janardhanan, **60**, 3285 (2013).
- [16] Y. Chen, M. H. Yusuf, Y. Guan, R. Jacobson, M. G. Lagally, S. E. Babcock, T. F. Kuech, and P. G. Evans, *ACS Appl. Mater. Interfaces* 41034 (2017).
- [17] D. Paskiewicz, R. Sichel-Tissot, E. Karapetrova, L. Stan, and D. D. Fong, *Nano Lett.* **16**, 534 (2016).
- [18] D. Brandon and W. D. Kaplan, *Microstructural Characterization of Materials*, Second (John Wiley & Sons, Ltd, West Susses, England, 2008).

Appendix A

A.1 Create Focused X-ray Beam

```

clear all
tic

%define constants

%physical constants
c_light = 299792458; %speed of light in m/s
h_plank = 4.135667662e-15; %plank's constant in ev*s

%Energy and Materials constants
E = 10000; %energy in eV
n = 1 - (2.9920e-5 - 2.2083e-6*i); %refractive index for Au at 10 keV

%Zone Plate Parameters
Dzp = 160e-6; %diameter of zone plate in m
deLR = 30e-09;
Tzp = 400e-9; %thickness of ZP in m

%Center Stop Parameters
Rcs = 30e-6; %radius of central stop in m
Tcs = 70e-6; %thickness of central stop in m

%Convenient values calculated from provided constants

Rosa = 0.5 * Rcs; %radius of OSA in m. arbitrarily chose to be 50%
%the radius of Rcs
lam = h_plank*c_light/E; %wavelength in m
k = 1/lam; %wavenumber in 1/m
Nzp = Dzp/(4*deLR); % Number of zones in the zone plate. This number
%should be an integer, Dzp and deLR can be slightly altered if needed
Rzp = Dzp/2; % Radius of the Zone Plate in m
PHIzp = (2*pi/lam)*(n-1)*Tzp; %Phaseshift caused by the odd zones on
%the zone plate
PHIcs = (2*pi/lam)*(n-1)*Tcs; %Phaseshift caused by the central stop
Lf = (4*Nzp*(deLR)^2)/lam; %Focal distance of the zone plate in m
Losa = (Lf - (Lf*Rosa/(Rzp)))*1.1; %distance between the zone plate
%and OSA in m. The distance has been arbitrarily chosen to be closer
%than the focal length without interacting with the 1st order focus

%calculate the beam at the OSA

stepSize = 5e-11; % steps the wavefield at the OSA is discretized into.
%This sets the stepsize for later numerical integration
Z = Losa;
R = (0:stepSize:Rosa);

```

```

RzOSA = zeros(1,numel(R));

parfor k = 1:numel(R)
    k;

    fun = @(rho) exp((1i * pi * (1/lam) * rho.^2)./Z).* ...
        besselj(0, ((2 .* pi .* R(k) .* rho)./(lam.*Z))).* ...
        Uzp_phase( rho, lam, Lf, PHIZp, PHICs, Rzp, Rcs).* rho;
    q = integral(fun,0,Rzp,'RelTol',0,'AbsTol',1e-14);
    RzOSA(k) = 2 * pi * exp(2*pi * 1i * Z / lam)/(1i*lam*Z) * ...
        exp((1i * pi * R(k)^2 / lam)/Z) * q;

end
ComplexField = RzOSA;
Radius = R;
save('waveFieldOSA','ComplexField','Radius')

%calculate the beam at any arbitraty point after the OSA, here we have
%chosen the focal spot

load('waveFieldOSA','ComplexField','Radius')

rho = Radius; %points to numerically integrat with the trapizoid rule
R_lenght = 1.5e-5; %radial distance from center to calculate wave field
R_stepSize = 5e-11; %steps the distance is discretized into
R = (0:R_stepSize:R_lenght); %points were the wavefield will be calculated
Uo = ComplexField; % wave field at starting position
finalPosition = Lf; %location of the calcuated wave field
Z = (Lf-Losa);
RzLf = zeros(1,numel(R));

parfor j = 1:numel(R)
    q = trapz(rho ,exp((1i .* pi .* (1./lam) .* rho.^2)./Z).* ...
        besselj(0, ((2 .* pi .* R(j) .* rho)./(lam.*Z))).* Uo .* rho);
    RzFinal(1,j) = 2 .* pi .* exp(2.*pi .* 1i .* Z ./ lam)./(1i.*lam.*Z) * ...
        exp((1i * pi .* R(j).^2 ./ lam)./Z) .* q;
end

ComplexField = RzFinal;
Radius = R;
save('waveFieldFocus','ComplexField','Radius')

plot(R,(abs(RzFinal)))

%Convert the radial intensity into 2D Cartesian coordinates

N = 501; %half the number of points for 2D object

%x = linspace(0,5e-7,N); % Nice picture of the real space focused beam
x = linspace(0,1e-5,N); % Nice picture of the reciprocal space foused beam
y = x;

[X,Y] = meshgrid(x,y); %create X,Y mesh in Cartesian coordinates

```

```
[theta, r] = cart2pol(X,Y); %population mesh of radii

pp = pchip(Radius,ComplexField); %create interpolation function
I = ppval(pp,r); %populate 2D mesh with interpolated intensities

X = X(1,:);
flipX = -flip1r(X);
X = horzcat(flipX,X(2:end));
Y = X;
A = flipud(I);
B=vertcat(A,I(2:end,:));
C = flip1r(B);
D=horzcat(C,B(:,2:end));
ComplexField = D;

save('2DFocusedBeam','ComplexField','X','Y');

surf(abs(fftshift(fft2(ComplexField))), 'edgecolor','none')

ET = toc;
```

[Published with MATLAB® R2016a](#)

```
function [ phi ] = Uzp_phase( rho, lam, Lf, PHIZp, PHICs, Rzp, Rcs)
%Returns the phase, phi, imparted by the zone plate and center stop at a
%given radius
% The ouput phase with either be 0,1,PHIZp, or PHIZp*PHICs

m = floor( (rho.^2 ./ (lam.*Lf)) + 0.5);
mzp = mod(m,2); % n = 0 for even and 1 for odd
mcs = gt(Rcs,rho);
mtot = gt(rho,Rzp);

phi = (((exp(1i .* PHIZp)-1) .* mzp )+ 1) .* ...
      (((exp(1i .* PHICs)-1) .* mcs) +1) ) .* (1 - mtot) ;

end
```

[Published with MATLAB® R2016a](#)

A.2 Create Lattice Sum and Rocking Curve using Focused Beam

```
clear all
tic
%This script calls on a variable created by the 'CreateFocusedBeam' script

%Define constants
```

```

%Physical constants
c_light = 299792458; %speed of light in m/s
h_plank = 4.135667516e-15; %planks constant in ev*s

%wavelength or Energy
E = 10e3; %eV
lam = h_plank*c_light/E; %m

%Load focused beam profile
load('2DFocusedBeam','x','y','ComplexField')

%Detector parameters
Lccd = 1.013; % distance between sample and detector in m
pixSize = 13e-6; %size of detector pixels in m

%Materials Parameters
theta_Si = 27.4069; %experimentally measured Bragg angle in deg
theta_SiGe = 26.9469;%experimentally measured Bragg angle in deg
lat_Si = (2 * lam) / sind(theta_Si); %calcuated out of plane
%lattice constant in m
lat_SiGe = (2 * lam) / sind(theta_SiGe); %calcuated out of plane
%lattice constant in m

t_Si = 10e-9;%experimentally measured layer thickness
t_SiGe = 91e-9;%experimentally measured layer thicknes
Numlayers_Si = round(t_Si/lat_Si); %layer Thickness in m
Numlayers_SiGe = round(t_SiGe/lat_SiGe); %layer Thickness in m

F_Si = 7.15; %atomic form factor for each layer
F_SiGe = (.7*7.15+.3*17.1);

%Simulation Parameters

thetaCenter = 27.3069;
delTheta = 1.16; %width of the rocking cruve in deg
numSteps = 291; %number of steps in the rocking cruve

%Simulate Rocking Curves
angleArray = ...
    linspace(thetaCenter-delTheta/2,thetaCenter+delTheta/2,numSteps);
FieldSize = size(ComplexField);
threeDField = zeros(1001,1001,numSteps);
xdpMatrix = zeros(numSteps, FieldSize(2));
ydpMatrix = zeros(numSteps, FieldSize(1));

for j = 1:numSteps
[ threeDField(:,:,j), xdpMatrix(j,:), ydpMatrix(j,:)] =...
    LatticeSumWithFocusedBeam(thetaCenter,angleArray(j),ComplexField,...
    x,lam,Lccd, lat_Si,lat_SiGe, Numlayers_Si,Numlayers_SiGe,F_Si, F_SiGe);
end

intensityMatrix = abs(threeDField).^2;

```

```
MI = max(max(max(intensityMatrix)));

ET = toc;
```

Published with MATLAB® R2016a

```
function [ finalField, xdp, ydp] = LatticesumwithFocusedBeam...
( thetaCenter, thetaInc, ComplexField, X, lam,Lccd, lat_Si,...
lat_SiGe,Numlayers_Si,Numlayers_SiGe,F_Si, F_SiGe)
%Create a diffraction pattern at a specified angle
% The inputs are related to the beam geometry and the sample, and the
% output is the diffracted complex wave field at the detector along with
% the detector real space coordinates in meters. The atomic scattering
% factor is for the 004 and is assumed to be constant. Both samples are
% assumed to be cubic.

angle = degtorad(thetaInc);

N = size(ComplexField);

threeDField(:, :,1) = fftshift(fft2(ComplexField));
b = 1./((X(end)-X(end-1)));

%define reciprocal space lattice positions
l_Si = 2*lat_Si*sin(angle)/lam;
l_SiGe = 2*lat_SiGe*sin(angle)/lam;
h_lat = 0;
k_lat=0;

%define structure factor as this angle.
SF_Si = F_Si.*(1+exp(1i*pi*(h_lat+k_lat))+exp(1i*pi*(h_lat+l_Si))+...
exp(1i*pi*(k_lat+l_Si))).*(1+exp(1i*pi/2*(h_lat+k_lat+l_Si)));
SF_SiGe = F_SiGe.*(1+exp(1i*pi*(h_lat+k_lat))+exp(1i*pi*(h_lat+l_SiGe))+...
exp(1i*pi*(k_lat+l_SiGe))).*(1+exp(1i*pi/2*(h_lat+k_lat+l_SiGe)));

% Definition of kx, ky, and kz

threeDField(:, :,2) = repmat(-b/2:b/(N(1)-1):b/2,N(1),1);
threeDField(:, :,3) = transpose(threeDField(:, :,2));
threeDField(:, :,4) = real((sqrt(repmat(lam^(-2),N(1),N(1)) -...
threeDField(:, :,2).^2 - threeDField(:, :,3).^2))+0);

% Application of Ying Transformation Matrix

HolderthreeDField(:, :,1) = sin(angle)*threeDField(:, :,2)+cos(angle)...
*threeDField(:, :,4);
HolderthreeDField(:, :,2) = -cos(angle)*threeDField(:, :,2)+sin(angle)...
*threeDField(:, :,4);
threeDField(:, :,2) = HolderthreeDField(:, :,1);
threeDField(:, :,4) = HolderthreeDField(:, :,2);
```

```

%apply the lattice sum to the different q values
q = 2 * pi * 2 .* threeDField(:, :, 4);
%these are the equations for the lattice sums
SA = sin(0.5*Numlayers_SiGe*q*lat_SiGe) ./sin(0.5*q*lat_SiGe);
SB = sin(0.5*Numlayers_Si*q*lat_Si) ./sin(0.5*q*lat_Si);
SAA = SA .* exp(1i*(Numlayers_SiGe-1)*q*lat_SiGe*0.5);
SBB = SB .* exp(1i*(Numlayers_Si+1)*q*lat_Si*0.5);

sumArgs(:, :) = (SF_SiGe .* SAA) + (SF_Si .* SBB);

% multiply by the Complex Field to create diffracted beam

threeDField(:, :, 5) = threeDField(:, :, 1) .* sumArgs(:, :);

%Rotate coordinate frame to the detector
angle = degtorad(thetaInc - 2*thetaCenter);

HolderthreeDField(:, :, 1) = sin(angle)*threeDField(:, :, 2)+...
    cos(angle)*threeDField(:, :, 4);
HolderthreeDField(:, :, 2) = -cos(angle)*threeDField(:, :, 2)+...
    sin(angle)*threeDField(:, :, 4);
threeDField(:, :, 2) = HolderthreeDField(:, :, 1);
threeDField(:, :, 4) = HolderthreeDField(:, :, 2);

%Propagate to the detector
xdp = threeDField(1, :, 2).*lam.*Lccd ;
ydp = (threeDField(:, 1, 3)).*lam.*Lccd);

finalField = threeDField(:, :, 5);
end

```

Published with MATLAB® R2016a